UNIVERSITÁ DEGLI STUDI DI ROMA "TOR VERGATA"

FACOLTÁ DI INGEGNERIA

DOTTORATO DI RICERCA IN INGEGNERIA DELLE TELECOMUNICAZIONI E MICROELETTRONICA

XXII CICLO

Multiscale Thermal Models for Nanostructured Devices

Giuseppe Romano

A.A. 2009/2010

Tutor: Prof. Aldo Di Carlo

Coordinatore: Prof. Giuseppe Bianchi

To my Friend, Angelo Frammartino

Acknowledgement

This work would not have been possible without the direct or indirect help of many people. First of all, I would like to thank my supervisor, Prof. Aldo Di Carlo for accepting me as a PhD student. He always supported and encouraged me. Special thanks also to Prof. Alessandro Pecchia for his invaluable scientific support.

A special acknowledgement also to Matthias Auf Der Maur and Alessio Gagliardi for several interesting discussions and for thoroughly reading my thesis.

I thank the desk mate Gabriele Penazzi for the stimulating conversations we had during the work time and beyond.

I'm very grateful to my colleagues at OLAB. They accepted me with friendliness and provided a pleasant company during the last three years.

I'm also grateful to my friends Andrea, Cristina, Daniele, Domenico, Ernesto, Giuliana, Marco, Mauro, Pierluigi and Stefano for sharing amazing moments along the recent years.

Finally I would like to thank my family and relatives for supporting me in everything. A big hug to my little twin sisters Martina and Valentina, my sister Marina and my brother Andrea.

Rome, 2010

Giuseppe Romano

Contents

Abstract

Modern electronic devices comes from a double evolution. On one hand the miniaturization techniques have reduced the traditional devices to the microscopical scales. Such approach is called *top-down*. On the other hand, the researching in multidisciplinary fields has created novel devices, natively nanostructured. Carbon nanotubes, nanowire and quantum dots are examples of such devices, designed following an approach called *bottom-up*.

These two evolutive lines are converging in strongly heterogeneous devices, whose features are due to both micro and macroscopical elements. Hence, there is the need of CADs to employ models acting at different scales in the same simulation. Such a model is called *multiscale model*. Multiscale models involve several fields, ranging from fluid dynamics to electronic transport.

In this work we deal with heating and heat dissipation in a multiscale domain. In particular, we investigate the Joule's effect at the macro, meso and nanoscales.

We start to compute the self-heating effect by modeling the electron-phonon interaction at the Born Approximation level. The heating of a molecule under bias is computed by means of an effective temperature. The transport of heat and charge is calculated within the Non Equilibrium Green's Function (NEGF) approach whereas the ground state is obtained within the Density Functional Tight Binding (DFTB) method. We apply the method on different molecular systems.

The Boltzmann Tranport Equation (BTE) for phonons is used as mesoscale model of heat dissipation. At the macroscale, the temperature map is obtained at the diffusive level with the Fourier model. Both the BTE based model and the Fourier model have been implemented within the Finite Element Method (FEM). We perform a Fourier/BTE multiscale simulation of a GaN quantum dot embedded in a AlGaN nanocolumn.

All the three models have been implemented in TiberCAD, the multiscale simulator of optoelectronic devices developed by the OLAB research group at the University of Rome "Tor Vergata".

Riassunto

I moderni dispositivi elettronici sono frutto di una doppia evoluzione. Da un lato le tecniche di miniaturizzazione hanno spinto le dimensioni dei dispositivi tradizionali fino alle scale nanometriche. Questo approccio è il cosiddetto *top-down*. Dall'altro lato, la ricerca multisciplinare ha dato vita a nuove categorie di dispositivi, nativamente nanostrutturati. I nanotubi di carbonio, nanowire e quantum dot sono esempio di questo approccio, denominato *bottom-up*.

Questi due percorsi stanno convergendo in dispositivi che sono fortemente eterogenei, le cui feature sono dovute ad effetti sia dei suoi elementi micro che macro. C'è quindi la necessità di CADs capaci di impiegare modelli relativi a diverse scale nella stessa simulazione. Tali modelli sono denominati *modelli multiscala*. I modelli multiscala coinvolgono differenti aree di studio, dalla fluidodinamica al trasporto elettronico.

In questo lavoro trattiamo il riscaldamento e dissipazione di calore alle scale macro, meso e nano.

L'effetto Joule alle nanoscale è calcolato considerando l'interazione elettrone−fonone nell'approssimazione di Born. Il riscaldamento di una molecola, sotto l'azione di un bias, è calcolato mediante l'introduzione di una temperatura efficace. Il trasporto di carica e del calore sono ottenuti mediante le funzioni di Green di non-equilibrio (NEGF) mentre lo stato fondamentale è calcolato con il metodo Density Functional Tight Binding (DFTB). Come esempio, considereremo diversi sistemi molecolari.

Per quanto riguarda la dissipazione del calore a livello mesoscopico, impieghiamo un modello basato sull'equazione del trasporto di Boltzmann (BTE). A livello macroscopico, la mappa di temperatura è ottenuta mediante il modello di Fourier. Sia il modello basato su BTE che il modello Fourier sono stati implementati secondo il metodo agli elementi finiti (FEM). Infine, è stata eseguita una simulazione multiscala Fourier/BTE di un quantum dot di GaN inserito in una nanocolonna di AlGaN.

Tutti e tre i modelli sono stati implementati in TiberCAD, il simulatore multiscala di dispositivi optoelettronici sviluppato dal gruppo di ricerca OLAB all'universitá di Roma "Tor Vergata".

Chapter 1

Introduction

Electro-thermal simulations deal with charge and heat carriers transport. In particular, it's possible to decompose the system in the electrons, holes and phonons subsystems. They have different dynamics and, given a characteristic lengthscale and timescale, the transport regime could be different for each of them. Interaction between charge carriers and phonons cause the Joule's effect. During their dissipative transport, electrons and holes lose energy which is stored and dissipated by phonons.

This work is mainly involved in heating and heat dissipation at different regimes. Furthermore, effort is devoted to couple heat transport models operating at different scales. We apply the developed models to realistic devices.

1.1 Heat transport regimes

In the 1848 Fourier discovered the phenomenological law, bearing his name, of the heat transport. He found that the thermal flux flowing through a wall subjected to a difference of temperature is given by

$$\mathbf{J} = -\kappa \nabla T \tag{1.1}$$

where κ is the thermal conductivity.

The key assumption of the Fourier model is based on the local thermodynamic equilibrium. As a consequence, phonons out coming from a scattering are assumed to have the equilibrium distribution according to the local temperature. This regime, called *macroscale* regime, holds roughly for characteristic length greater than $10\,\gamma$.

The local equilibrium assumption merely fails whenever the device length becomes comparable to the phonon mean free path. To give an estimation of the phonons mean free path we may start from the expression of the lattice thermal conductivity

$$\kappa = \frac{1}{3} v_g^2 \tau C \tag{1.2}$$

For Silicon it is about $\kappa = 142.3\,W/mK$. The sound velocity is $v_g = 6400 m/s$ whereas the heat capacity is $C = 1.6610^6 J/m^3 K$ at $300\,K$. Inverting Eq. 1.2 the relaxation time is $\tau = \frac{3\kappa}{C v_g^2} = 6.28\,ps$. The phonon mean free path is, therefore, $\Lambda = v_g\,\tau \approx 40\,nm$.

In order to capture the size effects in modern devices a novel approach is necessary. The step forward was the employment of the Boltzmann Transport Equation (BTE) for phonons. Several versions, mainly based on the relaxation time approximation, have been implemented. This regime is what is generally recognized as the *mesoscale* regime.

Although BTE based models are able to capture thermal effects that the Fourier model does not, there still exist devices which need of a more sophisticated approach. This is the case of molecular electronics or carbon nanotubes bases devices. Their short dimensions make the quantum wave effects predominant and a quantum mechanical approach becomes necessary. Quantum effects such as interference and tunneling may appear whenever the characteristic length of the device is comparable with dominant phonon wavelength which can can be estimated by the expression

$$\lambda = \frac{\Theta_D\, a}{T} = \frac{v_g \hbar}{2.82\, k_B\, T} \tag{1.3}$$

where Ω_D is the Debye frequency and a is the interatomic spacing. At $4\,K$ the dominant phonon wavelength of Silicon is about $27\,nm$ and, therefore, becomes comparable with the device length. At the short scale, as for the electron case, the thermal conductance is quantized and assumes the expression

$$G_0 = \frac{\pi^2 k_B^2 T}{3\,h} \tag{1.4}$$

This regime is the *nanoscale* regime. A review on heat transport regime can be found in Raf. [1]. As in this work we deal with steady state system we do not pay attention to the timescale related regimes.

1.2 The need of a multiscale simulation

Devices of interest lie between the macro and mesoscale. More precisely, we may have physics effects related to different scales in the same device. Let us give some examples.

In 2006 Muller et al proposed a quantum dot based LASER (see Fig. 1.1). Although the device belongs to the macroscale regime, what determines the main features are the quantum dots which lie in the mesoscale regime. The crucial point here is: on one hand one wants to get all the important details, on the other hand it's necessary to keep reasonable low the computational cost. A possible way to match theses different needs at the same time could be a *multiscale* approach. The aim of a multiscale scheme is coupling different regimes in the same simulation. In the LASER shown in Fig. 1.1 a possibility could be to compute the quantum charge in the dot and give it back to the Poisson equation which provides the electrostatic potential along all over the device.

Another example is represented by the carbon nanotube (CNT) based transistor shown in Fig. 1.2. In order to get a proper treatment of the electrical current and the heat dissipation in the CNT a quantum mechanical approach is necessary. However, the rest of the device still obeys to the macroscopic laws. A multiscale approach might be to calculate the quantum transport only along the CNT and then match it with the diffusive flux computed at the

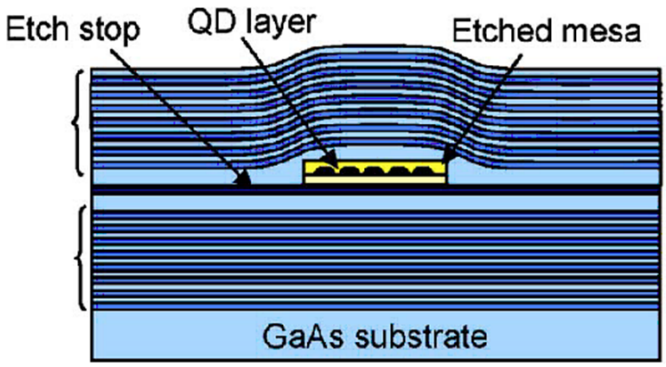

Figure 1.1: Quantum dot based MESA

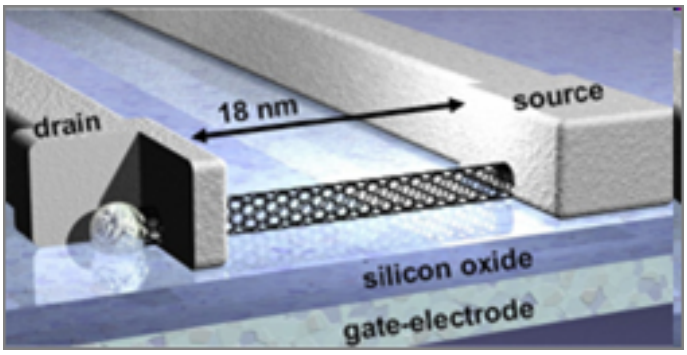

Figure 1.2: Carbon nanotubes based transistor

contacts. The domain partitioning as well as the matching criterium label the multiscale approach.

Clearly, as almost every physic subjects, the understanding of the heat transport phenomena has followed a top down approach, i.e. it started from the most macroscopical law to arrive to the transport at the nanoscale. The nature behaves exactly as the opposite way, i.e. it uses *small* pieces to build the macroscopical object, visible to human eye. The next three chapter will describe the heat transport model following the nature approach. This description involves the Chapter 2,3 and 4. The fifth chapter will be devoted to the description of TIBERCAD, the platform used to code the models described in this work. In the sixth chapter we will apply the developed models to realistic devices. Conclusion and final remark conclude the work.

Chapter 2

Thermal balance at the nanoscale

2.1 Introduction

As the dimension of the system approaches the wavelength of phonons a proper treatment of heat transport needs to be based on a quantum mechanical approach. The system considered in this work comprises a molecule interposed between two contacts (see Fig. 2.1). We as-

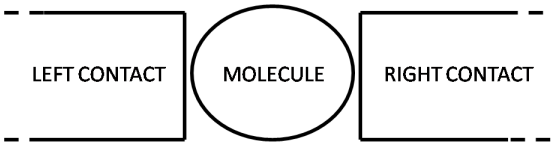

Figure 2.1: *Atomistic system*

sume the contact to be at thermodynamic equilibrium while the voltage drops only along the molecule. The energy is stored in the molecule by means of vibrons, i.e. localized phonons whose equilibrium population is given by the Bose-Einstein distribution

$$n(T_0) = \frac{1}{e^{\frac{\hbar\omega}{k_B T_0}} - 1} \tag{2.1}$$

where $\hbar\omega$ is the vibron energy and k_B is the Boltzmann constant. When a bias is applied to the system the electrons and phonons interact with each other exchanging energy. As emission of a vibron is more probable than absorption, the net effect is the heating of the molecule. The phonon distribution departs from the Bose-Einstein distribution. Non equilibrium vibrons can interact with themselves via anharmonic interaction or may decay in phonons of the contacts. In this work, we neglect the first effect whereas the vibron-phonon interactions, which represent the dissipation via conduction, is computed by first principles. In the next

paragraphs we will describe the balance equation and will provide the derivation of terms related to the heating and the heat dissipation.

2.2 The energy balance

The vibron dynamics is described by a rate equation that balances the quanta emitted and absorbed via electron-vibron interactions,

$$R_q^e = (N_q + 1)E_q - N_q A_q, \tag{2.2}$$

and the vibrons dissipated via vibron-to-phonon decays [2] into the contact reservoirs,

$$R_q^d = \sum_\alpha J_q^\alpha (N_q - n_q(T_\alpha)). \tag{2.3}$$

In Eqs. (2.2)-(2.3), α runs over the contact index (L and R contacts in this case), q is the mode label, N_q is the non-equilibrium phonon population, $n_q(T_\alpha)$ is the equilibrium phonon population at temperature T_α, J_q^α are the decay rates of molecular vibrons into the phonon reservoir of contact α. The terms A_q and E_q represents the absorption and emission rates, respectively. The steady state solution is obtained by imposing $R_q^e = R_q^d = R_q$, resulting in the non-equilibrium vibron population,

$$\begin{aligned} N_q &= \frac{Rq}{Jq} + \frac{\sum_\alpha J_q^\alpha n_q(T_\alpha)}{Jq} \\ &= \frac{\sum_\alpha J_q^\alpha n_q(T_\alpha) + E_q}{J_q + A_q - E_q}, \end{aligned} \tag{2.4}$$

whereas the net emission rate of quanta is given by

$$R_q = \sum_\alpha J_q^\alpha \frac{E_q \left[n_q(T_\alpha) + 1\right] - A_q n_q(T_\alpha)}{J_q + A_q - E_q}. \tag{2.5}$$

In Eqs. (2.4)-(2.5) the terms J_q represent the total phonon decay rates, i.e. $J_q = \sum_\alpha J_q^\alpha$. From the previous expression it should be noted that when there is no dissipation ($J_q = 0$), the condition $R_q = 0$ must be fulfilled. this implies that the heat must be absorbed by the electrons themselves. The phonon-phonon decays give rise to a heat flux going out from the α-contact that can be written as

$$P_q^\alpha = \hbar\omega_q J_q^\alpha \left[N_q - n_q(T_\alpha)\right], \tag{2.6}$$

which, by using Eq. (2.4), becomes

$$P_q^\alpha = \frac{J_q^\alpha \hbar\omega_q \sum_\beta J_q^\beta \left[n_q\left(T_\beta\right) - n_q\left(T_\alpha\right)\right]}{J_q} + \frac{\hbar\omega_q R_q J_q^\alpha}{J_q} \tag{2.7}$$

The first term in Eq. (2.7) represents the heat flux driven by the gradients of temperature between contacts; the second contribution is the power dissipated by the Joule's effect.

This expression (2.4) is particularly instructive, since it allows to carry several limit results. For instance in the limit of very fast phonon relaxation to the reservoirs ($J_q = \infty$), we find $N_q = n_q(T_0)$. This is an expected result, since it simply means that the coupling is so strong that thermal equilibrium is immediately restored, no matter how fast phonons are emitted in the system. In the opposite limit of no relaxation ($J_q = 0$), phonon absorption by the electrons must balance their emission, leading to

$$N_q = \frac{E_q}{A_q - E_q}. \tag{2.8}$$

Remarkably, this expression is independent on the electron-phonon coupling γ_q, since E_q and A_q are both proportional to γ_q^2. This can be understood since changes in γ_q modify both the absorption and emission probabilities, leaving the steady state number of phonon, N_q, unchanged.

We also note that a stationary solution is not always guaranteed and generally does not exist whenever $N_q < 0$. From Eq. (2.4) we get the system stability condition for $J_q + A_q > E_q$. The simple interpretation of this is that $J_q + A_q$ expresses the rate of phonon damping while E_q the rate of phonon creation (It is not actually easy to get an simple interpretation of E_q, since the emission is proportional to $N_q + 1$). Stability is possible only when the damping rate overcomes the emission rate. Whenever these to quantities become close, the steady state number of phonons turns out very large.

Since at steady state the amount of power emitted in the molecule must balance the power dissipated to the reservoirs, a simple (though sometimes not so intuitive) concept can be outlined. For slow dissipations the power emitted is essentially limited by the dissipation rate, J_q. The power emitted must be small and tend to zero as $J_q \to 0$. In the opposite limit of fast dissipation, the power emitted reaches a maximum, only limited by the electron-phonon coupling and by the inelastic tunneling probability, both contained in E_q and A_q.

The molecular heating is described in terms of an *effective* temperature T_m which is found by the equivalence between the total vibrational energy, U, given by the non-equilibrium population N_q with the energy obtained imposing an equilibrium Bose-Einstein population at temperature T_m,

$$U = \sum_q \hbar\omega_q N_q = \sum_q \frac{\hbar\omega_q}{exp(\frac{\hbar\omega_q}{k_B T_m}) - 1}. \tag{2.9}$$

The molecular temperature should not be interpreted as a thermodynamic quantity but can be regarded as a parameter mapping the vibrational energy of the molecule. This is established by the monotonic dependence between U and T_m expressed by Eq. (2.9). The advantage of using T_m is that it does not depend on the size of the system and coincides with the rigorous concept of temperature in the thermodynamical limit.

2.3 Heating

We briefly report the essential result of the theory of quantum transport with incoherent electron-vibron scattering presented in Ref. [3,4]. The electron-phonon coupling Hamiltonian is written in the form

$$H_{el-ph} = \sum_{q,\mu,\nu} \gamma^q_{\mu\nu} c^+_\mu c_\nu \left[a^+_q + a_q \right], \tag{2.10}$$

by making use of the standard relationships between the position operator and the creation/annihilation phonon operators, a^+_q and a_q, and where c^+_μ and c_ν are, respectively, the creation and annihilation operators of one electron in the atomic basis. The coupling matrices,

$$\gamma^\alpha_{\mu\nu} = \sqrt{\frac{\hbar}{2\omega_q M_q}} \sum_\alpha \left[\frac{\partial H_{\mu\nu}}{\partial R_\alpha} - \sum_{\sigma,\lambda} \frac{\partial S_{\mu\sigma}}{\partial R_\alpha} S^{-1}_{\sigma\lambda} H_{\lambda\nu} - \sum_{\sigma,\lambda} H_{\mu\lambda} S^{-1}_{\lambda\sigma} \frac{\partial S_{\sigma\nu}}{\partial R_\alpha} \right] e^q_\alpha, \tag{2.11}$$

contain the atomic masses M_q, the mode frequencies ω_q, and the normal modes of vibration e^q_α. The non-orthogonality of the atomic basis set is reflected by the presence of a non-diagonal overlap matrix $S_{\mu\nu}$ and its derivative with respect to the ionic positions R_α.
The electron-phonon interaction is treated within perturbation theory of the non-equilibrium Green's function formalism and the current through the junction is computed using the Meir-Wingreen formula [5],

$$I = \frac{2e}{h} \int_{-\infty}^{+\infty} Tr \left[\Sigma^<_L(\omega) G^>(\omega) - \Sigma^>_L(\omega) G^<(\omega) \right] d\omega, \tag{2.12}$$

where $\Sigma^{<(>)}_L$ represents the injection rate of electrons (holes) from the *left* contact of the device, while $G^{<(>)}$ is the electron (hole) correlation function, obtained from the kinetic equations [6, 7]

$$G^{<(>)}(\omega) \quad = \quad G^r(\omega) \Sigma^{<(>)}(\omega) G^a(\omega), \tag{2.13}$$

and $G^{r(a)}$ are the retarded (advanced) Green's functions given by the usual expression

$$G^{r(a)}(\omega) = \left[\omega S - H - \Sigma^{r(a)} \right]^{-1}. \tag{2.14}$$

Where the single electron Hamiltonian H is obtained within the Density-Functional Tight-Binding (DFTB) method [8]. The *lesser* and *greater* self-energies (SE) are given by the sum of three terms,

$$\Sigma^{<(>)}(\omega) = \Sigma^{<(>)}_L(\omega) + \Sigma^{<(>)}_R(\omega) + \Sigma^{<(>)}_{ph}(\omega). \tag{2.15}$$

The current expressed by Eq. (2.12) contains both a coherent and an incoherent component. The coherent component arises from $\Sigma^{<(>)}_L(\omega)$ and $\Sigma^{<(>)}_R(\omega)$, whereas the incoherent component is associated to $\Sigma^{<(>)}_{ph}(\omega)$, describing scattering processes caused by electron-phonon interactions. The electron-phonon self-energy can be evaluated with diagrammatic techniques. The self-consistent Born approximation (SCBA) is expressed by

$$\Sigma^{<(>)}_{ph}(\omega) = i \sum_q \int_{-\infty}^{+\infty} \frac{d\omega'}{2\pi} \gamma_q G^{<(>)}(\omega - \omega') \gamma_q D^{<(>)}_q(\omega'), \tag{2.16}$$

where $D_q^{<(>)}$ are the correlation functions related to the vibrational modes,

$$D_{0,q}^{<}(\omega) = -2\pi i \left[(N_q+1)\delta(\omega+\omega_q) + N_q\delta(\omega-\omega_q)\right]$$
$$D_{0,q}^{>}(\omega) = -2\pi i \left[(N_q+1)\delta(\omega-\omega_q) + N_q\delta(\omega+\omega_q)\right], \tag{2.17}$$

assumed as Einstein oscillators, i.e. the vibron lifetimes are neglected in the phonon propagator. Inserting (2.17) into (2.16) it is possible to derive an explicit formula for the electron-phonon self-energy,

$$\Sigma_{ph}^{<} = \sum_q N_q\gamma_q G^{<}(E-\omega_q)\gamma_q + (N_q+1)\gamma_q G^{<}(E+\omega_q)\gamma_q$$
$$\Sigma_{ph}^{>} = \sum_q N_q\gamma_q G^{>}(E+\omega_q)\gamma_q + (N_q+1)\gamma_q G^{>}(E-\omega_q)\gamma_q. \tag{2.18}$$

The self-consistency in Eq. (2.16) is implied by the use of a renormalized Green's function, $G^{<}$, whereas the first order Born approximation is obtained when the unrenormalized (zeroth order) Green's function is used to evaluate the electron-phonon self-energy. Using the relationship $Im\Sigma_{ph}^{r} = 1/2(\Sigma_{ph}^{>} - \Sigma_{ph}^{<})$ it is possible to compute Σ_{ph}^{r} that modifies the electron propagator in (2.14). As we are mainly interested in the electron lifetime and we restrict to weak electron-phonon coupling, the real part of Σ_{ph}^{r} that is responsible for a polaronic shift is neglected. Consistently, we also neglect the first order Hartree diagram, which gives a contribution to the real part only.

Let us see how get the expressions for A_q and E_q appearing in (2.2). In order to calculate R_q, first we introduce the net power emitted into the junction, which is given by the net rate of energy transferred to the molecule and that can be calculated using [9]

$$W = \frac{2}{h}\int_{-\infty}^{+\infty} \omega \left[\Sigma_{ph}^{<}(\omega)G^{>}(\omega) - \Sigma_{ph}^{>}(\omega)G^{<}(\omega)\right] d\omega. \tag{2.19}$$

We notice that the electron-phonon self-energy (2.18) is expressed as a linear superposition of individual mode contributions. Inserting Eq. (2.18) into (2.19) and exploiting this linearity, it is possible to write the net power emitted in each vibrational mode,

$$W_q = \frac{2}{h}\int_{-\infty}^{+\infty} i_q(\omega)\omega d\omega, \tag{2.20}$$

where $i_q(\omega)$, given by

$$i_q(\omega) = Tr\left[\Sigma_q^{<}(\omega)G^{>}(\omega) - \Sigma_q^{>}(\omega)G^{<}(\omega)\right], \tag{2.21}$$

is interpreted as the current at a virtual contact, having the role of breaking the wavefunction phase and change the electronic energy (see Fig. 2.2) [10].

Current conservation requires that the net current at the virtual contact must vanish, i.e.,

$$I_q = \int_{-\infty}^{+\infty} i_q(\omega)d\omega = 0. \tag{2.22}$$

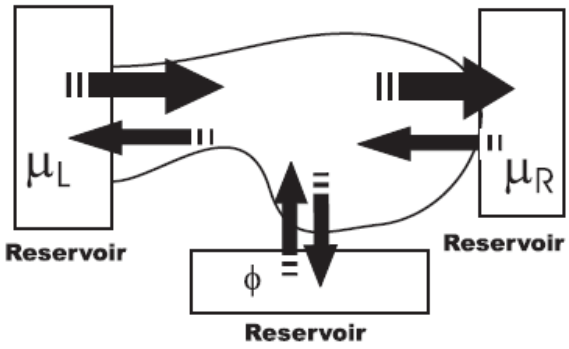

Figure 2.2: SDiagram showing the in- and out-scattering electron in and out from the electrodes and the virtual phase-breaking contact.

The net rate of phonon emission into the junction required by Eq. (2.4) can be defined as the ratio between the power dissipated in each mode and the mode energy, $R_q = W_q/\hbar\omega_q$.

The computation of Eq. (2.20) requires some care in order to avoid numerical inaccuracies. The delicate issue involved in such integration is the necessary condition of current conservation that relays on a cancellation of terms in Eq. (2.21). In order to fulfill current conservation a rather fine grid becomes necessary, although computationally very expensive. A much better strategy is to split Eq. (2.21) into the current out-coming (o) and in-coming (i) the virtual contact, respectively given by the first and the second term of Eq. (2.21). Collecting all terms proportional to N_q and $N_q + 1$, each of these contributions can be further divided into absorption (A) and emission (E) components, respectively. Using this procedure, the net current at the virtual contact can be written as

$$I_q = \int_{-\infty}^{+\infty} Tr\left[i^E_{q,o}(\omega) + i^A_{q,o}(\omega) - i^E_{q,i}(\omega) - i^A_{q,i}(\omega)\right] d\omega, \tag{2.23}$$

where the emission and absorption terms are

$$\begin{aligned} i^E_{q,o}(\omega) &= (N_q+1)Tr\left[\gamma_q G^<(\omega+\omega_q)\gamma_q G^>(\omega)\right], \\ i^E_{q,i}(\omega) &= (N_q+1)Tr\left[\gamma_q G^>(\omega-\omega_q)\gamma_q G^<(\omega)\right], \end{aligned} \tag{2.24}$$

$$\begin{aligned} i^A_{q,o}(\omega) &= N_q Tr\left[\gamma_q G^<(\omega-\omega_q)\gamma_q G^>(\omega)\right], \\ i^A_{q,i}(\omega) &= N_q Tr\left[\gamma_q G^>(\omega+\omega_q)\gamma_q G^<(\omega)\right]. \end{aligned} \tag{2.25}$$

Using the invariance of the Trace under cyclic permutation and changing integration variable it is easy to prove the identities

$$i^E_{q,o}(\omega) = i^E_{q,i}(\omega+\omega_q), \tag{2.26}$$

$$i^A_{q,o}(\omega) = i^A_{q,i}(\omega-\omega_q). \tag{2.27}$$

These expressions, inserted back into (2.20), can be used to show that

$$W_q = \frac{2}{h}\hbar\omega_q \int \left[i^E_{q,o}(\omega) - i^A_{q,o}(\omega) \right] d\omega. \tag{2.28}$$

This final result allows a much easier computation of the emitted power because it does not rely on the subtle cancellation of terms hidden in Eq. (2.23). Current conservation is guaranteed by construction, as it can be easily shown by inserting the identities (2.26) and (2.27) into (2.23). The result is a numerically reliable expression using a coarser integration grid.

The technical details of our implementation are given in the Appendix. Finally we observe that reduction of this heavy computational step allows to perform calculations which needs to include the full energetic dependency of the Green's functions, avoiding the simplifying assumptions made in Ref. [11].

If we compare Eq. (2.31) with Eq. (2.2) we get the expressions for A_q and E_q

$$A_q = \frac{2}{h} \int Tr \left[\gamma_q G^<(E - \hbar\omega_q) \gamma_q G^>(E) \right] dE, \tag{2.29}$$

$$E_q = \frac{2}{h} \int Tr[\gamma_q G^<(E + \hbar\omega_q) \gamma_q G^>(E)] dE. \tag{2.30}$$

Let us validate these expressions at the equilibrium condition. Hereafter, we assume that the phonon decay rates are equal for the two contacts, i.e. $J^\alpha_q = J_q/2$. Furthermore, the two contacts are maintained at the same temperature T_0. Under this assumption the net rate of phonon emission and their non-equilibrium population can be written as

$$R_q = \frac{J_q}{J_q + A_q - E_q} \left[(n_q + 1) E_q - n_q A_q \right] \tag{2.31}$$

$$N_q = n_q(T_0) + \frac{R_q}{J_q} \tag{2.32}$$

At $V = 0$ the system reaches thermodynamic equilibrium and $R_q = 0$ (and, consequently, $N_q = n_q(T_0)$) which leads to the equilibrium conditions, $A_q = E_q e^{\hbar\omega_q / k_b T_0}$.

It is straightforward to show that this condition is satisfied thanks to the general relationship $G^<(E) = -e^{E/k_b T_0} G^>(E)$ at $V = 0$, applied to the Eqs. (2.29) and (2.30). The contrary, the relationship $A_q = E_q e^{\hbar\omega_q / k_b T_0}$ is not valid under general bias conditions.

2.4 Heat dissipation

The atomic vibrations of the open structure are treated in the usual way [12–15] by decoupling the Hamiltonian as a superposition of normal modes of vibration. The modes and frequencies for the whole structure are obtained solving the eigenvalue system

$$\sum_j \mathcal{H}_{ij} e^p_j = \sum_j \mathcal{M}_{ij} e^p_j \omega^2_p, \tag{2.33}$$

where e_j^p are the normal modes, M_{ij} and H_{ij} are the mass and Hessian matrices, respectively. The Hessian matrix is defined using the Hellmann-Feynmann theorem as

$$\mathcal{H}_{\alpha,\beta} = \frac{\partial^2 E}{\partial R_\alpha \partial R_\beta}, \tag{2.34}$$

where E is the total energy of the system. The practical problem posed by Eq. (2.33) is that the contacts are semi-infinite and consequently the matrices $\mathcal{H}_{ij}$ and $\mathcal{M}_{ij}$ are of infinite dimension.

In order to treat the open boundary conditions on the bulk side of the contacts we use the Green's function formalism. The treatment is analogous to the electronic Green's functions, usully defined in quantum transport problems [9]. We start by defining the Green's function corresponding to Eq. (2.33) and by partitioning the system into molecule and contact blocks. For instance, restricting to the left contact only, the following equation can be written for the Green's function

$$\begin{bmatrix} \mathcal{M}_M\omega^2 - \mathcal{H}_M & \mathcal{H}_{M,L} \\ \mathcal{H}_{L,M} & \mathcal{M}_L\omega^2 - \mathcal{H}_L \end{bmatrix} \begin{bmatrix} G_M^r & G_{M,L}^r \\ G_{M,L}^r & G_L^r \end{bmatrix} = \begin{bmatrix} I & 0 \\ 0 & I \end{bmatrix}. \tag{2.35}$$

The matrix blocks are obtained from the computation of the Hessian of the whole system. The label M and L stand for the molecular and left contact blocks, respectively. In practice, a particular treatment has to be used for the contact as the calculation of the Hessian must be performed on a finite system. Our strategy is to compute the Hessian for a truncated system that includes a sufficiently large portion of the contacts. In each contact we can identify a surface and a bulk, comprising two principal layers (PL), which are chosen in order to satisfy the condition that the Hessian matrix appears block-tridiagonal, i.e. the elastic coupling does not extend beyond nearest neighbor PLs. Hydrogen saturation or a buffer layer can be included to terminate the cutted edge at the bulk sides of each contact. The diagonal blocks of the Hessian corresponding to the PLs and the coupling blocks between PLs are replicated an infinite number of times, corresponding to the definition of an ideal bulk. The converged is ensured by increasing the PL size. The Green's function is defined in the usual form,

$$G^r(\omega^2) = \frac{1}{\mathcal{M}_M\omega^2 - \mathcal{H}_M + \Pi_R^r(\omega^2) + \Pi_L^r(\omega^2)}, \tag{2.36}$$

where the self-energies $\Pi_{L,R}^r(\omega^2)$ exactly map the infinite left and right contacts into the finite portion of the molecular sub-system. Atomic units ($\hbar$=1) are used throughout. In the Green's function (2.36) we keep the explicit dependency on ω^2, as expressed in the corresponding eigensystem (2.33). This self-energies are obtained from Eq. (2.35) as

$$\Pi_L^r(\omega^2) = \mathcal{H}_{M,L} g_L^r(\omega^2) \mathcal{H}_{L,M}, \tag{2.37}$$

where g_L^r represents the surface Green's function of the left semi-infinite contact, defined as

$$g_L^r(\omega^2) = \frac{1}{\mathcal{M}_L\omega^2 - \mathcal{H}_L}. \tag{2.38}$$

This can be computed using recursive algorithms from the knowledge of the PL blocks defined above. The local phonon density of states (LDOS) projected on the molecule can be computed from $G^r(\omega^2)$ by means of the expression,

$$\rho(\omega^2) = -\frac{1}{\pi} Tr\left\{ Im\left[G^r(\omega^2)\right]\right\}. \tag{2.39}$$

Also this quantity is expressed in terms of ω^2. The connection with the usual DOS can be recovered using the functional derivative

$$\rho(\omega) = \frac{\partial N}{\partial \omega} = 2\omega\rho(\omega^2) = -\frac{2\omega}{\pi} Tr\left\{ Im\left[G^r(\omega^2)\right]\right\}. \tag{2.40}$$

The frequencies and modes of the molecule interacting with the contacts can be obtained by solving the eigensystem

$$\sum_j \left[\mathcal{H}_{M,ij} + \Pi_{ij}\left(\omega^2\right)\right]\phi_j^q = \sum_j \omega_q^2 M_{ij}\phi_j^q. \tag{2.41}$$

In principle this equation can give exact eigenvectors, ϕ^q, and frequencies, ω_q, but it is rather impractical to solve because of the nonlinear terms given by the complex self-energies. For this reason it is often useful to take a first order expansion of (2.41), which approximates the exact eigenvectors of the coupled system with those of the uncoupled molecule, e^q, satisfying the equation

$$\sum_j \mathcal{H}_{M,ij} e_j^q = \sum_j \mathcal{M}_{M,ij} e_j^q \omega_q^2, \tag{2.42}$$

whereas the mode frequencies are given by

$$\bar{\omega_q}^2 = \omega_q^2 + \mathcal{Z}_q \sum_{ij} e_i^q Re\left[\Pi_{ij}^r(\omega_q^2)\right] e_j^q, \tag{2.43}$$

where

$$\mathcal{Z}_q = \left[1 - \sum_{ij} e_i^q \left.\frac{\partial Re\left[\Pi_{ij}(\omega^2)\right]}{\partial \omega^2}\right|_{\omega=\omega_q} e_j^q\right]^{-1}. \tag{2.44}$$

In practice this approximation gives new, renormalized, frequencies and associated broadening, reflecting the interaction with an open system. The mode broadening is related to the imaginary part of the self-energy by

$$\Gamma_q = \sum_{ij} e_i^q Im\left[\Pi_{ij}^r(\omega_q^2)\right] e_j^q. \tag{2.45}$$

The connection between broadening and phonon decay rate can be obtained starting from the usual representation of the Green's function on the basis of the eigenmodes,

$$\tilde{G}_q(\omega) = \frac{1}{\omega^2 - \bar{\omega}_q^2 - i\Gamma_q} \cong \frac{1}{2\bar{\omega}_q(\omega - \bar{\omega}_q) - i\Gamma_q}, \tag{2.46}$$

and the spectral density in terms of the Green's function

$$\tilde{\rho}(\omega) = -\frac{2\bar{\omega}_q}{\pi}\sum_q Im\left[\tilde{G}_q(\omega)\right] \cong -\frac{1}{\pi}\sum_q \frac{\frac{\Gamma_q}{2\bar{\omega}_q}}{\left(\omega-\bar{\omega}_q\right)^2+\left(\frac{\Gamma_q}{2\bar{\omega}_q}\right)^2} \tag{2.47}$$

which leads, using the relationship $\tau^{-1} = -2Im\left[\Sigma\right]$ between lifetime and self-energy, to the identification $Jq = -\frac{\Gamma_q}{\bar{\omega}_q}$ as the phonon decay rate.

The method implemented is essentially a Fermi Golden Rule, including first-order one phonon to one phonon decay processes, but obviously neglects a large number of other mechanisms that may take place when the direct decay is forbidden. High frequency modes, characteristic of molecular vibrations, generally lay well beyond the vibrational bandwidth of the bulk reservoirs and cannot decay other than via one-to-many phonon channels [16,17]. Some of these effects can be taken into account introducing effective phonon densities for the contact modes [18]. This, for instance, allows the correct prediction of the temperature dependency of many-phonons decay rates. However, quantitative predictions of one-to-many phonons decay rates require the calculation of the coupling constants related, for instance, to anharmonic potentials which is not explicitly treated in this work. Other decay mechanisms may also be represented by vibrational coupling with the surrounding molecules and generally depend on the environment, or with multistep processes involving relaxations to lower energy modes via anharmonic couplings. Radiative decays may also play an important role.

2.5 Analytical model

It is useful to write the explicit expressions for E_q and A_q that can be obtained to lowest order of perturbation theory, assuming $T_L = T_R = 0$ and neglecting the self-energy in the vibron propagators. We introduce the notations

$$\begin{aligned} A_q^{\alpha,\beta} &= \tfrac{2}{\hbar}\int Tr[\gamma_q S_\alpha^*(E-\hbar\omega_q)\gamma_q S_\beta(E)] \\ &\quad \Theta(E-\mu_\beta)\Theta(\mu_\alpha - E + \hbar\omega_q)dE, \end{aligned} \tag{2.48}$$

$$\begin{aligned} E_q^{\alpha,\beta} &= \tfrac{2}{\hbar}\int Tr[\gamma_q S_\alpha^*(E+\hbar\omega_q)\gamma_q S_\beta(E)] \\ &\quad \Theta(E-\mu_\beta)\Theta(\mu_\alpha - E - \hbar\omega_q)dE, \end{aligned} \tag{2.49}$$

where the integration domain runs over the whole real axis, $\Theta(x)$ is the Heaviside step function and μ_α is the electrochemical potential of contact α. Finally, the spectral density matrix for the $\alpha-$contact is given by

$$S_\alpha(E) = G^r(E)\Gamma_\alpha(E)G^a(E), \tag{2.50}$$

where Γ_α is the imaginary part of the self-energy of contact α. In Eqs. (2.48) and (2.49) the labels α and β refer to incoherent processes in which an electron enters the molecule

from contact α and is scattered into contact β after absorption or emission of one vibrational quantum. The total absorption and emission can be expressed as $A_q = \sum_{\alpha,\beta\in L,R} A_q^{\alpha,\beta}$ and $E_q = \sum_{\alpha,\beta\in L,R} E_q^{\alpha,\beta}$, respectively. Higher order diagrams involve more vibrons as well as virtual absorption/emission processes, but for the sake of simplicity we present a qualitative analysis of the numerical calculations only considering the dominant first order terms. As the terms A_q and E_q depend non-linearly on N_q, the non-equilibrium population is computed with a self-consistent loop. For details about the Green's function method refer to Ref. [9]. With the definition $T_q^{\alpha\beta} = \frac{2}{\hbar} Tr\left[\gamma_q \tilde{S}_\alpha^* \gamma_q \tilde{S}_\beta\right]$ we find explicit expression for $E_q^{\alpha,\beta}$ and $A_q^{\alpha,\beta}$ within the Born Approximation

$$A_q^{\alpha,\beta} = n(\eta)\eta T_q^{\alpha\beta}\Theta(\eta)e^{\eta/K_bT_0} \tag{2.51}$$

$$E_q^{\alpha,\beta} = n(\eta)\eta T_q^{\alpha\beta}\Theta(\eta) \tag{2.52}$$

where $\eta = \hbar\omega_q - \mu_\alpha + \mu_\beta$. It's easy to show that $A_q^{\alpha,\beta} = E_q^{\alpha,\beta} e^{\eta/K_bT_0}$. For zero bias we have $\eta = \hbar\omega_q$ and we recover the equilibrium condition. Furthermore, if $T_q^{LR} = T_q^{RL}$, twe can use the following relationship, which holds even for non-bias

$$\sum_{\alpha,\beta}(A_q^{\alpha,\beta} - E_q^{\alpha,\beta}) = \hbar\omega_q \sum_{\alpha,\beta} T_q^{\alpha\beta} = \hbar\omega_q T_q \tag{2.53}$$

where $T_q = \sum_{\alpha,\beta} T_q^{\alpha\beta}$. The equality (2.53) turns Eq. (2.31) into

$$R_q = \frac{J_q}{J_q + \hbar\omega_q T_q}\left[E_q - n(\hbar\omega_q)\hbar\omega_q T_q)\right] \tag{2.54}$$

Based on the analytic equations derived above, we can analyze the dependence of the power dissipated and local temperature in molecular bridges for different choices of the relevant parameters characterizing the junction. In the calculations that follow we assume $T_{LL} = T_{LR} = T_{RL} = T_{RR}$, valid in the case of two identical metallic contacts. For Semiconducting contacts $T_{LL} = T_{RR} \approx 0$ because back-scattering with phonon absorptions is suppressed by the presence of the energy gap. T_{LR} represent a dimensionless parameter directly related to the phonon emission and absorption rates.

The attention is focused on the molecular temperature as a function of applied bias. In Fig. 2.3 the local temperature, T_{mol}, is plotted as a function of V for two different choices of the phonon energy (12 meV and 120 meV). A large sensitivity is found on the crucial parameter J_q and, as expected, higher temperatures are reached for lower J_q. We observe that the local temperature increases for higher mode frequencies and the temperature gradient between contacts and molecule decreases as the reservoir temperature increases. The first mechanism can be understood considering that keeping an identical electron-phonon coupling and dissipation rate, the system reaches the same number of steady state phonons, implying a larger local temperature. The second effect happens because for higher temperatures emission and absorption rate tend to balance, decreasing the net rate of phonon emission. We also observe that in the limit $eV/\hbar\omega_q \gg 1$ the molecular temperature becomes linear with bias, whereas

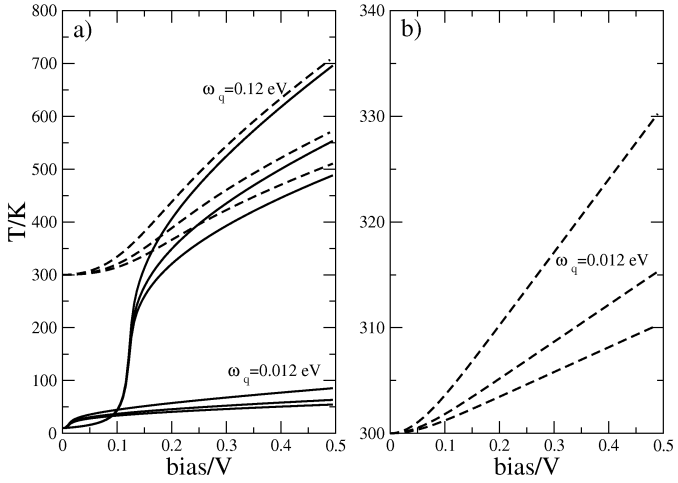

Figure 2.3: Molecular temperature vs bias for different parameters. Solid lines are for $T_0 = 10$ K, dashed lines for $T_0 = 300$ K. The two groups of three curves correspond to ω_q =12 meV and ω_q =120 meV, $J_q = 1 \cdot 10^{12} Hz, 2 \cdot 10^{12} Hz, 3 \cdot 10^{12} Hz$ and $T_{LR} = 10^{-3}$. Generally T_{mol} decreases as J_q rises.

the dependence is quadratic for low biases. This behavior can be easily recovered by inspection of Eq. (2.51) which, for large N_q, turns linear in V.

Fig. 2.3 reveals a sharp increase on the local temperature for biases larger than the mode frequency because emission assisted tunneling take place. When more modes are involved different steps at different characteristic frequencies may be expected, as shown in Fig. 2.4.

More phenomenological argumentations [19, 20] to calculate molecular temperatures under bias are based on the balance between the power emitted, assumed proportional to V^2 as in ohmic conductors, with the power dissipated into the contacts, assumed to behave as σT^4 like in the thermodynamic limit. This leads to a dependence of the junction temperature as $V^{\frac{1}{2}}$. In the present model the balance of power emitted and dissipated is microscopically defined mode by mode through the rate Eq. (2.4). In the limit of a continuous distribution of modes the power dissipated in the contacts can be written as

$$W_{diss} = \sum_q \hbar\omega_q J_q N_q = \int d\omega \rho(\omega) J(\omega) \frac{1}{e^{\beta\hbar\omega} - 1}, \tag{2.55}$$

where $\rho(\omega)$ is the phonon density of states. In Eq. (2.55) we assume that phonons population can be approximated by the Bose-Einstein distribution. The density of states of the acoustic phonon bands behaves as $\rho(\omega) = c$ for one-dimensional systems and as $\rho(\omega) = c\omega^2$ for three dimensional systems. Assuming a slow frequency dependent J, in the first case the dissipated power is proportional to T^2, whereas in the second case it is proportional to T^4, recovering the expected behavior of macroscopic systems. On the other hand, the dependence

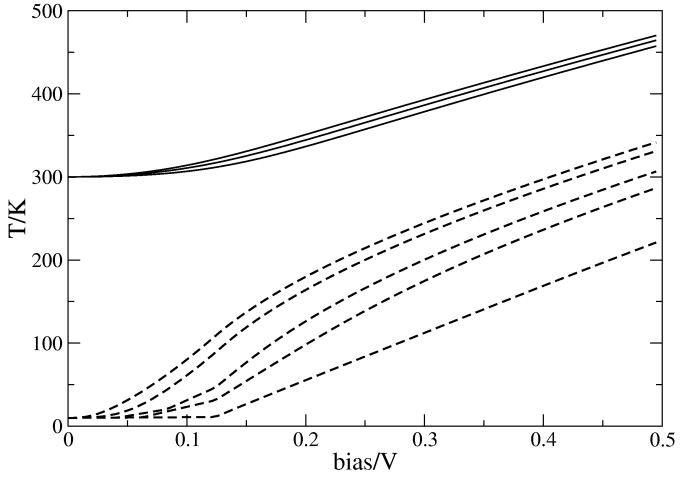

Figure 2.4: Molecular temperature vs bias for increasing number of modes uniformly distributed in the range $0 < \omega_q < 120$ meV, $J_q = 1 \times 10^{12}$Hz and $T_{LR} = 10^{-3}$.

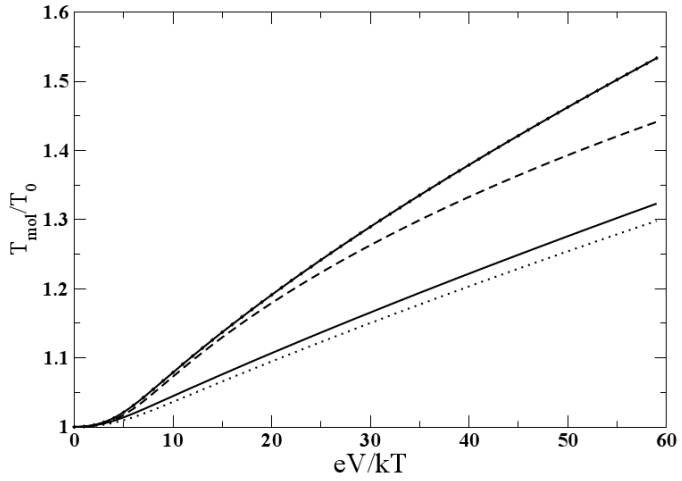

Figure 2.5: Molecular temperature vs bias for different distributions of molecular modes. The dashed line corresponds to a distribution $\rho \propto \omega^2$ with a Debeye cut-off $\omega_D = 5.74kT$. The dotted line corresponds to a constant distribution with identical cut-off. The solid lines correspond to one mode only, of energies $\omega_q = \omega_D/2$ (lower) and $\omega_q = 2\omega_D/3$ (higher), respectively. The other parameters are $J_q = 8 \cdot 10^{-5} kT/h$ and $T_{LR} = 10^{-7}$.

of the power emitted in the molecule, as expressed by $\sum_q R_q \hbar\omega_q$, is quadratic in V for low biases but becomes linear for large applied biases, irrespective of the number of vibrational modes or their distribution. This trends, contrasting the ohmic behavior, is an effect of the present model, which assumes that the incoherent current is just a small perturbation of the dominating coherent component and justifying that only one-phonon processes are taken into account. In this regime the power emitted behaves as $\sim \hbar\omega_q I_{inc} \sim \hbar\omega_q V$. In order to recover the ohmic limit, it should be necessary to consider a system much longer than the electron mean free path, such that coherent tunneling is suppressed and propagation is possible only via multiple phonon emissions, releasing all the energy provided by the applied bias. It is worth noting that in the coherent regime the excess energy provided by the bias is released at the collecting contact and is still proportional to V^2 (assuming $I \propto V$).

On the light of the discussion above, we deduce that, under the assumption of partially coherent tunneling, the molecular temperature should behave as $T_{mol} \sim V^2$ for low biases turning into $T_{mol} \sim V$ in case that only one or few vibrational modes absorb electron energy. Different trends like $T_{mol} \sim V^{1/2}$ or $T_{mol} \sim V^{1/4}$ are expected when many modes absorb similar amount of energy and their distribution is one-dimensional (first case) or bulk-like (second case). These different behaviors are shown in Fig. 2.5 in terms of dimensionless quantities. The mode distribution assumes a Debeye cut-off frequency, $\omega_D = 5.74kT$, which at room temperature corresponds to $1200cm^{-1}$, typical of many molecules.

For Semiconducting contacts $T_{LL} = T_{RR} \approx 0$ because back-scattering with phonon absorptions is suppressed by the presence of the energy gap. A discussion connecting this terms with phonon decay into electron-hole pairs is given in the Appendix. If we consider only the direct emission and absorption contributions we have

$$R_q = \frac{J_q T_q^{LR}}{J_q + \hbar\omega_q T_q^{LR}} \Gamma_q(V) \tag{2.56}$$

where

$$\Gamma_q(V) = n(\hbar\omega_q + eV)(\hbar\omega_q + eV) - n(\hbar\omega_q)(\hbar\omega_q) \tag{2.57}$$

Since most of the heat is carried trough low energy phonons which correspond to highest J_q we get a simple formule for the heat dissipates (or emitted)

$$P_q = \hbar\omega_q T_q^{LR} \Gamma_q(V) \tag{2.58}$$

Although Eq. (2.58) is not able to capture some interesting effects such as the heating due to resonances, it may estimate the order of magnitude of the power dissipated. Further investigation is needed to study the validity and limitations of this model.

2.6 Effect of resonant levels

The results of the previous section are valid in the limit when the energy dependence of the transmission function can be neglected. In this section we show the effect of considering a case where such assumption cannot be considered valid, such as for instance when a molecular level enters the tunneling energy window. In this case resonant tunneling and phonon

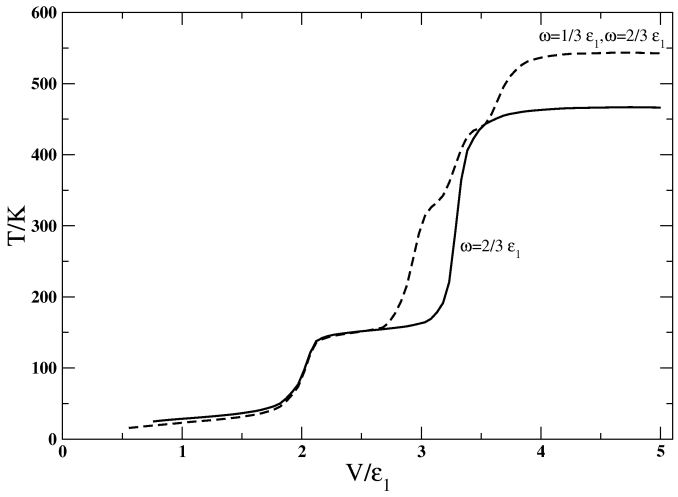

Figure 2.6: T_{mol} vs V for a system with a sharp resonating level located at energy ϵ_1 above the Fermi level for $V = 0$. The steps correspond to the biases that leads to a sharp enhancement of phonon emission due to assisted tunneling. The solid line is obtained assuming one mode, the dashed line assuming two modes.

assisted emission can take place, changing the qualitative behavior of T_{mol} vs V. The molecular resonance is modeled as a single peak, located off resonance at $V = 0$, at an energy ϵ_1 above the Fermi level. Two identical metallic contacts are assumed in this model whose results are shown in Fig. 2.6. As the bias increases up to $V = 2\epsilon_1$ the molecular resonance is brought into the tunneling window (a linear potential drop is assumed) where both coherent and incoherent transport are strongly enhanced, leading to a sharp increase of local temperature. A plateau follows, since the incoherent current levels up. A second rise appears when the bias matches the energy $eV = 2(\hbar\omega_q + \epsilon_1)$, corresponding to a second channel for transport assisted by phonon emission. When more modes are present, more features are expected, as seen in Fig. 2.6. Clearly for a continuous distribution of modes these features smear out, leaving a broadened step near $V = 2\epsilon_1$.

This example shows that the electronic density of states can introduce a richness of features in the molecular temperature as a function of bias. From this discussion we have skip the possibility of semiconducting contacts whose energy gap introduces other characteristic features such as NDR and negative differential heating whenever the tunneling resonances slip below the band edge.

Chapter 3

Thermal balance at the mesoscale

3.1 The Boltzmann Transport Equation for phonons

Whenever the system size is much larger than the wavelength of phonons we may adopt a classical approach for heat transport.

The behavior of a classical particle, under non-equilibrium conditions, can be obtained by the balance between the total derivative of its distribution function f and the collision operator $Q[f]$, i.e.

$$\frac{df(\mathbf{r},\mathbf{v},\mathbf{t})}{dt} = \partial_t f + (\partial_t x_i)\partial_{x_i} f + (\partial_t v_i)\,\partial_{v_i} f = Q[f] \tag{3.1}$$

Eq. (3.1) is the Boltzmann Transport Equation (BTE) and its steady state formulation, within the relaxation time approximation, is given by

$$v_i \partial_{x_i} f = \frac{f_0 - f}{\tau} \tag{3.2}$$

where f_0 is the equilibrium distribution and $v_i = (\partial_t x_i)$.

The BTE model can be applied to phonons by introducing the following transformation,

$$I(\omega) = \hbar\omega D(\omega) f \tag{3.3}$$

where I stands for the energy intensity per unit of solid angle and volume and $D(\omega)$ is the phonon density of states. If we further consider a heat source $\tilde{H}$, Eq. (3.2) becomes

$$\partial_{x_i}(v_i(\omega) I) = \frac{I_0 - I}{\tau(\omega)} + \tilde{H} \tag{3.4}$$

where I_0 is the equilibrium energy, which can be obtained by substituting the term f in Eq. (3.3) with the Bose-Einstain distribution. Eq. (3.4) is called the *phonon BTE* and should be solved accordingly with the phonon dispersion. In general, if the unit cell comprises q atoms, there will be one longitudinal (LA) and two transverse (TA) acoustic branches, $(q-1)$ longitudinal and $2(q-1)$ transverse optical branches. The symmetry can produce degeneracy

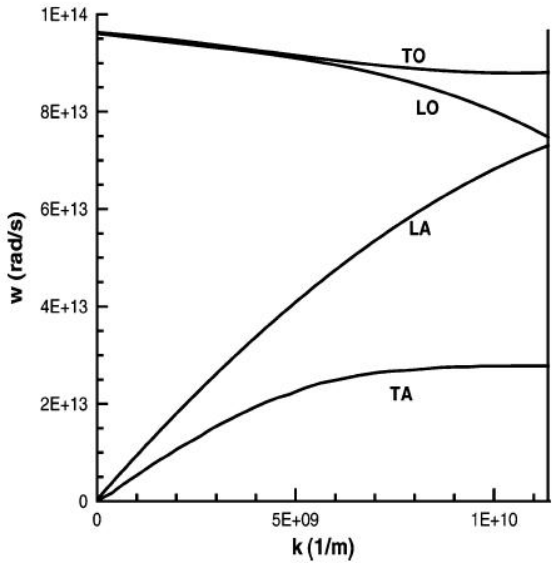

Figure 3.1: The Silicon phonon dispersion along the [001] direction.

of bands. For example, the Silicon phonon dispersion along the [001] direction is given in Fig. (5.1) [21].

The relaxation time takes into account the phonon-phonon interaction as well as the phonon-defect scattering. The phonon-phonon scattering can be either a normal (N) or umklapp process (U). In the first case the momentum is conserved and the collision does not reduce the thermal conductivity. In the U collision two phonons interact to form a third one whose wave vector is outside the first Brillouin zone. In this case the direction of propagation changes resulting in the reduction of thermal conductivity. The U processes are predominant above room temperature [1] and make the thermal conductivity decrease linearly. At low temperature the thermal conductivity drops because the heat capacity vanishes whereas the maximum value is reached at room temperature. To model numerically this trend the full phonon dispersion should be included in Eq. (3.2). In Fig. (3.2) a fit for the Silicon thermal conductivity [22] with data from [23] is reported.

In order to reduce the computational effort in solving the phonon BTE several approximations have been proposed in literature. A first approximation is to group the two transversal and the longitudinal optical phonons in one reservoir mode and consider only the longitudinal acoustic phonon as propagating mode. Due to their low group velocity, optical phonons do not contribute to the heat dissipation. The heat generation can be used as a source for the reservoir mode. This model is called the *semi-gray* model [24] and has been applied for the simulation of hotspots in MOSFET [25]. Another BTE based model splits the thermal flux in two controbution: the diffusive and ballistic part. This method defines the so called *ballistic-diffusive* equations [26].

The simplest model of the phonon BTE is obtained under the gray assumptions and it will

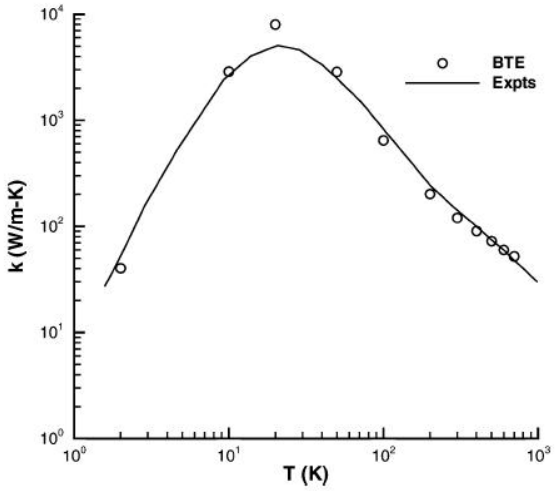

Figure 3.2: Lattice thermal conductivity of Silicon. A comparison between exeperimental [22] and numerical [23] data.

be the object of the next paragraph. A comparison of the BTE based heat transport models is reported in Ref. [27].

3.2 The gray model

In this work we adopt a simple BTE model which relies on the following assumptions: (i) collisions experienced by phonons are described via a relaxation time, which does not depend on the phonon energy (gray assumption). (ii) All phonons are considered to have the same group velocity, equal to the first sound velocity. Hereafter, we will refer to this model as the *gray* model.

Under the above assumptions Eq. (3.4) becomes

$$v_g s_i \partial_{x_i} I = \frac{I_0 - I}{\tau} + \tilde{H} \tag{3.5}$$

where v_g is the group velocity. The thermal flux is computed as

$$J_i = \int_{4\pi} I v_g s_i d\Omega \tag{3.6}$$

If we integrate both sides of Eq. (3.5) over the solid angle we have

$$\partial_{x_i} J_i = \int_{4\pi} \frac{I_0 - I}{\tau} d\Omega + H \tag{3.7}$$

where we have assumed that the versor **s** is divergence free and v_g is constant. Furthermore we have considered an isotropic heat source $\tilde{H} = 4\pi H$. Under the condition

$$I_0 = \frac{1}{4\pi}\int_{4\pi} I d\Omega \tag{3.8}$$

Eq. (3.7) becomes the continuity equation for the thermal flux. Eq. (3.8) is used in this work to achieve energy conservation. Eq. (3.5) is formally equivalent to the Energy Radiative Transfer (ERT) equation which is well suited for thermal radiation modeling. In ERT model, condition (3.8) is called *radiative equilibrium*. According to this analogy Eq. (3.5) is also named as the Energy Phonon Radiative Transfer (EPRT) equation.

Neglecting the full phonon dispersion may introduce unpredicting results in the temperature map [28]. However, the implementation of the gray model is part of a larger project, focused on the multiscale scheme rather on the detailed treatment of phonon transport.

Dirichlet boundary conditions impose the incoming phonon energy (with respect the simulation domain) to the desired value. Thermal insulating boundary condition can be applied by considering either specular or diffusive interfaces. The details about applying boundary condition on the gray model can be found in [29] As I_0 depends on the solution itself a self-consistent loop is needed.
In order to stabilize the numerical computation, we recast Eqs. (3.5)-(3.8) by a change of variable $\widetilde{T} = \frac{4\pi}{C} I + T_0$ into

$$\Lambda s_i \partial_{x_i} \widetilde{T} = T - \widetilde{T} + \frac{\tau}{C} H \tag{3.9}$$

$$T = \frac{1}{4\pi}\int_{4\pi} \widetilde{T} d\Omega \tag{3.10}$$

The heat flux expressions becomes

$$J_i = \frac{C v_g}{4\pi}\int_{4\pi} \widetilde{T} v_i s_i d\Omega \tag{3.11}$$

where we used the relationship $\Lambda = v_g \tau$.
The first guess of the equilibrium energy density is a crucial point to speed up the convergence. We found that if we first perform a Fourier simulation and take the resulting equilibrium energy as the first energy guess, convergence can be reached within few steps. The overall algorithm is summarized in Fig. 3.3.

3.3 Angular discretization

The gray model requires the discretization of the solid angle. Eq. (3.9) should be solved for each slice of solid angle, namely

$$\int_{\Delta\Omega_k} \Lambda s_i^k \partial_{x_i} \widetilde{T} d\Omega = \int_{\Delta\Omega_k} (T - \widetilde{T}) d\Omega + \frac{\tau}{C}\int_{\Delta\Omega_k} H d\Omega \tag{3.12}$$

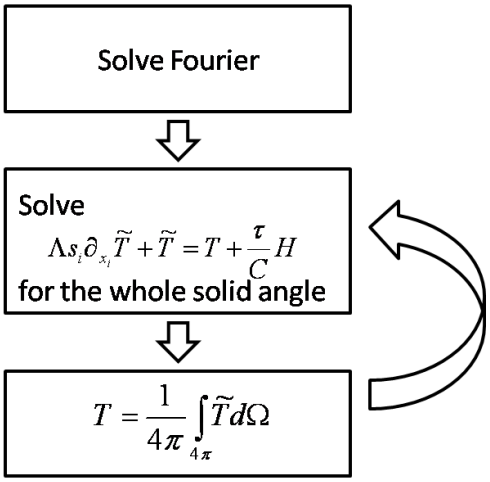

Figure 3.3: The algorithm of the gray model.

where, according to Fig. 3.4, the versor $\mathbf{s^k}$ is

$$\mathbf{s^k} = \begin{bmatrix} \sin(\theta_k)\sin(\phi_k) \\ \sin(\theta_k)\cos(\phi_k) \\ \cos(\theta_k) \end{bmatrix} \tag{3.13}$$

Eq. (3.9) can be written as

$$\Lambda S_i^k \partial_{x_i} \widetilde{T} + \widetilde{T}\Delta\Omega_k = \left(\frac{\tau}{C} H + T\right) \Delta\Omega_k \tag{3.14}$$

where

$$\Delta\Omega_k = \int_{\phi_k - \frac{\Delta\phi}{2}}^{\phi_k + \frac{\Delta\phi}{2}} \int_{\theta_k - \frac{\Delta\theta}{2}}^{\theta_k + \frac{\Delta\theta}{2}} \sin(\theta) d\theta d\phi = 2\sin(\theta)\sin(0.5\Delta\theta)\Delta\phi \tag{3.15}$$

and

$$\mathbf{S^k} = \int_{\phi_k - \frac{\Delta\phi}{2}}^{\phi_k + \frac{\Delta\phi}{2}} \int_{\theta_k - \frac{\Delta\theta}{2}}^{\theta_k + \frac{\Delta\theta}{2}} \mathbf{s^k} d\theta d\phi \begin{bmatrix} \sin(\phi_k) * \sin(0.5\Delta\phi)\left[\Delta\theta - \cos(2\theta_k)\sin(\Delta\theta)\right] \\ \cos(\phi_k) * \sin(0.5\Delta\phi)\left[\Delta\theta - \cos(2\theta_k)\sin(\Delta\theta)\right] \\ 0.5\Delta\theta \sin(2\theta_k)\sin(\Delta\phi) \end{bmatrix} \tag{3.16}$$

After some algebraic manipulation of Eq. (3.14) we obtain

$$\gamma_k S_i^k \partial_{x_i} \widetilde{T} + \widetilde{T} = \frac{\tau}{C} H + T \tag{3.17}$$

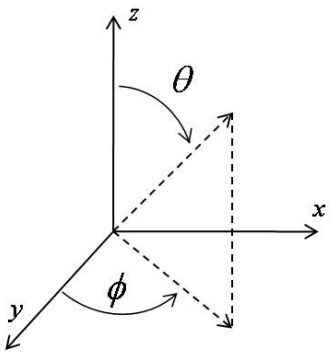

Figure 3.4: Spherical coordinates

where $\gamma_k = \frac{\Lambda}{\Delta\Omega_k}$. Once the Eq. (3.17) is solved for each slice of solid angle we can compute T as

$$T = \frac{1}{4\pi}\sum_k T_k \Delta\Omega_k \tag{3.18}$$

where $T_k = \widetilde{T}(\Omega_k)$. In the same way, the thermal flux is computed as

$$J_i = v_g \sum_k T_k S_i^k \tag{3.19}$$

Eqs. (3.17)-(3.18) have to be solved in a self-consistent way.

3.4 Spatial discretization

The Finite Element method has long been used in solving partial differential equations. Several methods have been developed in order to improve the convergence and a stability for a given problem and mesh type. The method used to solve Eq. (3.17) is the Discontinuous Galerkin (DG). Contrary to standard FEM, a DG discretization provides a stable method in solving first order differential equations on unstructured grids. The DG method was originally introduced for linear advection problems and, afterwards, extended to solve diffusion problems. The DG has established itself as an alternative to the continuous FEM where the latter does not work well. For details about the DG method see Ref. [30].

For a given direction Ω_k we write Eq. (3.17) as

$$\begin{aligned} b_i \partial_{x_i}\widetilde{T} + \widetilde{T} &= f \qquad \mathbf{x} \in \Omega \\ \widetilde{T} &= g \qquad \mathbf{x} \in \Gamma^- \end{aligned} \tag{3.20}$$

$\mathbf{b} = \gamma_k \mathbf{s}^k$, $f = \frac{\tau}{C}H + T$ and $\Omega \subset R^d$ ($d \leq 3$) is a bounded domain with boundary Γ. The *inflow boundary* Γ_- is defined as

$$\Gamma_- = \{\mathbf{x} \in \Gamma : (\mathbf{b}^k \cdot \mathbf{n}) < 0\} \tag{3.21}$$

where $\mathbf{n}$ is the outer normal on Γ.
Let us partition the domain Ω into elements E_h with $h > 0$. For each element we split its boundary ∂E into the inflow and outflow part by (see Fig. 3.5):

$$\begin{aligned} \partial E^+ &= \{\mathbf{x} \in \partial E \,:\, (\mathbf{s}\cdot\mathbf{n})(\mathbf{x}) < 0\}, \\ \partial E^- &= \{\mathbf{x} \in \partial E \,:\, (\mathbf{s}\cdot\mathbf{n})(\mathbf{x}) > 0\}, \end{aligned} \tag{3.22}$$

We associate to the element E_h the function space

$$V_h = \{\varphi : \varphi \text{ is a bounded function on } \Omega \text{ and } \varphi \in P_r(E_h)\} \tag{3.23}$$

where $P_r(E_h)$ is the space of polynomials on K of degree at most $r \geqslant 0$. We further introduce

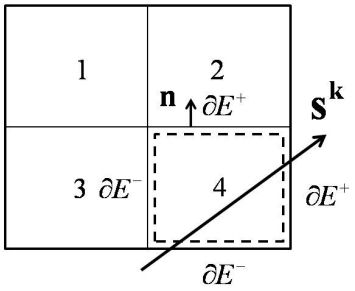

Figure 3.5: Partitioned domain

the following notation

$$\varphi^-(\mathbf{x}) = \lim_{\epsilon \to 0^-} \phi(\mathbf{x} + \epsilon \mathbf{b}) \tag{3.24}$$

$$\varphi^+(\mathbf{x}) = \lim_{\epsilon \to 0^+} \phi(\mathbf{x} + \epsilon \mathbf{b}) \tag{3.25}$$

Now, the DG method for Eq. (3.20) is defined as follows: For the element E_α, given $\widetilde{T}_h^-$ on ∂E_h^-, find $\widetilde{T}_h \in P_r(E_h)$ such that

$$\begin{aligned} \int_{E_\alpha} b_i(\partial_{x_i}\widetilde{T})\varphi_h dV - \int_{\partial E_\alpha^-} \widetilde{T}^+ \varphi_h^+ b_i n_i dS \\ \int_{E_\alpha} f\varphi_h dV - \int_{\partial E_\alpha^-} \widetilde{T}^- \varphi_h^+ b_i n_i dS \end{aligned} \tag{3.26}$$

Note that Eq. (3.26) is the standard FEM for Eq. (3.5) on the element E_h, with *weak* boundary condition.
If $\mathbf{b}$ is divergence-free we can use the Green's formula to show that

$$\begin{aligned} \int_{E_\alpha} b_i(\partial_{x_i}\widetilde{T})\varphi_h dV = \int_{\partial E_\alpha^-} \widetilde{T}^+ \varphi_h^+ b_i n_i dS + \int_{E_\alpha} \widetilde{T}\varphi_h dV = \\ + \int_{\partial E_\alpha^+} \widetilde{T}^- \varphi_h^- s_i n_i dS - \int_{E_\alpha} \widetilde{T} s_i \partial_i \varphi_h dV \end{aligned} \tag{3.27}$$

By inserting the expression (3.27) in Eq. (3.26) we have

$$-\int_{E_\alpha}\widetilde{T}(b_i\partial_{x_i}\varphi_h)dV+\int_{\partial E_\alpha^+}\widetilde{T}^-\varphi_h^-(b_in_i)dS+\int_{E_\alpha}\widetilde{T}\varphi_h dV= \int_{E_\alpha}f\varphi_h dV-\int_{\partial E_\alpha^-}\widetilde{T}^-\varphi_h^+(b_in_i)dS \tag{3.28}$$

We chose zeroth-order polynomial functions such as

$$\varphi_h(\mathbf{x})=\begin{cases}1, & \text{if } \mathbf{x}\in E_h\\ 0, & \text{elsewhere}\end{cases} \tag{3.29}$$

With the function space (3.29), Eq. (3.28) becomes

$$\int_{\partial E_\alpha}\gamma_k\widetilde{T}^-(b_in_i)dS+\int_{E_\alpha}\widetilde{T}dV=\int_{E_\alpha}f\,dV \tag{3.30}$$

The expansion

$$\widetilde{T}(\mathbf{x})=c_\beta\varphi_\beta(\mathbf{x}) \tag{3.31}$$

allows Eq. (3.30) to be written in terms of a stiffness and load matrix

$$A_{\alpha\beta}=\delta_{\alpha\beta}\left[\int_{\partial E_\alpha^+}\gamma_k(b_in_i)dS+V_\alpha\right]+ \tag{3.32}$$

$$+\int_{\partial E_\alpha^-\cap\partial E_\beta^+}\gamma_k(b_in_i)dS \tag{3.33}$$

$$F_\alpha=\int_{E_\alpha}f dV \tag{3.34}$$

where V_α is the volume of the element E_α.
Finally, recalling that $\mathbf{b}=\frac{\Lambda}{\Delta\Omega_k}\mathbf{S^k}$ and $f=\left(\frac{\tau}{C}H+T\right)$ we have

$$A_{\alpha\beta}=\delta_{\alpha\beta}\left[\frac{\Lambda}{\Delta\Omega_k}\int_{\partial E_\alpha^+}(S_i^kn_i)dS+V_\alpha\right]+ \tag{3.35}$$

$$+\frac{\Lambda}{\Delta\Omega_k}\int_{\partial E_\alpha^-\cap\partial E_\beta^+}S_i^kn_idS \tag{3.36}$$

$$F_\alpha=\int_{E_\alpha}\left(\frac{\tau}{C}H+T\right)dV \tag{3.37}$$

3.5 Heat transport regime

The heat transport regime for a structure of length L can be identified by the Knudsen number, defined as $Kn = \frac{\Lambda}{L}$. It is a useful quantity which provides the device length in terms of the phonon mean free path.
When the rod length is much smaller than the phonon mean free path, namely for a large Knudsen number $Kn = \frac{\Lambda}{L} >> 1$ we are close to the ballistics regime. This case, in analogy with the thermal radiation problem, is called the *acoustically thin* limit.
Conversely, whenever the phonon mean free path is much smaller than the device length, i.e. $Kn << 1$, we approach the diffusive regime. This condition is called *acoustics thick* limit.
Let us start to investigate the *acoustically thin* limit for a planar structure of length L (See Fig. 3.6) without any heat source. The plane ends with two walls maintained at two different temperatures $T(0)$ and $T(L)$.

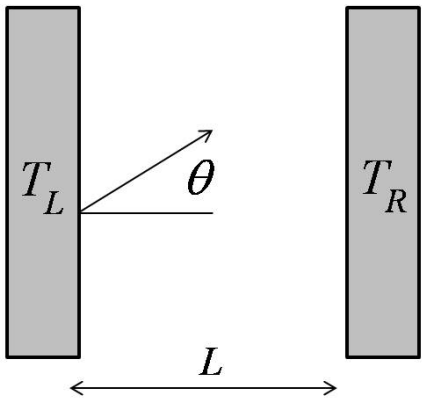

Figure 3.6: Planar domain.

We split the heat flux into two contributions

$$\begin{aligned} \Lambda\mu\partial_{x_i}\widetilde{T}^{+} &= T - \widetilde{T} \qquad 0 < \mu < 1 \\ \Lambda\mu\partial_{x_i}\widetilde{T}^{-} &= T - \widetilde{T} \qquad -1 < \mu < 0 \end{aligned} \tag{3.38}$$

and

$$\begin{aligned} \widetilde{T}^{+}(0) &= T_L \\ \widetilde{T}^{-}(L) &= T_R \end{aligned} \tag{3.39}$$

The formal solutions are [1]

$$\widetilde{T}^{+}(x,\mu) = T_L e^{-\frac{x}{\Lambda\mu}} + \frac{1}{\Lambda\mu}\int_0^x T(\zeta) e^{-\frac{x-\zeta}{\Lambda\mu}} d\zeta \tag{3.40}$$

$$\widetilde{T}^{-}(x,\mu) = T_R e^{\frac{L-x}{\Lambda\mu}} + \frac{1}{\Lambda\mu}\int_x^L T(\zeta) e^{-\frac{x-\zeta}{\Lambda\mu}} d\zeta \tag{3.41}$$

In Eqs. (3.40)-(3.41) the first terms represent the intensity generated by the surfaces and attenuated by the medium whereas the second terms are the internal contributions which are attenuated, as well.

Accordingly to Eq. (3.11), the heat flux is computed as

$$J(x) = \frac{v_g C}{4\pi} 2\pi \int_0^1 \left[T^+(x,\mu) - T^-(x,\mu)\right] d\mu = J_1 + J_2 \tag{3.42}$$

where

$$J_1 = \frac{v_g C}{2} T(0) E_3\left(\frac{x}{\Lambda}\right) - \frac{v_g C}{2} T(L) E_3\left(\frac{L-x}{\Lambda}\right) \tag{3.43}$$

$$J_2 = \frac{v_g C}{2\Lambda} \int_0^x T(x) E_2\left(\frac{x-\zeta}{\Lambda}\right) d\zeta - \frac{v_g C}{2\Lambda} \int_x^L T(x) E_2\left(\frac{x-\zeta}{\Lambda}\right) d\zeta \tag{3.44}$$

In Eq. (3.42) the azimutal and polar symmetries were used. The function

$$E_m(x) = \int_0^1 \mu^{m-2} e^{-\frac{x}{\mu}} d\mu \tag{3.45}$$

is the $mth-$exponenetial integral.

The surface contributions are expected to be predominant and, therefore, the term J_2 in Eq. (3.43) can be neglected. Furthermore, we approximate $\frac{x}{\Lambda} \approx 0$ and $\frac{L-x}{\Lambda} \approx 0$ The heat flux then becomes

$$J(x) = -\frac{v_g C L}{4}\left(\frac{T(0) - T(L)}{L}\right) \tag{3.46}$$

where $\boldsymbol{E}_3(0) = \frac{1}{2}$ is used.
The effective thermal conductivity is

$$k_B = \frac{v_g C L}{4} \tag{3.47}$$

Hereafter, we will refer to K_B as the *ballistic thermal conductivity*.

Now we treat the case when $Kn << 1$, namely, the *acoustically thick* limit. In thic case we can neglect the term J_1. We impose $z = \frac{x-\zeta}{\Lambda}$ and use the expansion $I_0(x) = I_0(\zeta) + \partial_x I_0(x)(x-\zeta) = I_0(\zeta) + (\partial_x I_0(x)) z\Lambda$. The term J_2 is

$$J(x) = -\frac{C v_g \Lambda}{2} \Lambda \left[\partial_{x_i} T(x)\right] \left[\int_0^{\frac{x}{\Lambda}} E_2(z) dz + \int_0^{\frac{x-L}{\Lambda}} E_2(z) dz\right] \tag{3.48}$$

We may assume that $\frac{x}{\Lambda} \approx \infty$ and $\frac{x-L}{\Lambda} \approx \infty$. Under these assumptions we have

$$J(x) = -\frac{C v_g \Lambda}{3} \Lambda \left[\partial_{x_i} T(x)\right] \tag{3.49}$$

where $\int_0^\infty E_2(z) dz = \frac{1}{3}$ is used. The effective thermal conductivity is

$$k_D = \frac{v_g C \Lambda}{3}. \tag{3.50}$$

which consistent with the Kinetics result. We will refer to it as the *diffusive thermal conductivity*. In the intermediate regime the effective thermal conductivity can be computed empirically as the parallel κ_B in parallel with κ_D

$$k = \frac{k_B k_D}{k_B + k_D} \tag{3.51}$$

In the following we will see whether Eq. (3.51) is a good approximation.

3.6 1-D numerical Solution

In this section we will solve numerically the *gray* model for a 1D system. Let us partition a 1D rod in M elements of length L_α where $\alpha = 1, 2...M$. The left and the right ends have a fixed temperature of $T(0)$ and $T(L)$, respectively.
Referring to the Eqs. (3.35)-(3.37), for a given direction k, we have

$$A_{\alpha\beta} = \left[\frac{v_g \tau \cos(\theta_k)}{\Delta\theta_k} + L_\alpha\right]\delta_{\alpha\beta} - \frac{v_g \tau \cos(\theta_k)}{\Delta\theta_k}\delta_{(\alpha-1)\beta} \tag{3.52}$$

$$F_\alpha = \int_{E_\alpha} \left(\frac{\tau}{C}H + T\right) dL \tag{3.53}$$

The boundary conditions are fixed for the incoming flux into the domain.
Solving the system $A_{\alpha\beta}C_\beta = F_\alpha$ means solving

$$\frac{v_g \tau \cos(\theta_k)}{\Delta\theta_k}\frac{T_\alpha - T_{\alpha-1}}{L_\alpha} + T_\alpha = \frac{1}{L_\alpha}\int_{E_\alpha} \left(\frac{\tau}{C}H + T\right) dL \tag{3.54}$$

for each element α. The boundary value T_0 depends on the direction of propagation

$$T_0 = \begin{cases} T_0, & \cos(\theta_k) > 0 \\ T(L), & \cos(\theta_k) < 0 \end{cases} \tag{3.55}$$

In Fig. 3.7 the quantity $T^* = \frac{T - T(0)}{T(L) - T(0)}$ is plotted for different Knudsen numbers. The normalized position is $x^* = \frac{x}{L}$. As one can see, the smaller the Knudsen number the bigger is the jump in temperature at the boundaries. This behavior can be observed also between boundaries of different materials and is interpreted as a Thermal Boundary Resistance (TBR). This is due to different acoustic properties between materials. The TBR is present even in a perfectly matched interface. It is often called the *Kapitza* resistance. TBR exists between two dielectrics as well as between a dieletric and a metal. A review can be found in [31].
In Fig. 3.8 a comparison between the ballistic and diffusive thermal conductivities is provided. Unlike the diffusive conductivity, the ballistic thermal conductivity depends on the device length. The two conductivities reach the same value when $Kn = \frac{1}{2}$. The green line is the thermal conductivity computed as

$$k = -\frac{J}{T(0) - T(L)} \tag{3.56}$$

As one can expect its value approaches the diffusive and ballistic regime for extreme values of the Knudsen number. The value of k as computed by Eq. (3.56) is pretty similar to that computed by Eq. (3.51).

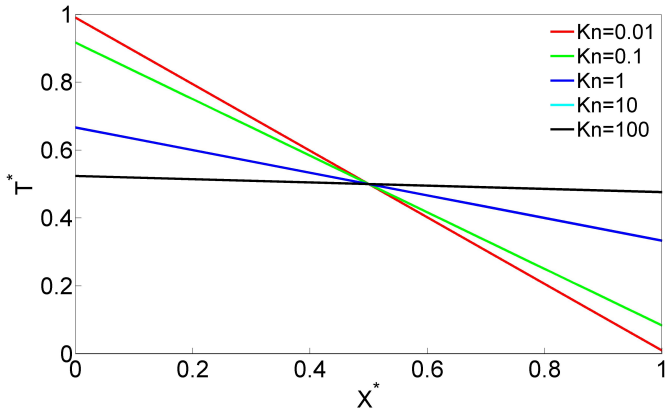

Figure 3.7: Temperature profile at different Knudsen number.

3.7 Fourier/Gray Interface

The aim of a multiscale model is to couple different physical models in order to get an accurate description without strongly increasing the computational effort. In principle, we might perform the gray model over all the whole simulation domain but the discretization of the solid angle and the non-linear term in the right hand side (see Eq.(3.10)) strongly increase the computational cost. For this reason we compute the BTE only in the region where it is needed (meso domain) and the Fourier model is adopted in the remaining part of the device (macro domain)(see Fig. 3.9). Both models can communicate by means of their boundary conditions. Hence, we adopt the *bridge* scheme. The temperature calculated with the Fourier model serves as Dirichlet boundary conditions for the gray model. The thermal flux computed by the gray model acts as Neumann boundary condition for the Fourier model [32].

Whenever the gray domain is much larger than the phonon mean free path, the convergence becomes very slow. Now we analyze the convergence behavior of this scheme. Let us assume to have a rod of length $2L$ where the left side is maintained at a dimensionless temperature $T = 1$. We split the domain in two subdomains with equal lenght. The Fourier model is performed on the left subdomain whereas on the right subdomain we perform the gray model. Let $T_I^{(n)}$ be the temperature on the Fourier/BTE interface at the nth-iteration expressed as

$$T_I^{(n)} = 1 + \frac{J_m^{(n-1)}}{k_M} L \tag{3.57}$$

where $J_m^{(n-1)}$ is the thermal flux along the micro domain at the $(n-1)th$ step given by

$$J_m^{(n-1)} = -\frac{\kappa_m}{L} T_I^{(n-1)} \tag{3.58}$$

The values of $J_m^{(n)}$ and $T_I^{(n)}$ are show in Tab. (3.7)

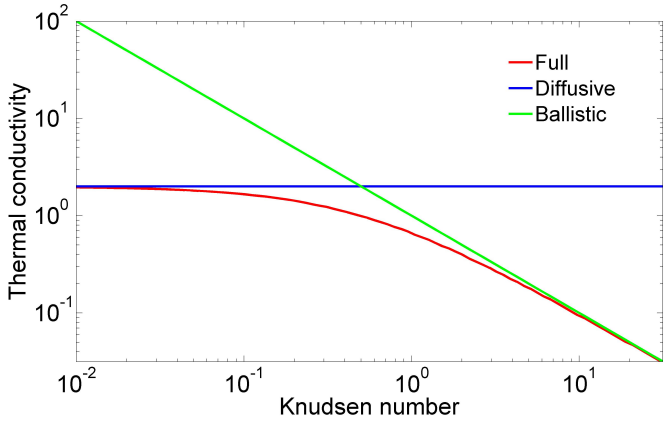

Figure 3.8: Lattice thermal conductivity at different Knudsen number.

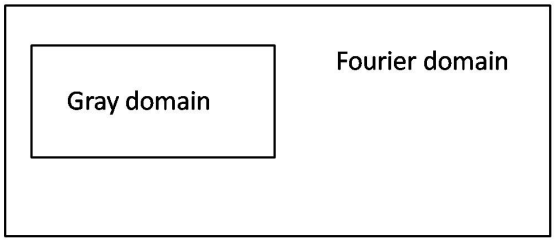

Figure 3.9: Domain partitioning in a bridge scheme

n	$T_I^{(n)}$	$J_m^{(n)}$
0	1	$-\frac{\kappa_m}{L}$
1	$1-\gamma$	$-\frac{\kappa_m}{L}(1-\gamma)$
2	$1-\gamma+\gamma^2$	$-\frac{\kappa_m}{L}(1-\gamma+\gamma^2)$
...	...	...
n	$\sum_{k=0}^{n}(-1)^k\gamma^k$	$-\frac{\kappa_m}{L}\left[\sum_{k=0}^{n}(-1)^k\gamma^k\right]$

where $\gamma = \frac{\kappa_m}{\kappa_M}$.
Relying on the Leibniz criterium, the series $\sum_{k=0}^{n}(-1)^k\gamma^k$ converges only if γ^k is monotonic decreasing and $\lim_{k\to\infty}\gamma^k = 0$. As $k_m < k_M$ (see Fig. 3.8), $\gamma < 1$ and the convergence condition is satisfied.

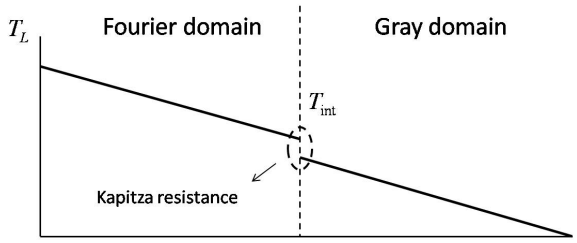

Figure 3.10: One dimensional multiscale domain

The convergence value is

$$T_I = \lim_{n\to\infty} T_I^{(n)} = \frac{1}{1+\frac{k_m}{k_M}} \tag{3.59}$$

$$J = \lim_{n\to\infty} J_m^{(n)} = -\frac{k_m}{L}\frac{1}{1+\frac{k_m}{k_M}} \tag{3.60}$$

It's straightforward to show that for a general T_L and T_R we have

$$T_I = (T_L+T_R)\frac{k_M}{k_m+k_M} \tag{3.61}$$

$$J = -\frac{T_L-T_R}{2L}\frac{2k_mk_M}{k_m+k_M} \tag{3.62}$$

For $\kappa_m = \kappa_M = \kappa$ we recover the standard situation

$$T_I = \frac{T_L+T_R}{2} \tag{3.63}$$

$$J = -\kappa\frac{T_L-T_R}{2L} \tag{3.64}$$

For small Knudsen number, i.e., $\kappa_m \approx \kappa_M$ (see Fig.3.8), the whole loop may require several steps. A workaround of this problem is to solve first the Fourier model on the whole domain. The resulting temperature profile is used to set the temperature at the interface and to provide the initial guess of the equilibrium energy for the gray model.
The scheme is summarized in Fig. 3.11. The loop error is based on the equilibrium density energy and the power balance.

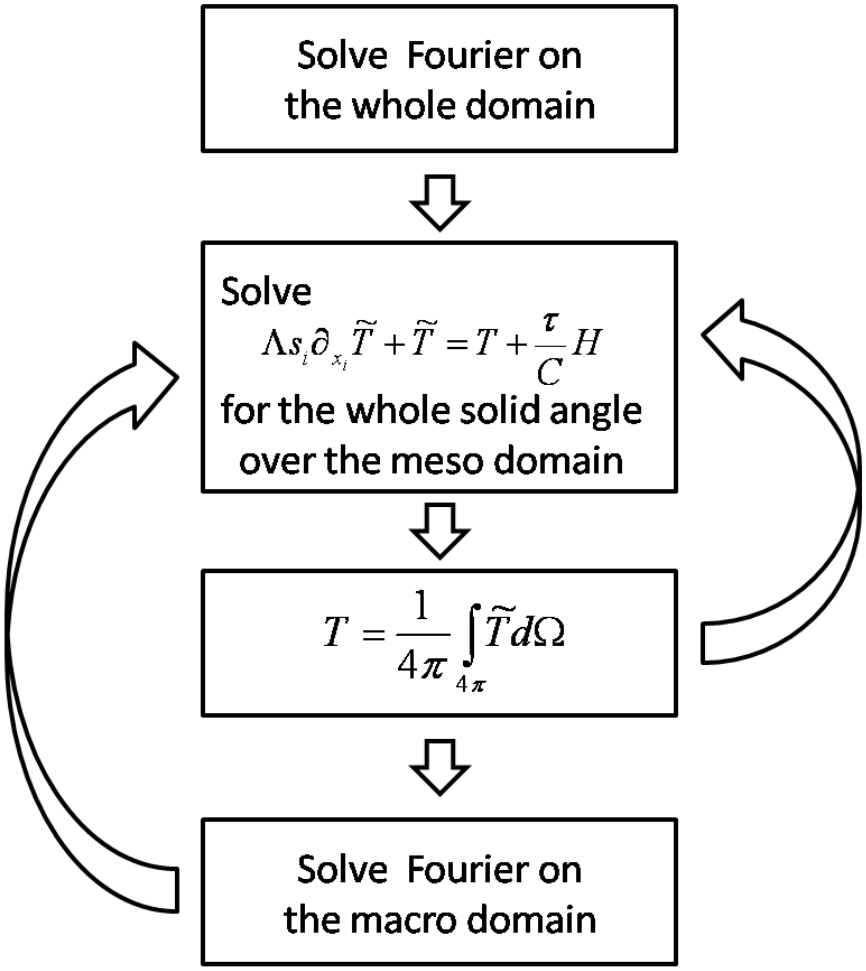

Figure 3.11: The scheme for the gray model

Chapter 4

Thermal balance at the macroscale

4.1 Transport equation

Transport phenomena in continuous media are governed by irreversible thermodynamics. In principle, for a system under non-equilibrium conditions we cannot use the relationship related to the thermodynamics. However, for system not so far from the equilibrium condition we may divide the domain in small subdomains where the physics regarding the thermodynamic equilibrium still holds (see Fig. 4.1). More precisely, if (i) each subsystem is at equilibrium indipendently of the other subsystems, (ii) interactions between neighboring subsystems are weak, we have a *local equilibrium* [33]. Now we may apply what has been

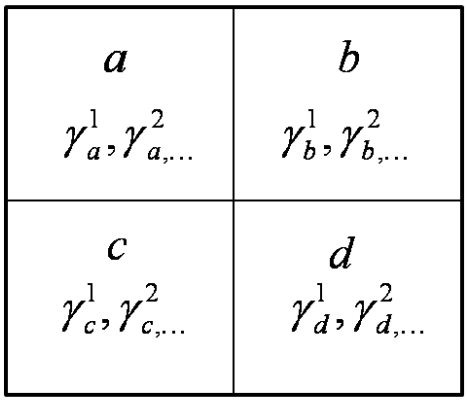

Figure 4.1: Subdomains with different intensive variables.

already developed for systems in equilibrium conditions.

For a small subdomain we apply the energy conservation law

$$dS = \sum_i \gamma^i dA^i \tag{4.1}$$

where A_i are the extensive variables and γ_i are the conjugate intensive variable. We recall that, in thermodynamics, the extensive variables depend on the size of the system, i. e. the number of particles, the internal energy etc.... Conversely, the intensive variables are related to quantities which does not depend on the size of the system.

In order to get the entropy flux we divide both sides of Eq. (4.1) by a unit surface and time and let the subdoomains tend to an infinitesimal region

$$J_i^s = \sum_\alpha \gamma_i J_i^\alpha \tag{4.2}$$

The terms J_i^α are the flux of the extensive variables. The continuity equation for the entropy flux in its steady state condition (hereafter we will consider only steady state conditions) reads as

$$S_{tot} = \partial_{x_i} J_i^s \tag{4.3}$$

where

$$S_{tot} = \sum_i \gamma_i A_i \tag{4.4}$$

is the total entropy production. To get Eq. (4.4) we used the relationship 4.1. Each flux appearing in the right hand side of Eq. 4.3 must satisfy own continuity equation which read as

$$\partial_{x_i} J_i^s = \sum_\alpha J_i^\alpha \partial_{x_i} \gamma^\alpha \tag{4.5}$$

The above equation assumes that there is no source of the extensive quantities, i.e. $\partial_{x_i} J_i^\alpha = 0$ The terms $\mathbf{F^{ff}} = \nabla \gamma^\alpha$ are called *affinities*.

So far we have set up the relationship between the entropy flux and the extensive variable fluxes. But we have not mentioned how we may compute the latter, yet.

Let us assume that for a small gradient of the intensive variable γ^α there exist a flux of the extensive variable A^α, linearly proportional to the related affinity $\mathbf{F^{ff}}$. In general we may have a full coupling among all variables, i.e.

$$J_i^\alpha = L_{ij}^{\alpha\beta} F_j^\beta \tag{4.6}$$

where $L_{ij}^{\alpha\beta}$ are the *transport coefficients*. The Onsager theorem states that, in absence of a magnetic field, we have $L_{ij}^{\alpha\beta} = L_{ij}^{\beta\alpha}$ [34]. This relationship, called the *Onsager reciprocal relationship*, will be used in the next paragraph in order to get the transport coefficients of interests.

4.2 The transport coefficients

In a full electro-thermal simulation of a continuous media in the diffusive regime we have three kind of particles: electrons, holes and phonons. The first two carry energy and matter, the second involves only transport of energy. The conjugate intensive variables can be computed directly from the thermostatic theory [33]. In Tab. 4.2 the relative expressions are reported.

Description	γ^α	A^α	$\mathbf{J}$
electrons energy	$\frac{1}{T_n}$	U_n	$\mathbf{J_{nu}}$
holes energy	$\frac{1}{T_p}$	U_p	$\mathbf{J_{pu}}$
lattice energy	$\frac{1}{T_L}$	U_L	$\mathbf{J_{Lu}}$
electrons concentration	$\frac{\phi_n}{T_n}$	n	$\mathbf{J_n}$
holes concentration	$\frac{\phi_p}{T_p}$	p	$\mathbf{J_p}$

In Tab. 4.2 T_n, ϕ_n and $\mathbf{J_{nu}}$ are the electron temperature, electro-chemical potential and energy flux, respectively. The p-labeled analogue quantities refer to holes. T_L is the lattice temperature and $\mathbf{J_{Lu}}$ the thermal flux carried by phonons.

At thermodynamic equilibrium $\phi_n = \phi_p = const$ and $T_n = T_p = T_L = const$.

Now we use the relationship (4.6) to build the transport equations

$$\begin{pmatrix} \mathbf{J_n} \\ \mathbf{J_p} \\ \mathbf{J_{nu}} \\ \mathbf{J_{pu}} \\ \mathbf{J_{Lu}} \end{pmatrix} = \begin{pmatrix} L_{11} & L_{12} & L_{13} & L_{14} & L_{15} \\ L_{12} & L_{22} & L_{23} & L_{24} & L_{25} \\ L_{13} & L_{23} & L_{33} & L_{34} & L_{35} \\ L_{14} & L_{24} & L_{33} & L_{34} & L_{45} \\ L_{15} & L_{25} & L_{35} & L_{45} & L_{55} \end{pmatrix} \cdot \begin{pmatrix} \nabla\left(\phi_n/T_n\right) \\ \nabla\left(\phi_p/T_p\right) \\ \nabla\left(\frac{1}{T_n}\right) \\ \nabla\left(\frac{1}{T_p}\right) \\ \nabla\left(\frac{1}{T_L}\right) \end{pmatrix} \tag{4.7}$$

Generally speaking, we have fifteen coefficients. However, in our calculation we consider only the coefficients L_{11}, L_{13}, L_{22}, L_{33}, L_{21}, L_{24} and L_{55}. We further assume the charge carrier to be at thermal equilibrium with the lattice, i.e. $T_n = T_p = T_L = T$. These coefficients may be derived from the Boltzmann Equation as in [35] and are reported below (assuming isotropic

material)

$$\begin{aligned}
L_{11} &= n\mu_n T \\
L_{13} &= -n\mu_n T\left(\frac{\varphi_n}{q} - P_n T\right) \\
L_{33} &= \kappa_n T^2 + n\mu_n T\left(\frac{\varphi_n}{q} - P_n T\right)^2 \\
L_{21} &= p\mu_p T \\
L_{23} &= -p\mu_p T\left(\frac{\varphi_p}{q} - P_p T\right) \\
L_{44} &= \kappa_p T^2 + p\mu_p T\left(\frac{\varphi_p}{q} - P_p T\right)^2 \\
L_{55} &= \kappa_L T^2
\end{aligned}$$

where κ_n, κ_p and κ_L are the thermal conductivity of electrons, holes and lattice, respectively. From kinetic theory they can be computed as

$$\kappa_L = \frac{1}{3}\tau v_g^2 C \tag{4.8}$$

$$\kappa_n = \mu_n q\, T\, L \tag{4.9}$$

$$\kappa_p = \mu_p q\, pT\, L \tag{4.10}$$

where $L = \frac{\pi^2}{3}\left(\frac{k_B}{q}\right)^2 = 2.44\,10^{-8} W\,\Omega K^{-2}$ is the Lorenz number, τ is the relaxation time of phonons, v_g is the group velocity of phonons and C the lattice heat capacity. In Eq. (4.8), P_n and P_p are the thermoelectric powers (or the Seebeck's coefficients) given by

$$P_n = \frac{k_B}{e}\left[\ln\left(\frac{n}{N_c}\right) - \frac{5}{2}\right] \tag{4.11}$$

$$P_p = \frac{k_B}{e}\left[\ln\left(\frac{n}{N_v}\right) - \frac{5}{2}\right] \tag{4.12}$$

After some algebraic manipulation the expression for the fluxes are

$$\begin{aligned}
J_i^n &= \mu_n n\left(\partial_{x_i}\varphi_n + P_n \partial_{x_i} T\right) \\
J_i^p &= -\mu_p p\left(\partial_{x_i}\varphi_p + P_p \partial_{x_i} T\right) \\
J_i^{un} &= -\kappa_n \partial_{x_i} T - e\, P_n T\, J_i^n \\
J_i^{up} &= -\kappa_n \partial_{x_i} T - e\, P_p T\, J_i^p \\
J_i^{uL} &= -\kappa_L \partial_{x_i} T
\end{aligned}$$

The continuity equations for the charge fluxes are

$$\partial_{x_i} J_i^n = q\, R \tag{4.13}$$

$$\partial_{x_i} J_i^p = -q\,R \tag{4.14}$$

where R is the total electron-hole recombination.

The temperature map is obtained by balancing the heat generated with the heat dissipation. The steady state formulation of the continuity equation for the energy flux, in absence of electromagnetic fields, reads as

$$\partial_{x_i}\left(J_i^{un} + J_i^{up} + J_i^{uL} - e\phi_n J_i^n + e\phi_p J_i^p\right) = 0 \tag{4.15}$$

From Eq. (4.15) we obtain the heat balance equation

$$\partial_{x_i}\left[\kappa_{tot}\partial_{x_i} T\right] = H \tag{4.16}$$

where $\kappa_{tot} = \kappa_L + \kappa_n + \kappa_p$ and H is the total heat source given by

$$H = e\partial_{x_i}[(\phi_n + T\,P_n)J_i^n + (\phi_p + T\,P_p)J_i^p] = H_J^n + H_J^p + H_{PT}^n + H_{PT}^p + H_{rec} \tag{4.17}$$

where

$$\begin{aligned}
H_J^n &= \frac{e j_i^n j_i^n}{n\mu_n} \\
H_J^p &= \frac{e j_i^p j_i^p}{p\mu_p} \\
H_{PT}^n &= -eT(j_i^n \partial_{x_i} P_n) \\
H_{PT}^p &= -eT(j_i^p \partial_{x_i} P_p) \\
H_{rec} &= R\left[\phi_p - \phi_n + T(P_n + P_p)\right]
\end{aligned}$$

The H_J^n is the electron Joule's heat and H_{PT}^n is the contribution due to Peltier and Thomson effects. The former is due to spatial variations in the carrier density or changes of the thermoelectric power at material interfaces, the latter is assigned to the change of thermoelectric power due to temperature variations. p-labeled quantities are related to holes. H_{rec} is the heat generated by the non-radiative electron-hole recombination. We finally note that the thermal conductivity of the carriers are usually some orders of magnitude lower with respect to the lattice thermal conductivity and can therefore be neglected [36].

4.3 Numerical technique

The aim of a numerical approach for solving a differential equation is to discretize the problem, which has infinitely many degrees of freedom, to produce a discrete problem which has finitely many degrees of freedom. Compared to the finite difference method, the Finite Element Method (FEM) is relatively recent. It was first introduced by Courant in 1943 and, afterwards, has been further developed and used by physicists and mathematicians.

The advantages of FEM is the capability to easly handle general boundary conditions and geometries. Furthermore, in many cases it's possible to get an explicite expression for

the error estimation. A short introduction to the FEM shall be given in the following (for a detailed introduction and analysis see e.g. [30, 37–39]). A rigorous treatment of the finite element method is bejond this work. Below is reported a briefly introduction. Let assume to have a differential equation $\mathcal{L}[u] = f$ where $\mathcal{L}[u]$ is a linear differential operator and f is a source term defined on the domain Ω.

Let us build the relative *weak* formulation

$$\int_\Omega \mathcal{L}[u_\beta]\varphi_\alpha dV = \int_\Omega f\,\varphi_\alpha dV \tag{4.18}$$

where $\varphi_\alpha \in U$ are the trial functions and U is some vector space called the *finite element space*. We now expande the solution as $u = c_\beta\varphi_\beta$ where $\varphi_\alpha \in U$ are the base functions. We have used the same space functions for both the trial and the base functions. This method is called the *Galerkin* method. Eq, (4.19) becomes

$$c_\beta \int_\Omega \mathcal{L}[u_\beta]\varphi_\alpha dV = \int_\Omega f\,\varphi_\alpha dV \tag{4.19}$$

The discretization of the problem means to consider a non infinite space function U. That way we are able to solve Eq. (4.19) by a simple matricial calculation $K_{\alpha\beta} = F_\alpha$ where K and F are the stiffness matrix and the load vector, respectively, defined as

$$K_{\alpha,\beta} = \int_\Omega \mathcal{L}[\varphi_\beta]\,\varphi_\alpha dV \tag{4.20}$$

$$F_\alpha = \int_\Omega f\,\varphi_\alpha dV \tag{4.21}$$

A fondamental ingredient that label a FEM is the triangulation of the domain. A triangulation $\mathcal{T}_h$ is defined on Ω, i.e. Ω is subdivided into a finite number of subsets $\mathcal{K} \in \mathcal{T}_h$.

The triangulation method as well as the finite element space must satisfy certain regularity properties. In particular the elements have to be non-overlapping and cover the whole region. Furthermore the space functions should have a support as small as possible in order to assures that the finite element basis has near orthogonal properties, i.e. two basis functions have only overlapping support when they are associated to neighboring nodes. Details about triangulations can be found in Ref. [35].

Under the above conditions the integrals over the domain Ω can be easily decomposed into a sum of integrals over the finite elements $\mathcal{K}_l$

$$K_{\alpha,\beta} = \sum_{K_l \in T_h} \int_{K_l} \mathcal{L}[\varphi_\beta]\,\varphi_\alpha dV \tag{4.22}$$

$$F_\alpha = \sum_{K_l \in T_h} \int_{K_l} f\,\varphi_\alpha dV \tag{4.23}$$

and the near-orthogonality assures that only a small number of basis functions (usually only the ones that are associated to a node of the element to integrate over) lead to non-vanishing integrals.

4.4 Discretization of the Fourier equation

Here we discretize the energy balance equation $\partial_{x_i}\kappa_{ij}\partial_{x_j} = H$.

The basis functions, denoted by $\psi_i(\boldsymbol{x})$, in this case are the piecewise linear functions

$$\left\{\psi_i \in H^1 \,\middle|\, \psi_i(\boldsymbol{x}_j) = \delta_{ij},\ \mathrm{supp}\{\psi_i\} = \bigcup_{\substack{j \\ x_i \in K_j}} \mathcal{K}_j \in \mathcal{T}_h\right\}, \tag{4.24}$$

i.e. they are continuous across the element boundaries and they are one at the node they are associated with and zero on any other node. These functions, also called *hat functions*, are illustrated in Fig. 4.2.

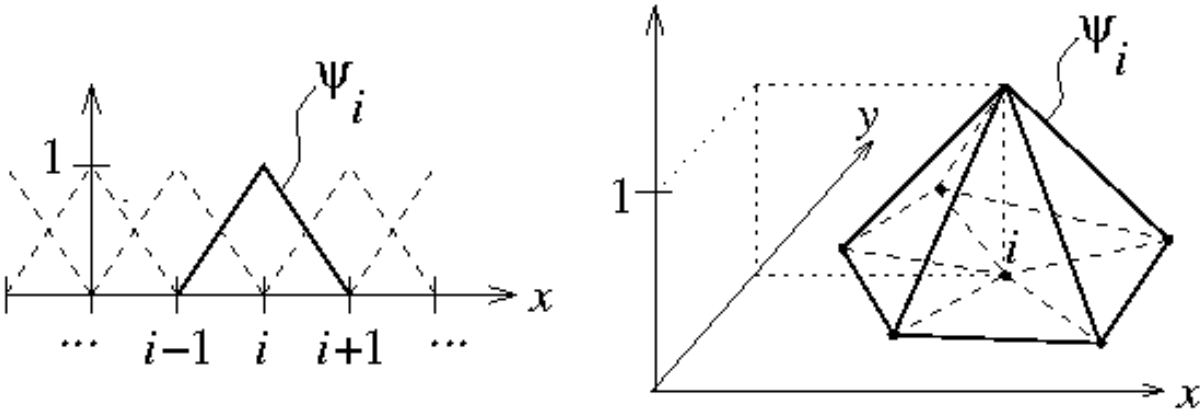

Figure 4.2: The basis functions of 1^{st}-order Lagrange elements in 1D and 2D (hat functions).

The differential operator of the Energy balance equation (4.16) is $\mathcal{L}[u] = \partial_{x_i}\kappa_{ij}\partial_{x_j}u$ whereas the source term is simply $f = H$. The temperature is expanded as

$$T(\mathbf{x}) = c_\beta \varphi_\beta(\mathbf{x}) \tag{4.25}$$

Referring to Eq.(4.20) the expressions for the stiffness matrix and the load vector are

$$K_{\alpha,\beta} = \int_{\partial\Omega} \varphi_\alpha(\kappa_{ij}\partial_{x_j}T)N_i dS - \int_{\Omega_\alpha} \kappa_{ij}\partial_{x_i}T\partial_{x_i}\varphi_\alpha dV \tag{4.26}$$

$$F_\alpha = \int_{\Omega_\alpha} H\varphi_\alpha dV \tag{4.27}$$

The first term in the left hand side is the thermal flux normal to the surface of the element. It can be used to impose Neumann boundary conditions, i.e.

$$-\int_{\partial\Omega_\alpha} \varphi_\alpha P_n dS - \int_{\Omega_\alpha} \kappa_{ij}\partial_{x_i}T\partial_{x_i}\varphi_\alpha dV = \int_{\Omega_\alpha} H\varphi_\alpha dV \tag{4.28}$$

where P_n is the imposed thermal flux, Thanks to the construction of the space functions defined in (4.24) we may obtain the temperature simply as

$$T(\mathbf{x_{fi}}) = C_\beta. \tag{4.29}$$

where $\mathbf{x_{fi}}$ is the coordinate associated to the node β.

4.5 1-D simulation

Here we provide an example of heat balancing in a 1D system. We consider a Si p-n diode of a length of $1\,mm$. The doping in both sides is $1\,10^{18}$. The ends of the diode are maintained at a environment temperature ($300\,K$). We first perform a sweep in the apply bias. Hereafter all results refer to a bias of $1.2V$. The band diagram is reported in Fig. (4.3). The device is long enough to allow the contact to reach the thermodynamical equilibrium in a natural way. Otherwise, the electric boundary conditions would force the equilibrium, indirectly imposing an infinite electron-hole surface recombination.

The heat sources are reported in Fig. 4.4. As one can see, most of heat is produced in the depletion region where the recombination take place. The Joule's effect is higher in the p-region (left-side) due to the lower mobility of holes. The temperature profile reach the maximum value at the center (see Fig. 4.5) and matches the Dirichlet boundary conditions at the ends of the diode. The whole calculation is validated by the power balance check (Fig. 4.6).

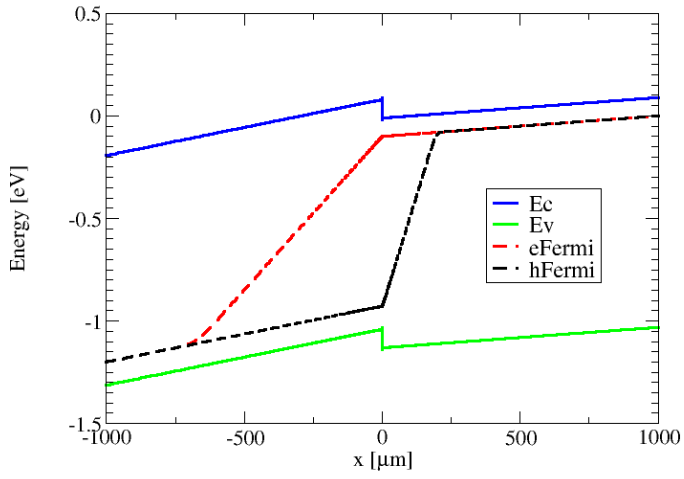

Figure 4.3: Band diagram

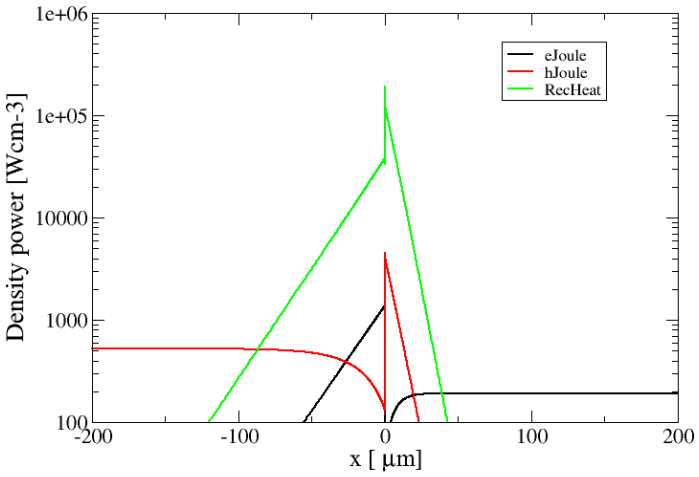

Figure 4.4: Heat sources

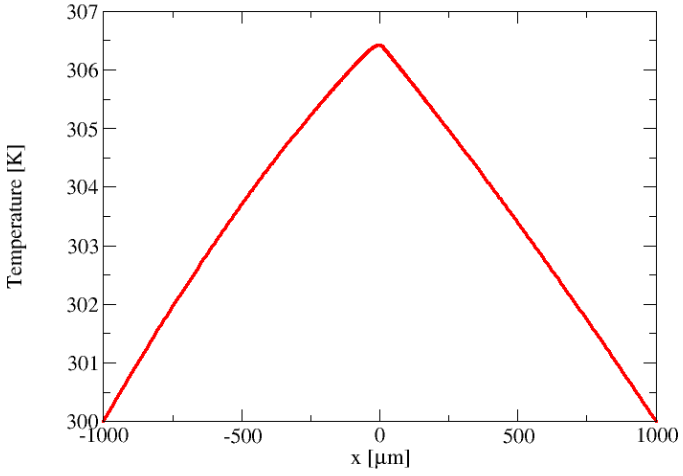

Figure 4.5: Temperature profile

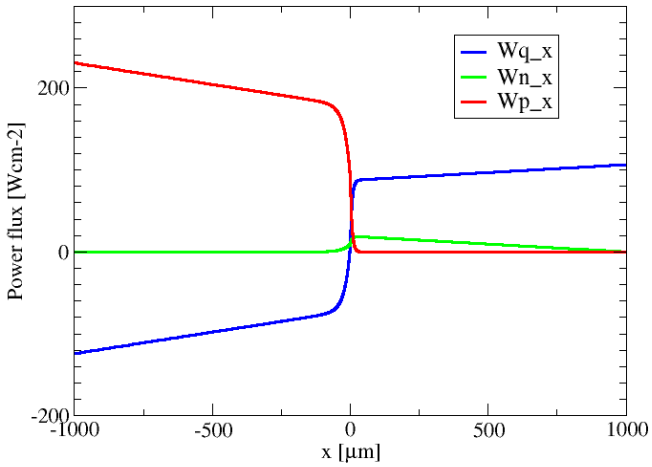

Figure 4.6: Power balance

Chapter 5

TiberCAD

5.1 The mission

TiberCAD is the leading software of TiberLAB s.r.l. [40], the university spin-off involved in the development of TCADs. The aim of TiberCADis to couple different physical models, both atomistic and continuous, in the same simulation. The software is fully modular and each module performs a task (see Fig.5.4). The first release of TiberCADcounts four modules: the DriftDiffusion, ThermalBalance, Elasticity and EFA modules. A typical simulation flow chart is as follows: first the Elasticity module calculates the internal stress due to either lattice mismatch or external forces. Then, EFA module computes the band diagram according to the strain map. The DriftDiffusion module calculates holes and electrons transport taking into account the piezoelectric potential as well as the strain induced band bending. EFA and drift-diffusion simulation can be coupled self-consistently in order to get the electrostatic potential due to the quantum charge. Once the transport of charge carrier is computed, the heat generated is taken as input by the ThermalBalance module which computes the temperature profile by balancing the heat generated and the heat dissipated. This work is clearly focused on the latter module.

Several modules are under development and will be mainly devoted to the atomistic models such as empirical and semi-empirical Tight Binding models. These modules, including also the Non-Equilibrium Green's function formalism, allow to compute the tunneling current wich can be taken as boundary condition for the continuous transport simulation. A review on physical models of TiberCAD can be found in [41].

5.2 The multiscale approach

The multiscale schemes can be grouped in two categories: the *bridge* and the *overlap* method. The bridge method, used in this work, is employed when models communicate with each other via their boundary conditions (see Fig. 5.3(a)). In this case there is no overlap among domains which are bounded exclusively through their contacts. This method has been used in the computation of the gate tunneling current in high-k MOSFETs. The leakage current

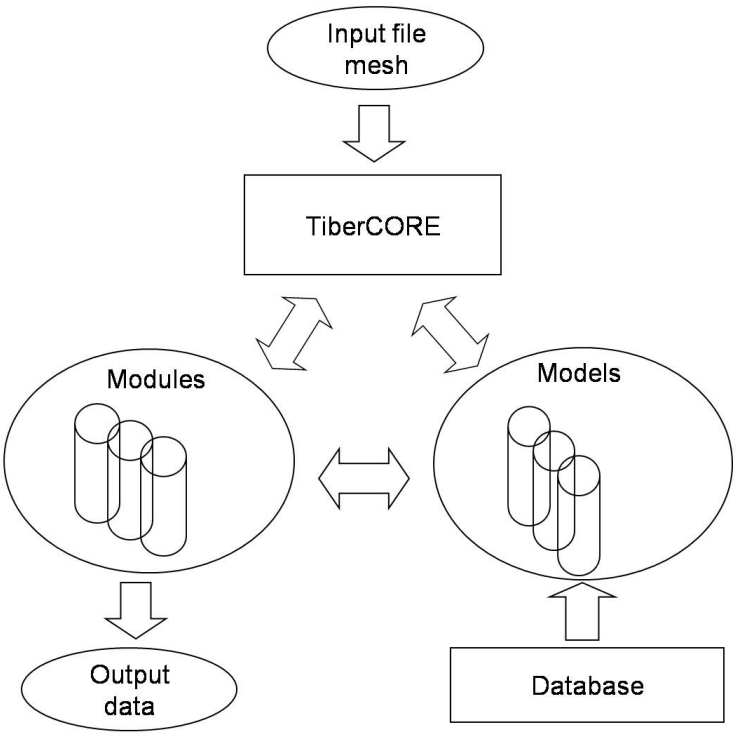

Figure 5.1: TiberCAD scheme

along the oxide is computed by the empirical tight binding method and rest of the device is treated at the drift-diffusion level. The tunneling current acts as boundary condition for the transverse transport of electrons in the channel. Details of this simulation can be found in [42].

The overlap multiscale method is used whenever a model uses physical properties whose value is computed by an another model (see Fig. 5.3(b)). The domains are, therefore, overlapped. This is the case when, for instance, the quantum charge in a quantum dot is used by the drift-diffusion simulation to compute the electrical current. An example of this simulation can be found in [43]. The aim of the ThermalBalance module is to handle the heating and the heat dissipation as two separate problems. For a given module, TiberCAD allows to define physical models over a restricted area. That way allows to handle heating and dissipation in a very flexible manner. For example it is possible to define a constant heat source in a small part of the simulation domain and include the heat generated by electron and hole transport in another region. In the same way it is easy to associate each part of the device with different heat transport models (see Fig. 5.4).

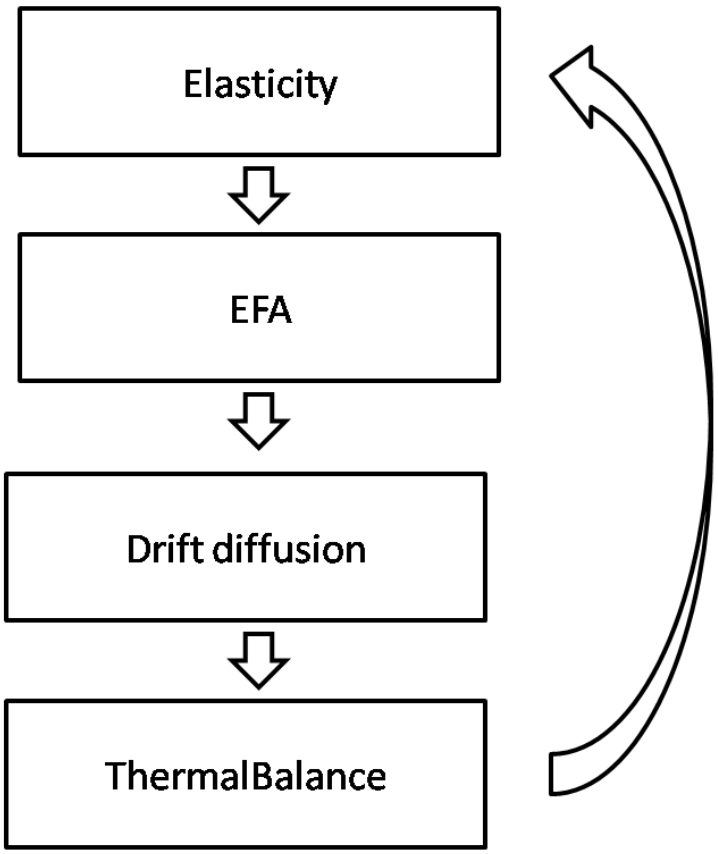

Figure 5.2: TIBERCAD modules

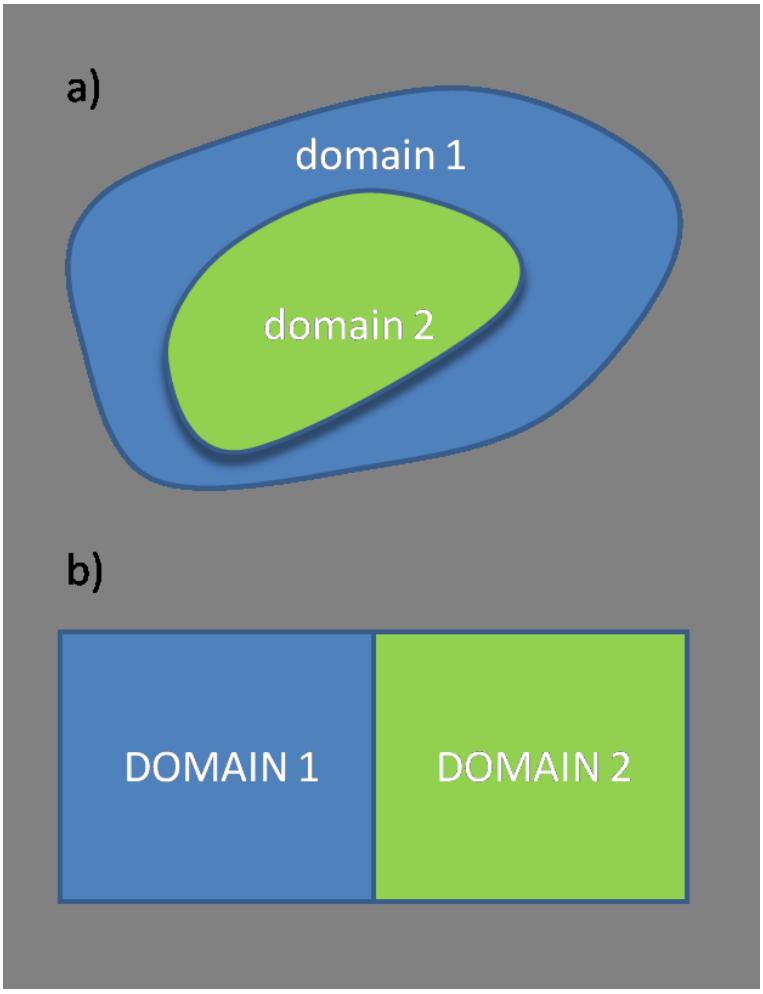

Figure 5.3: a) Bridge and b)Overlap multiscale schemes.

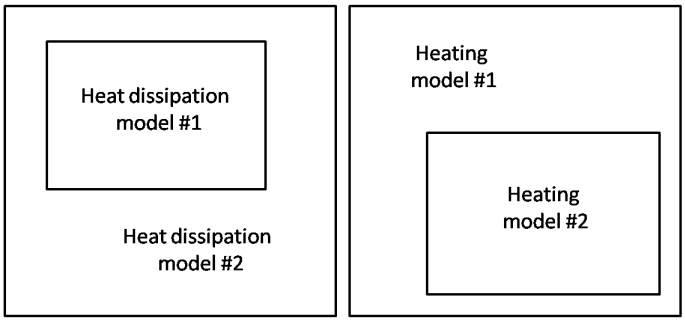

Figure 5.4: Heat dissipation and heating model partition

Chapter 6

Applications

This chapter contains two parts. In the first part we report on calculation of heating and dissipation of molecular systems. We mainly expose the results published in Ref. [2,4,44,45]. In the second part we report the results about a multiscale computation for a pyramidal GaN quantum dot embedded in a AlGaN nanocolumn. The results are pretty similar to those for the cubic quantum dot in the same system [32].

6.1 Styrene molecule

We consider the system shown in Fig. 6.1, comprising a Si(100) substrate, reconstructed 2x1, with an adsorbed styrene molecule in a bridge position and an Ag metal contact which could model an STM tip. The position of the tip was chosen in order to obtain a relatively large direct coupling between the tip and the π orbitals of the styrene which guarantees a sufficiently high conductance. The Figure shows a unit cell of the system considered, but periodic boundary conditions are imposed. The Si substrate is heavily p-doped in order to make it conducting and the Fermi Level is assumed at the valence band edge. While electrons cross the molecule, they interact with the molecular ionic vibrations from which they can be inelastically scattered. The electron-phonon scattering within the leads is not considered in this work.

In order to study the electron-vibron coupling we first relax very accurately the structure (This is done under no applied bias). Then we compute the vibrations of the molecule constraining the Si and Ag atoms. The calculation is then repeated letting all atoms free to move. This calculation allows to compute the coupling of the molecular modes with the Si substrate and to compute the decay rate of such vibrations into the contacts.

This type of first-principle calculation applied to phonon decay is presented here for the first time to our knowledge. The result of such calculation is shown in Figure 6.2, reporting in the upper panel the superposition of the phonon density of states of the coupled system with the uncoupled molecular frequencies shown as vertical dashed lines. The phonon DOS of the Si substrate is shown as a gray area where the cut-off frequency of 500 cm^{-1} is clearly visible. The modes within the Si bandwidth show a sizeable broadening due to the interaction with

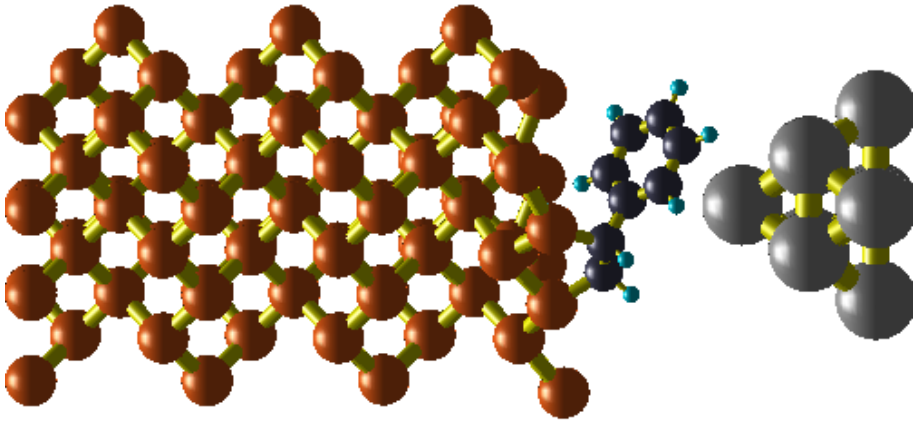

Figure 6.1: Cartoon showing a unit cell of the system with a styrene molecule adsorbed on a Si(100) 2x1. Periodic boundary conditions are imposed on the structure

the contacts. As the frequency rises above the cut-off both broadening and frequency shift become very small. The lower panel of Fig. 6.2 reports the decay rates, J_q, computed from the broadening of each molecular mode. The model gives realistic results for those molecular modes lying within the Si phonon bands, however they decrease fast as the molecular frequencies go beyond this band.

On the light of the discussion made in section 2.4, decay rates as slow as 10^2 Hz are rather unrealistic, therefore the lowest limit of decay of 10^6 Hz has been fixed in subsequent calculations.

We find that the out of equilibrium phonon population is strongly bias dependent. At the applied bias of 0.95 V, a molecular resonance (shown in Figure 6.5) enters the injection window, with the effect of strongly increasing the coherent and incoherent currents. On average all vibrational modes are excited as the bias increases, although some of them are particularly favored, such as the lowest vibrational mode. This depends on the electron-phonon couplings shown in Figure 6.3. First we project the electron-phonon coupling matrices, M_q, on the molecular orbitals, ψ_i Since the tunneling process occurs via the MO resonances, these matrix elements give an indication about which modes have larger el-ph interactions. We observe that the lowest mode dominates over most molecular orbitals, and gives the largest average coupling. The lowest vibrational mode, at the frequency of 10.55 cm^{-1}, corresponds to a rigid oscillation of the whole benzene ring, away and toward the Ag tip, leading to a strong variation of the molecule-metal matrix elements and, therefore, to a large electron-phonon coupling. This explains why the phonon emission mostly occurs into the lowest energy mode, once the first resonant tunneling is hit. Fig. 6.4 reports the behavior of the molecular temperature as a function of applied bias for two different contact temperatures.

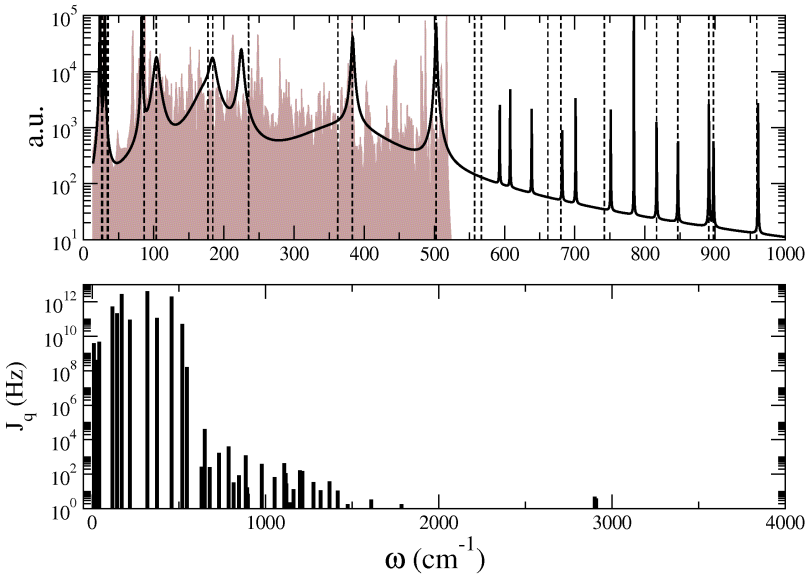

Figure 6.2: Upper. Phonon DOS of the coupled system Si-substrate + molecule and uncoupled molecular modes (vertical lines). Lower. Phonon decay rates.

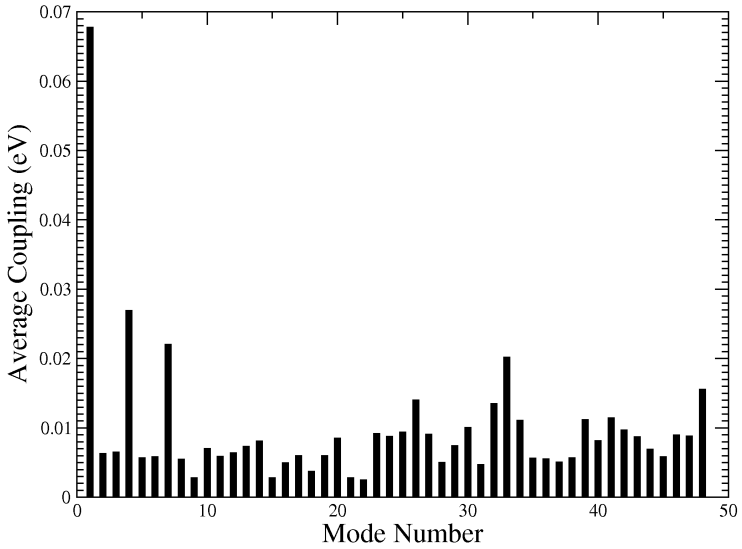

Figure 6.3: Average electron-phonon coupling for each mode.

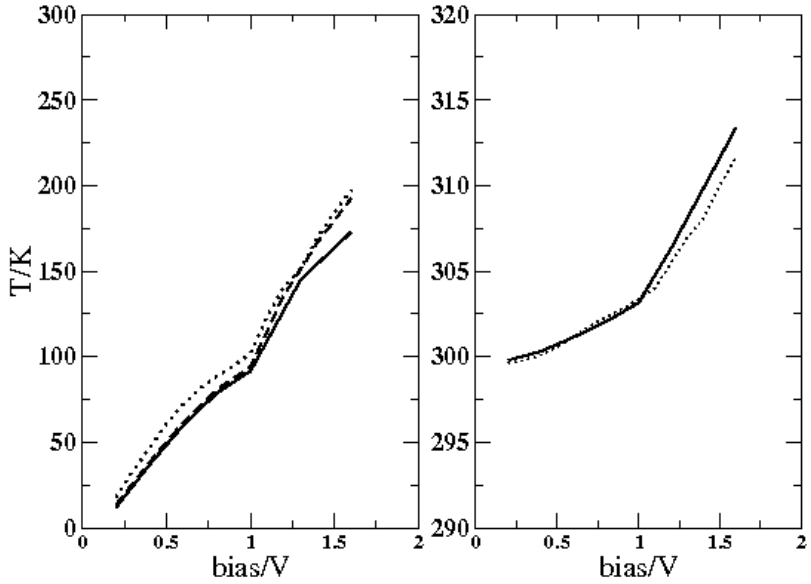

Figure 6.4: Molecular temperature as a function of bias for different contact temperatures. Left, T_0=0. Right T_0=300 K. Dotted, dashed and solid lines correspond respectively to lowest order, BA and SCBA.

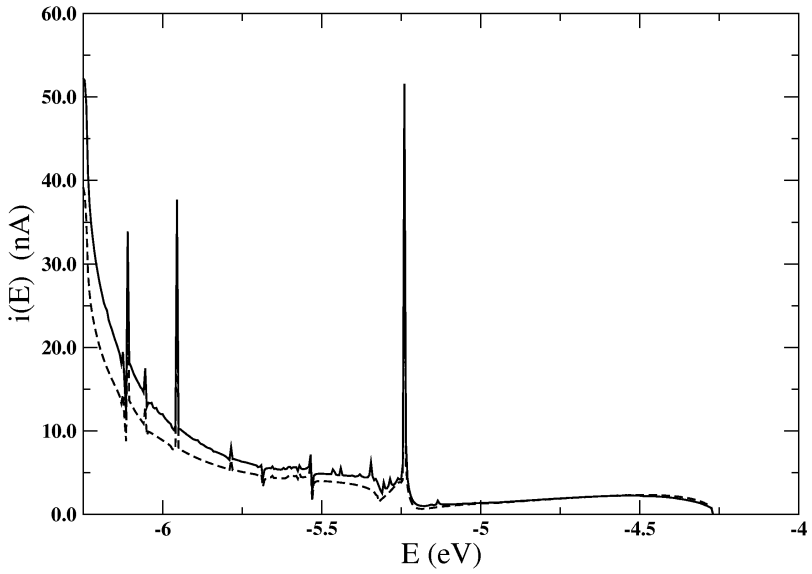

Figure 6.5: Total and coherent component of the current density in the energy window relevant for integration.

It is possible to appreciate the change in slope at the applied bias of 1.0 V. The figure reports three different calculations obtained for the simplest lowest order calculation, not including the electron-phonon self-energy renormalization of the electron propagator, the first order correction, commonly known as first order Born approximation (BA) and the self-consistent Born approximation (SCBA). Because of the small incoherent tunneling current, the inclusion of higher orders bring only small corrections to the final result. The computed current density within the bias window at 2.0 V is shown in Figure 6.5, where it is possible to see the resonance peak at -5.25 eV. The figure shows the total current and the coherent component. The incoherent component (not shown) is about two orders of magnitude smaller, except at the resonance, where it becomes comparable. The total tunneling current computed at 1.0 V is 1.2 nA.

The molecular temperature sensibly depends on the tunneling current, which can be changed by varying the tip-molecule distance. When this distance becomes approximately 2.0 the flowing current reaches 0.5 μA, leading to a very large temperature increase ($\approx$ 1000 K). Obviously the molecule is not likely to withstand such temperatures and may rather desorb.

6.2 $C_{10}H_{12}$ and $C_{10}H_{10}$ molecules

The method has been applied to two systems (see Fig. 6.6) obtained by a sandwich of an organic layer between two Si contacts. The contacts of both structures are identical and made of hydrogenated Si(100), 2x1 reconstructed. The molecules are adsorbed on the surface via Si-C covalent bonds. For the first system the molecule chosen is a $C_{10}H_{12}$ (structure A), whereas $C_{10}H_{10}$ is used in the second structure (structure B). Periodic boundary conditions are imposed on the structures shown. The total energy of the contact-molecule-contact system is

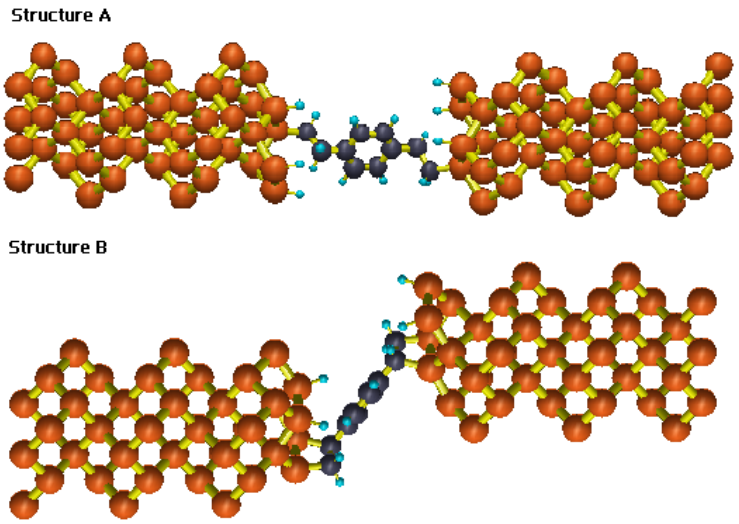

Figure 6.6: Test structures comprising two semi-infinite contacts of hydrogenated Si(100), reconstructed 2x1 and an absorbed molecule in configuration A ($C_{10}H_{12}$) and in B is ($C_{10}H_{10}$)

obtained through a local basis density functional scheme, where appropriate approximations are considered in order to make the approach efficient for a large number of atoms [46]. These include the use of an optimized minimal basis set and the neglect of three-center integrals. Both the electronic and the repulsive potential, are expressed as a superposition of atomic pair-potentials, obtained from ab-initio DFT reference calculations allowing extensive use of look-up tables. The method is very successful in describing structural properties of materials and their also gives accurate results for the mode frequencies.

We have seen how contacts induce a perturbation on the molecular modes and vibrational frequencies. Additionally, we have obtained two approaches for the evaluation of the projected DOS. The first method gives the exact DOS as obtained from the exact Green's function of the open system defined in equation (2.40). In the second method the self-energies are approximated by an energy independent shift and broadening, leading to the form of equation (2.47). Since for $\Pi^r(\omega^2) \to 0$ the $\tilde{\rho}(\omega) \to \rho(\omega)$, for frequencies beyond the silicon bandwidth both method give the same result. Figure 6.7 shows the comparison between the exact and the approximated DOS up to the Si cutoff (500 cm^{-1}). Obviously the simple

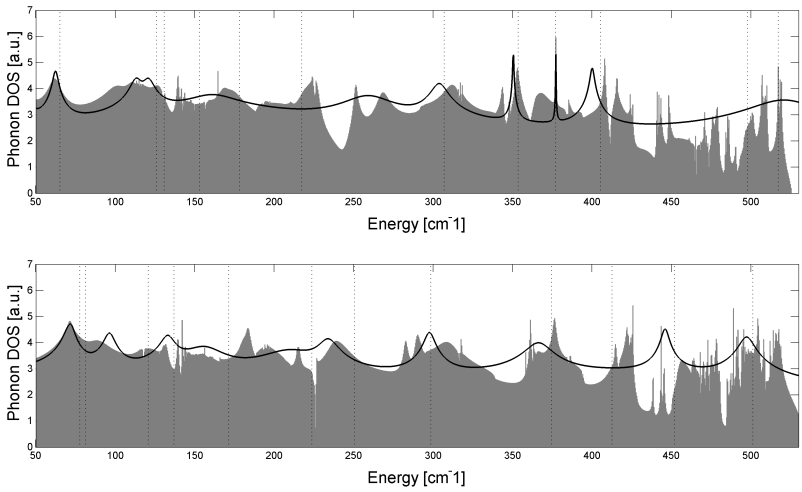

Figure 6.7: Phonon DOS projected on the molecule. The dashed lines correspond to the unperturbed molecular frequencies. The solid line is the lowest order approximated DOS and the grey shaded area represents the exact DOS.

$shift + bradening$ approximation sometimes is too crude and does not capture the richenss of the exact result. However, it gives a first order approximation to the complex problem of defining the vibrational lifetimes.

The phonon decay rates, J_q, of both structures are computed using Eq. (2.45) and shown in Fig. 6.8. Qualitatively similar results are obtained, which strongly depend on the contact DOS. Indeed, J_q is fast for the energy modes lying within the contact phonon bandwidth and sharply decreases beyond, reaching very small values.
These decays are underestimated, as discussed in the previous section, because do not include anharmonic corrections, that generate to one-to-many phonons decay channels.

The left and right contacts are identical and therefore the phonon bandwidths are the same. The projected phonon DOS on the contact surface is shown in Fig. 6.9. This is obtained from the surface Green's function of equation (2.38). The frequency cutoff (ω_D) is about 500 cm^{-1}, appropriate for bulk Si. The peaks around 580 cm^{-1} and 2000 cm^{-1} are related to the hydrogen passivation of the silicon surface.

Despite the difference in nature of the Si-C bonds between the two systems considered (one bond for structure A and two bonds for structure B), there are no lare differences in the decay rates. Due to the larger number of bonds to the surface, structure B is more rigid and posses higher mode frequencies. For this reason the elastic coupling to the surface is slightly more effective with respect to structure A, as seen in Figure 6.8.

The localization of the modes is another important parameter that governs the decay rates on the two contacts. In general, even when the contacts are identical and the bonds of the molecule to the surfaces are the same (as in our case) the decay rate of the molecular vibrons in the two leads can differ significantly. Indeed, the decay rates depend on the localization

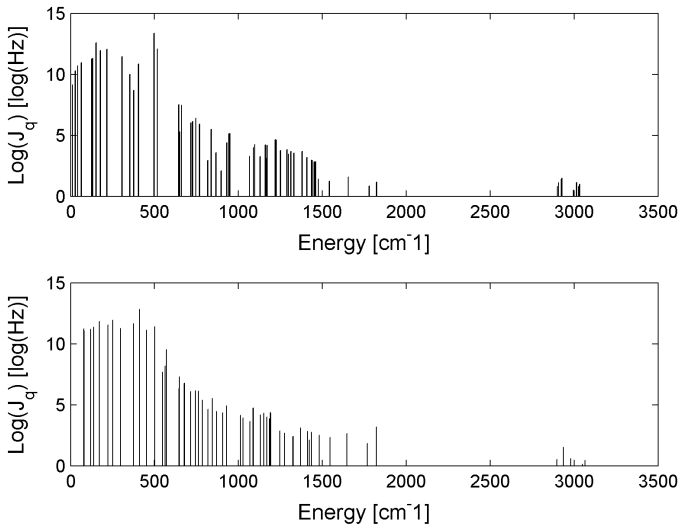

Figure 6.8: Decay rates of molecular vibrons into contact phonons

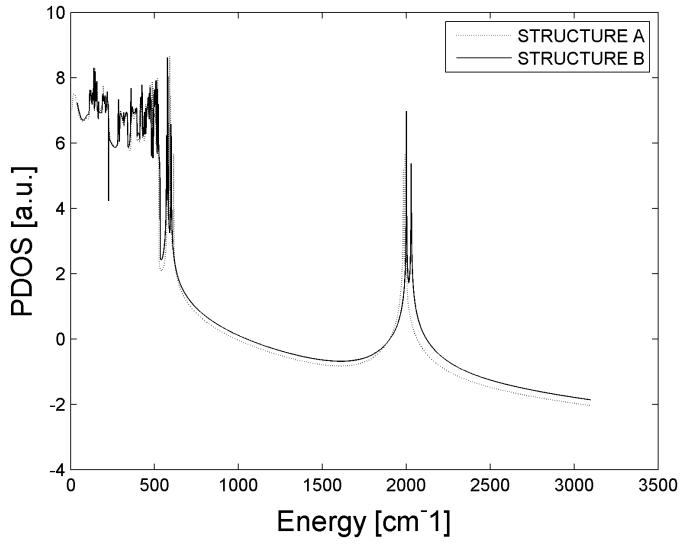

Figure 6.9: Phonon DOS of the contacts

of the vibrational modes. For instance, consider the vibrational mode of structure A at $\omega_q \cong 2900\ cm^{-1}$. This is mainly localized on one side of the molecule, as shown in Fig. 6.10(a). As a consequence, the decay rate into the right contact is much higher than the decay rate into the left contact ($J_q^R >> J_q^L$). In the opposite case, the mode at $\omega_q \cong 2907\ cm^{-1}$ has a much higher decay rate on the right contact, near which it is localized (see Fig. 6.10(b)). Eventually, symmatric modes as for instance that at $\omega_q \cong 1300\ cm^{-1}$ have an equal decay rate in the two contacts ($J_q^R \cong J_q^L$) (see Fig. 6.10(c)). The systems analyzed in this paper posses almost

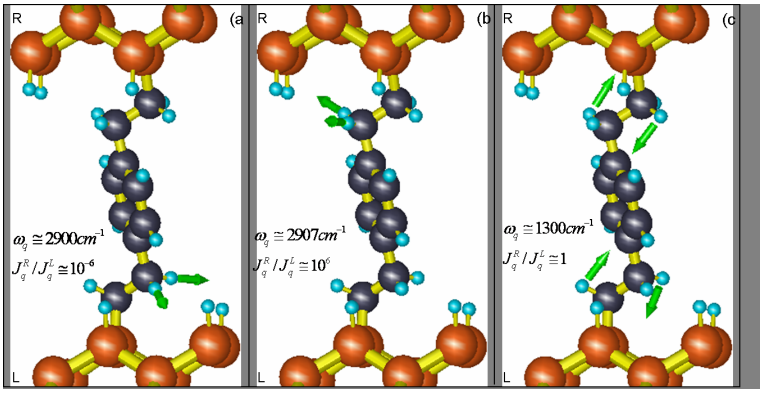

Figure 6.10: Mode localized near a) the left contact, b) the right contact and c) symmetric on both contacts.

perfect inversion symmetry, therefore, for each mode localized near one contact there is an almost degenerate mode localized near the other contact (degeneracy may be left because of a small symmetry breaking due to the numerical geometry optimization). As a consequence the heat release into the two contacts is the same. However, we can envisage that suitably constructed asymmetric molecules may give strongly asymmetric decays, leading to voltage-induced temperature gradients (Peltier effect) or heat rectifiers.

In the following we show the impact of the decay rates, J_q, on the molecular temperature. Figure 6.11 shows the coherent tunneling for both structures, where it is possible to see that Structure B is much better conducting than Structure A. The reason of this pronounced difference is that in structure A the short chains of C_2H_2 represent insulating bridges which are absent in structure B. The difference in coherent tunneling is also reflected in a difference of incoherent tunneling and local heating between the two systems.

The steady-state temperature reached by the two structures under bias conditions is reported in Figure 6.12 as a function of voltage. In this calculation the contact reservoirs are assumed to be at an equilibrium temperature of T=0 K.

Structure B heats up much more than structure A. Furthermore, for structure B we find a bias interval in which no stable steady state solutions are possible (within the approximations used). In this bias window the molecule heats up considerably and it is not likely to be stable. This phenomenon happens when the number of phonons emitted overcomes the number of phonons dissipated into the contacts. From a mathematical point of view, the absence of a steady state solution is indicated when negative values of some N_q are obtained.

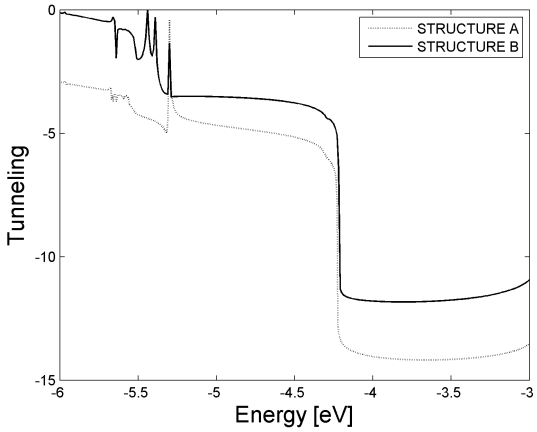

Figure 6.11: Tunneling

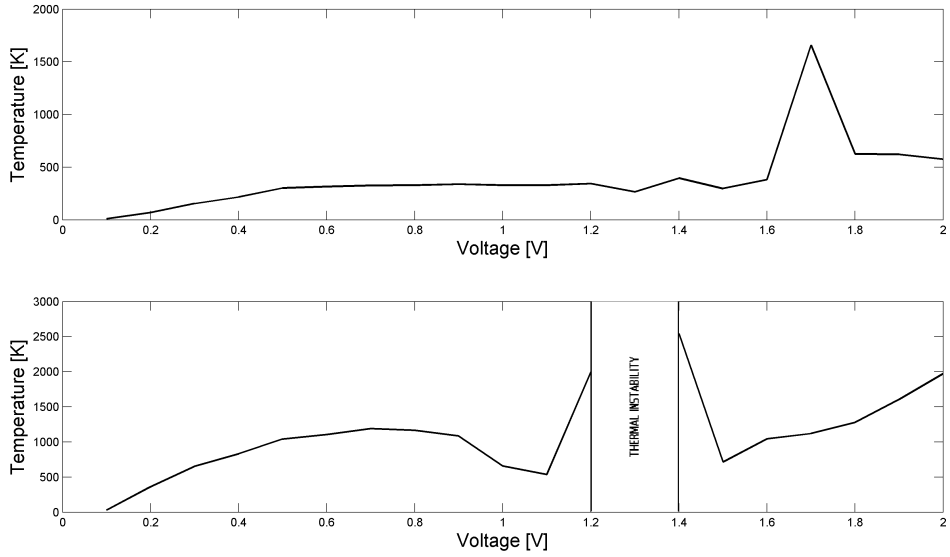

Figure 6.12: Local temperature reached by the molecules under bias. In structure B we find a bias interval where no steady state solutions are found.

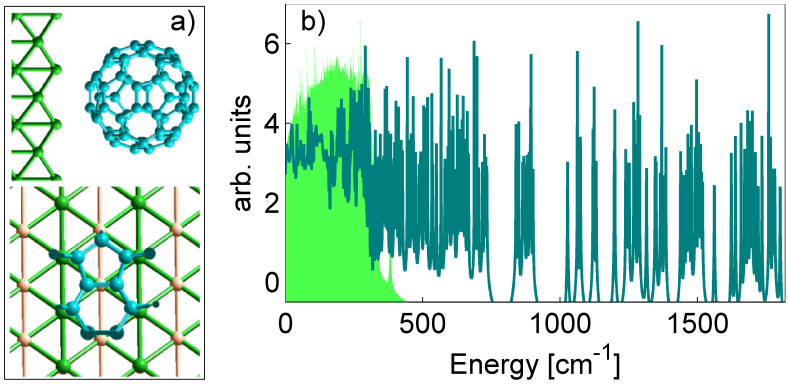

Figure 6.13: (color online) (a) C_{60} fullerene molecule on Cu(110) surface. (b) The phonon DOS of the perturbed molecule. The phonon DOS of the contact is shown in the background.

6.3 Fullerene molecule

In this we apply the formalism describe in second chapter to understand and discuss heating and thermal stability of a C_{60} molecule sitting on a Cu(110) substrate in which a Cu STM tip is used to drive a current through the junction [45]. The STM tip is modeled as a pyramid of Cu atoms and is positioned at varying distances (D_{tip}) from the closest C atom of the fullerene. The details of the the C_{60}/Cu interface geometry, shown in Fig. 6.13a, can also be found in [45]. The vibron decay rates, J_q are computed

The resulting dynamical matrix for this system, computed as Eq. (2.34) is partitioned into contact and device regions and the decimation algorithm is applied to compute the self-energy and the local density of states projected on the molecule. The latter is shown in Fig. 6.13b. The same figure also shows the phonon spectrum of the Cu substrate as a shaded area, in which the Debye cut-off frequency at about 300 cm^{-1} is quite evident. The values of J_q, extracted from the peak broadenings, range between 10^{10} Hz and 10^{12} Hz for the low energy modes, found within the Cu phonon bandwidth, and progressively decrease to as low as 10^3 Hz for the highest frequency modes ($\cong$ 1800 cm^{-1}). These low decay rates are probably strongly underestimated as anharmonic coupling and one-to-many phonon decays may give a considerable contribution. However, to avoid to introduce artificial parameters, in this work we neglect such effects.Furthermore, we will show in the following discussions that already at moderate voltages the emission/absorption rates, E_q and A_q, can be quite large for the high frequency modes, such that we expect $E_q >> J_q$ and $A_q >> J_q$ even after higher order corrections are taken into account. As a consequence, J_q should not play a significant role for these modes. We assume that there is no difference of temperature between the two contacts, namely, $T_L = T_R = T_0 = 0\ K$ which is close to STM experiments carried at $T = 4.2\ K$. In this case the contributions E_q^{LL}, E_q^{RR} and E_q^{RL} vanish because of

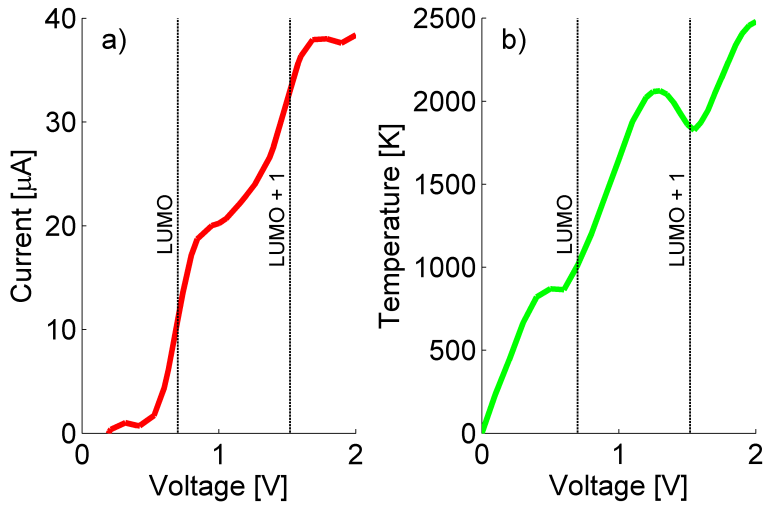

Figure 6.14: (color online)The dashed line is the electronic DOS.(a) Total current vs bias. As expected, the resonance makes the current rises (b) Molecular temperature vs bias. The lowering of the temperature across the resonance is due on the interplay between the emission and absorption processes

the Heaviside functions, whereas A_q^{RL} is non-zero only for $eV < \hbar\omega_q$. The terms E_q^{LR} and A_q^{LR} correspond to tunneling between the two contacts with corresponding emission and absorption of phonons. The terms A_q^{LL} and A_q^{RR} correspond to electron reflections after absorption of a phonon and we will refer to them as A_q^{tip} and A_q^{sub}, respectively, assuming the substrate to the right ant the tip to the left. These terms correspond to phonon decays via electron-hole (*e-h*) excitations in the contacts. We now assume that a bias, V, is applied to the substrate, while the STM tip is grounded, i.e. $\mu_R = \mu_L - eV$. Under these conditions the unoccupied levels are probed for positive voltages. We further assume that the molecular levels are pinned with the substrate Fermi energy and the whole applied bias drops at the molecule/tip interface. This is an extreme assumption, but it is supported by independent self-consistent DFT/NEGF calculations. The voltage ranges from 0.0 to 2.0 V. As shown in Fig. 6.14a the current steeply rises whenever a resonance enters in the injection window. The molecular resonances, centered at energy $E_1 = 0.7\ eV$ and $E_2 = 1.5\ eV$, will be referred as LUMO and LUMO+1, respectively. Correspondingly, Fig. 6.14b shows that the temperature rises because resonant phonon emission takes over. In the same Figure it is possible to observe that just before reaching a resonance, the molecular temperature can even decrease. The effect is especially visible for the LUMO+1. In the case of metal contacts this can be understood by considering Eqs. (2.48) and (2.49), with the help of Fig. 6.15. The LUMO level entering the bias window has energy E_L and we consider, for simplicity, just one effective vibrational mode of energy $\hbar\omega < E_L$. The equilibrium Fermi energy is assumed at $E_F = 0$. For increasing voltages up to $eV < E_L - \hbar\omega$ the molecular temperature increases since the emission rate prevail. As the molecular level approaches, for a bias in the range $E_L - \hbar\omega < eV < E_L + \hbar\omega$,

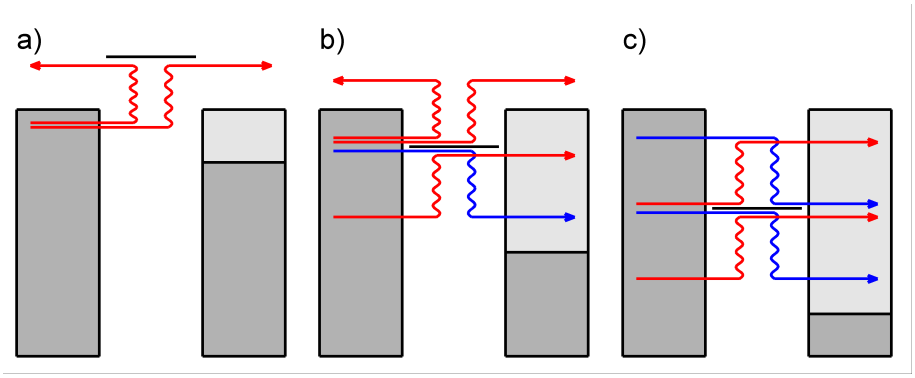

Figure 6.15: (color online) (a) For $0 < eV < E_L - \hbar\omega$ there is one resonant absorption process via *e-h* pairs in the substrate and one absorption process via transmission. (b) For $E_L - \hbar\omega < eV < E_L + \hbar\omega$ there are three resonant absorption processes (one into *e-h* pairs) and one resonant emission process. (c) For $eV > E_L + \hbar\omega$ there are two absorption and two emission processes via transmission.

resonant absorption channels activate and can prevail over the emission, leading to a decrease of temperature. For $eV > E_L + \hbar\omega$ two resonant emission processes become possible and the term E^{LR} rises, whereas A^{tip} become no longer active because no states are available for the reflected electrons. In this regime emission prevails over absorption and the molecule heats up, resulting in the usual increase of temperature with applied bias. A further analysis shows that in the intermediate cooling regime the high energy modes play a major role. The first reason for this is that, thanks to their high energy, these excited modes contribute considerably to the total vibrational energy of the molecule, which is therefore more sensitive to a decrease of their population, N_q. The second reason is because, for energies higher than the Debye frequency, the phonon-phonon decay rates becomes very small (see Fig. 6.13b) and the vibron population becomes more sensitive to the absorption and emission processes, depending only on the ratio A_q/E_q ($J_q \approx 0$). The last reason is simply because for larger $\hbar\omega_q$ the energy range in which absorption overcomes emission is wider, leading to a more visible effect in terms of applied bias. Our calculations also show that the population of the high energy modes decrease, whereas the population of the low energy modes keep increasing with increasing bias. By observing Fig. 2, it should also be observed that when $T_0 = 0$ there are no excited quanta to absorb when the LUMO resonance approaches the bias window (as in Fig 3a), resulting in a barely visible decrease of temperature. On the other hand, when the second molecular level (e.g., LUMO+1) approaches the bias window, resonant absorption give rise to a much more evident cooling effect, since phonons are removed from an already excited vibronic population. A qualitatively similar effect was also computed in Ref [47] using a model Hamiltonian.

We observe that in the cooling regime the power dissipated, as given by equation (2.7), keep increasing since it is dominated by the values of J_q corresponding to the low frequency modes, which heat up monotonically. In this regime internal energy and power dissipated

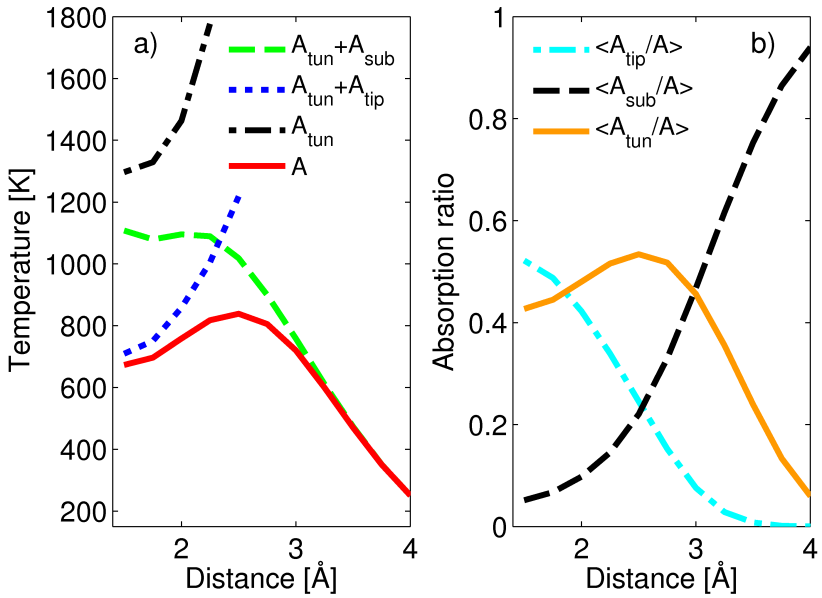

Figure 6.16: (color online) (a) Temperature vs tip distance. The red line shows the temperature trend taking into account all absorption processes. The blue line and the green line neglects e-h formation into the substrate and the tip, respectively. The black line corresponds to absorption via tunneling only. (b) Different relative contributions to the total absorption rate via *e-h* in the tip, the substrate and via tunneling.

via phonon-phonon decays have opposite trends.

Phonon decays via *e-h* excitations in the metal contacts provide a crucial cooling mechanism. Indeed, thanks to this decay channel, the molecule can remain stable even at relatively large voltages. To better emphasize this issue, we sweep the distance between tip and molecule keeping the voltage fixed. Fig. 6.16 shows the results for a bias of 0.4 V. This voltage is small, but larger than the higher vibrational energy of the molecule. Consequently we can expect that all modes are excited by electron-phonon scattering. As long as the tip is far from the molecule (tunneling region) the current is low and only A_q^{sub} plays a relevant role. The crucial point here is to note that in the absence of *e-h* excitations in the substrate the molecule will easily brake. Indeed, when A_q^{sub} is removed from Eq. (2.29), we find that N_q has no longer physical solutions for $D_{tip} \geq 2.8$ Å. In practice N_q diverges and we understand this results as a thermal instability of the molecule. Furthermore, if we remove both the substrate and the tip contributions and keep only the tunneling absorption mechanisms, the molecular temperature would be much higher (black line).

As shown in Fig. 6.16 the stability of C_{60} on the metal substrate is guaranteed by the *e-h* decays. Reducing the tip-molecule distance, the term A_{tip} becomes large and we observe two competing effects. On the one hand, as the tip approaches the molecule, the current increases, leading to an increase of heating; on the other hand the tip increases absorption via

e-h excitations, keeping the molecule cool. These competing effects produce the maximum at $D_{tip} = 2.8$ Å shown in Fig. 6.16a.

Fig. 6.16b shows the relative magnitude of the absorption processes as a function of tip distance. As expected, when the tip is close both tip and substrate contribute equally, whereas when the tip is far *e-h* pairs can be excited in the substrate only.

The role of dissipation via phonon-phonon decays is only marginal in this system and only effective for low energy modes. Although our lowest order treatment of the one phonon-to-one phonon decay processes may considerably underestimate the decay rates J_q, this can hardly reach the absorption rates necessary to keep the molecule stable, provided by A_q. The average of the A_q^{sub} is 10^{10} Hz and the average of A_q^{tip} range from 10^{11} Hz when the tip is at 2.0 Å to 10^7 Hz when the tip is at 4 Å. The values of J_q are several orders of magnitude smaller.

A natural question that may arise is whether it is possible to cool a molecule below the environment temperature. An inspection to Eq. (2.31) leads to the conclusion that cooling effect below T_0 may occur for $A_q > E_q e^{\hbar\omega_q/k_b T_0}$. In fact, in this case we have $R_q < 0$, $N_q < n_q(T_0)$ and part of the energy given by the applied bias is used to cool the molecule, like in a Peltier cell. Unfortunately this condition is not easily obtained for a normal molecule with large vibrational energies, $\hbar\omega_q >> kT$, with the consequence that the molecular temperature is always greater than the environment temperature. The molecule can effectively cool to lower temperatures only when it possesses vibrational modes of low energy, $\hbar\omega_q < kT$. For instance in the case of $T = 300K$ it is sufficient to have $\hbar\omega_q \approx kT/2$ and $A_q \approx 2E_q$ to obtain a phonon population lower than in equilibrium. Fundamental is also the role played by the resonant energy levels of such a molecule, which in equilibrium should be positioned at $E_L > E_F + \hbar\omega_q$ in order to activate the resonant absorption channel before the resonant emission. These conditions could be met for instance by a system of heavy ions (like a CdTe nanoparticle) placed in between Au contacts.

6.4 2D p-n Silicon junction

Here we will see a simple electro-thermal simulation of a 2D p-n Silicon LED. The diode is a vertical structure (see Fig.6.17). Along the interface with the substrate we impose a thermal surface resistance $R_s = 0.5\,K\,cm^2\,W^{-1}$. The device is surrounded by the air whose The heat conduction through the environment is modeled by adding an air region all around the diode. The boundary of the air region are fixed to $T = 300\,K$. Furthermore, we rely on the cylindrical symmetry with respect to the growth axis and consider only a 2D slice of the system. In this way we simulate a 3D device by performing a 2D simulation (with much less computational time). We compute the electric current by means of a drift-diffusion model, performed for a range of applied bias. Then, the thermal map is computed by the Fourier model at a bias of $1.2\,V$. The results are given back to he drift-diffusion simulation where all quantities depending on temperature are changed accordingly. The drift-diffusion/Fourier loop is performed self-consistently. In Fig. 6.18 the heat sources are reported. Clearly, the Joule's effect of electrons and holes is localized mainly in the p-region and n-region, respec-

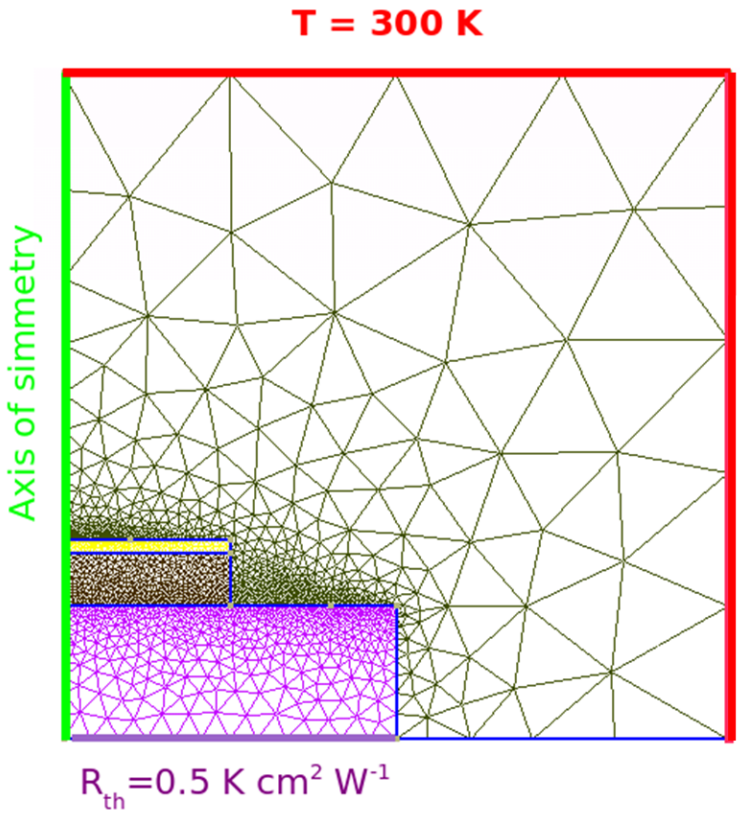

Figure 6.17: Mesh

tively. Most of heat is generated across the junction where electron and hole recombine. We neglect the radiative recombination. The Peltier and Thomson effects are driven by the variation of the thermoelectric powers (see Fig. 6.19) . The self-consistent thermal map is shown in Fig. 6.20. The maximum value is about $T_{max} = 362\,K$. The flux line underline the path of the thermal flux, mainly dissipated by the substrate. In the next paragraph we will see an example of the coupling of the Fourier model with a Boltzmann Transport Equation based model.

6.5 Nanocolumn

The multiscale thermal model presented in the previous chapter has been applied on a simple system consisting of a GaN quantum dot embedded in a $120\,nm$ high $Al_{0.2}GaN$ column. The quantum dot is pyramidal with a side of $5\,nm$ and is surrounded by an intrinsic GaN buffer layer (see Fig. 6.21). The $AlGaN$ contacts are 1e19 doped.

In order to take into account strain induced by the lattice mismatch along the interface

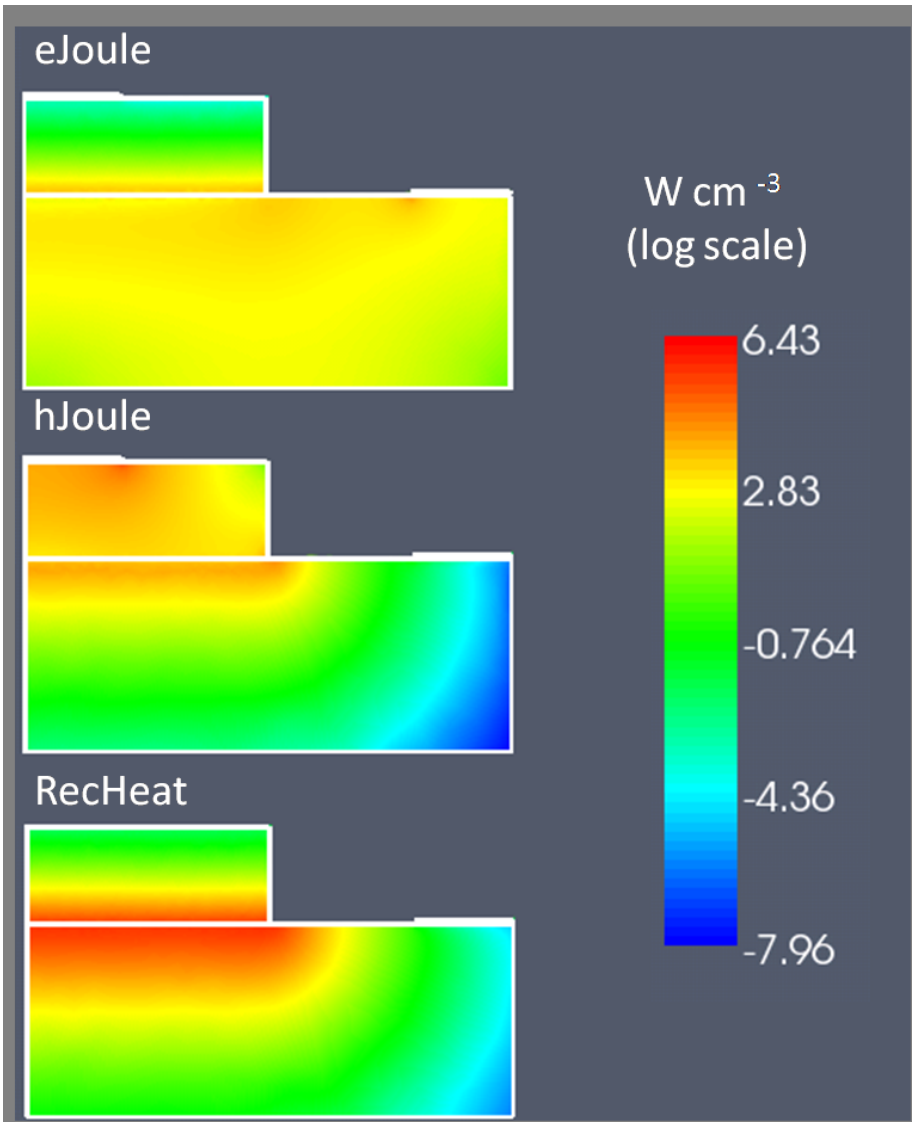

Figure 6.18: Heat sources

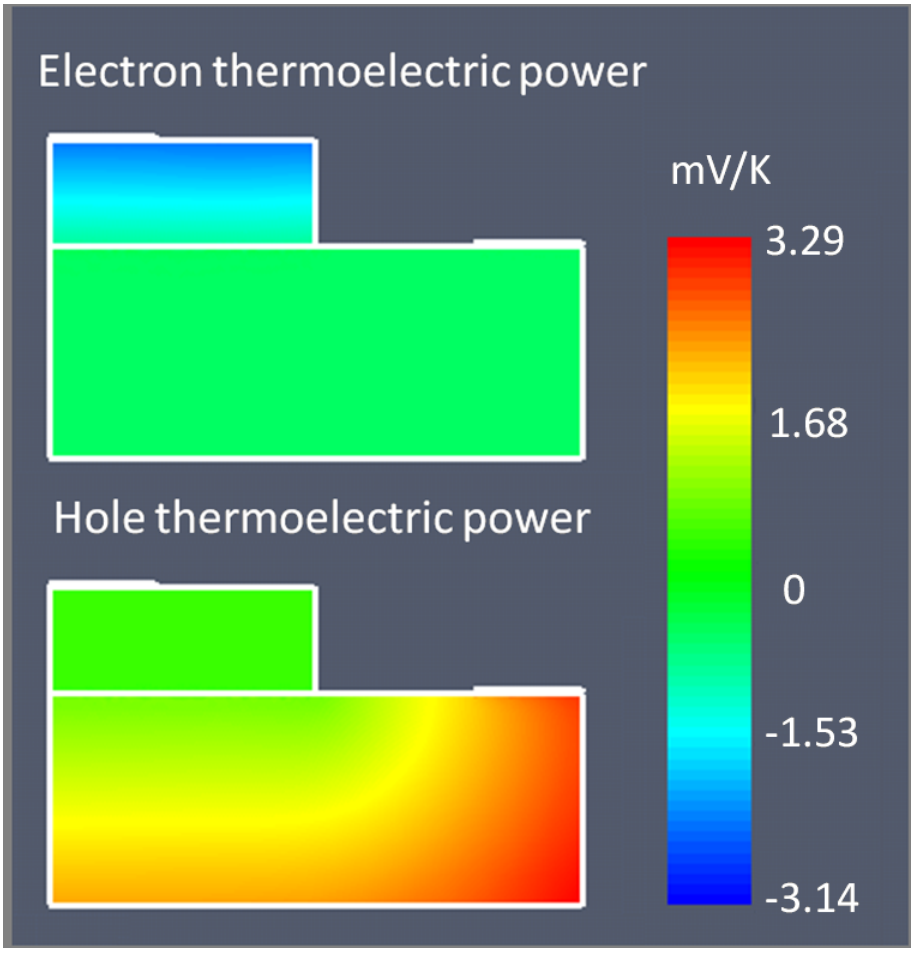

Figure 6.19: Thermoelectric powers

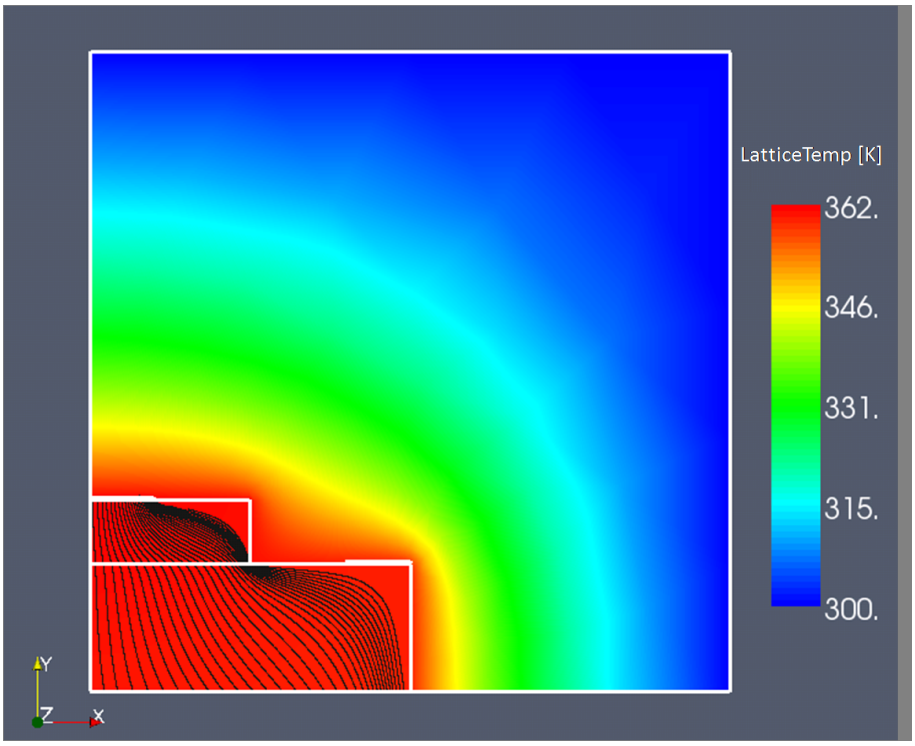

Figure 6.20: Temperature map

with the substrate (assumed of $AlGaN$) we first perform a strain simulation. Details about the implemented physical model is reported in [48]. The internal deformation develops a piezoelectric field which influences the transport properties of the device. Nitride based devices present also a spontaneous polarization, called pyroelectric polarization, due to the asymmetry in the unit cell. The piezoelectric as well as the pyroelectric field act as an effective charge source in the Poisson equation. The continuity equations for electrons and holes as given in Eqs. (4.13)-(4.14), together the Poisson equation, compute the charge transport in the device. As the nanocolumn is polarized directly it presents a diode-like characteristics shown in Fig. 6.22. The thermal simulations are performed for both the gray and the Fourier models. The solid angle is discretized in eighteen parts (six azimut and three elevation angles). Sounds velocities and thermal conductivities of GaN and AlN are taken from Ref. [49]. In order to be consistent with the diffusive limit, the thermal relaxation times are computed from the relationship $\tau = 3\kappa / \left(v_g^2 C\right)$

The sound velocity of $AlGaN$ is obtained by relying on the Virtual Crystal Approximation (VCA) whereas the lattice thermal conductivity is taken from a detailed calculation provided in Ref. [49]. The contacts are fixed to the environment temperature (300 K).

The temperature map obtained by the Fourier simulation is show in Fig. 6.23. The maximum temperature is about 330 K. The heat is mostly generated across the quantum dot and it is dissipated by means of the contacts. The thermal flux is show in Fig. 6.24.

The temperature computed by the Gray model, performed over the whole domain, is reported in Fig.6.25. The maximum temperature is about 355 K, much higher than the temperature computed in the diffusive regime. This reveals that the phonon distribution is far away from the local equilibrium. Furthermore, the gray model gives a strongly peaked temperature across the quantum dot region, resulting in a more realistic temperature profile.

As one can see, Dirichlet boundary conditions imposed to the contacts are not perfectly matched. This behavior is intrinsic of a BTE model and can be interpreted as a boundary thermal resistance [1]. A direct comparison between the Fourier and the Gray model is show in Fig.6.26.

Let us now consider the multiscale model.

We employ a *bridge* scheme. The simulation domain is splitted in two regions: the mesodomain and the macro domain. The mesodomain includes the quantum dot and the buffer region whereas the contacts belong to the macro domain. The partition of the simulation domain is shown in Fig. 6.27.

As already explained in the fourth chapter, we first solve the Fourier simulation over the whole domain. The resulting temperature map is used to fix the boundary temperature for the Gray model and to set the initial guess for the equilibrium energy. Then, the Gray model is computed over the mesodomain. The resulting thermal flux acts as boundary condition for the Fourier simulation which is now computed only over the macrodomain. The loop stops whenever the convergence (on the temperature map) is reached. The scheme has required few steps.

The temperature profile, as shown in Fig. 6.28, is almost the same as that obtained by using

the gray model performed over the whole domain.

In Fig. 6.29 the comparison between the full Gray and the multiscale model is provided. We point out that the size of the mesodomain is a crucial point and it should be chosen accordingly to several factors such as the Knudsen number, the lattice thermal conductivity and the magnitude of the heat source.

A clear comparison between the full Fourier, full gray and the multiscale model is obtained by a cut line along the *growth* axis (see Fig. 6.30). It is possible to note that the multiscale scheme is able to capture the maximum temperature obtained by the full gray model and, in the same time, to match the Dirichlet boundary condition at the contacts.

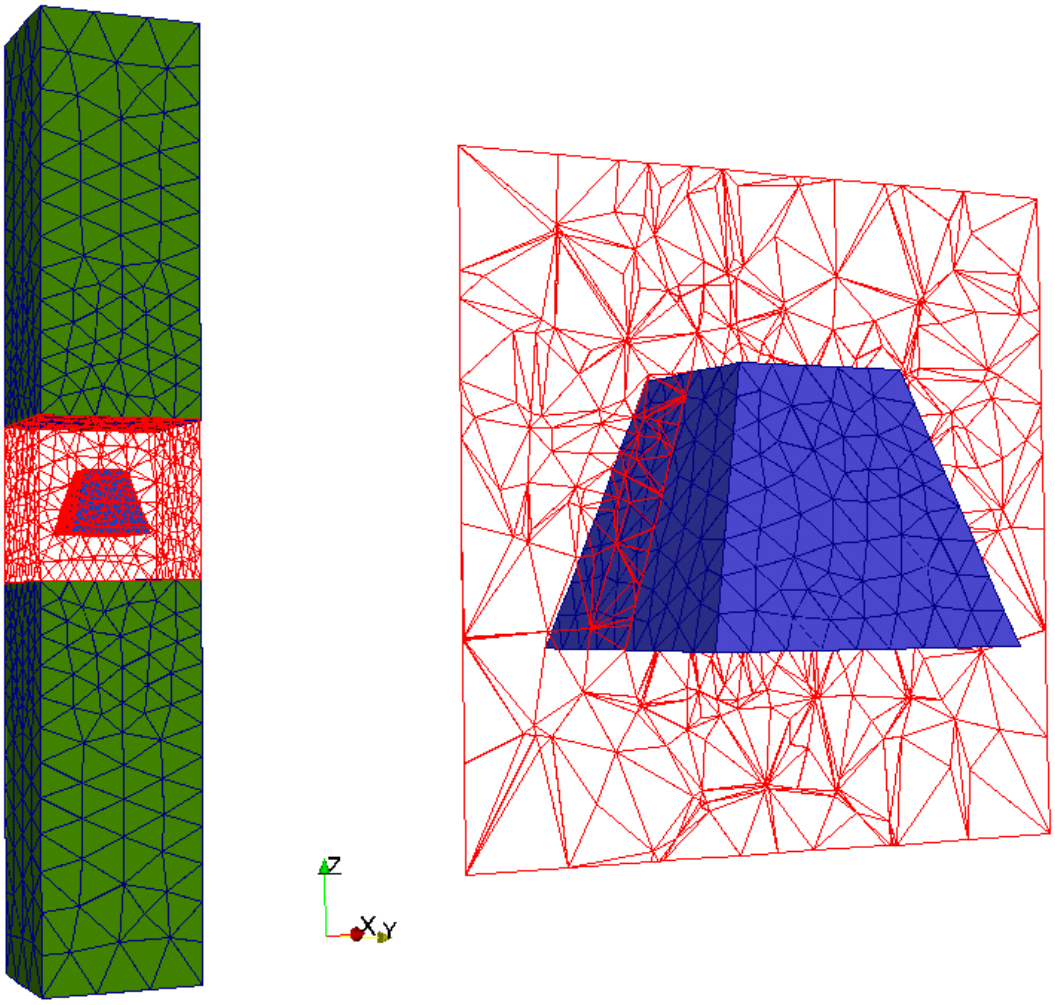

Figure 6.21: The structure

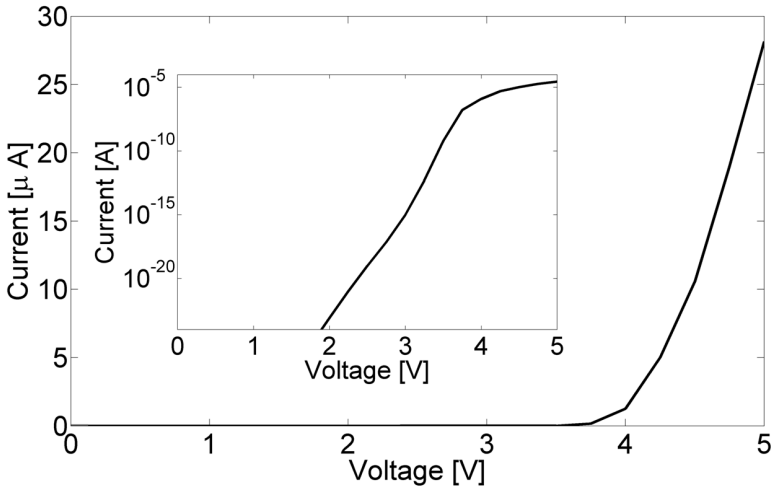

Figure 6.22: I-V characteristic

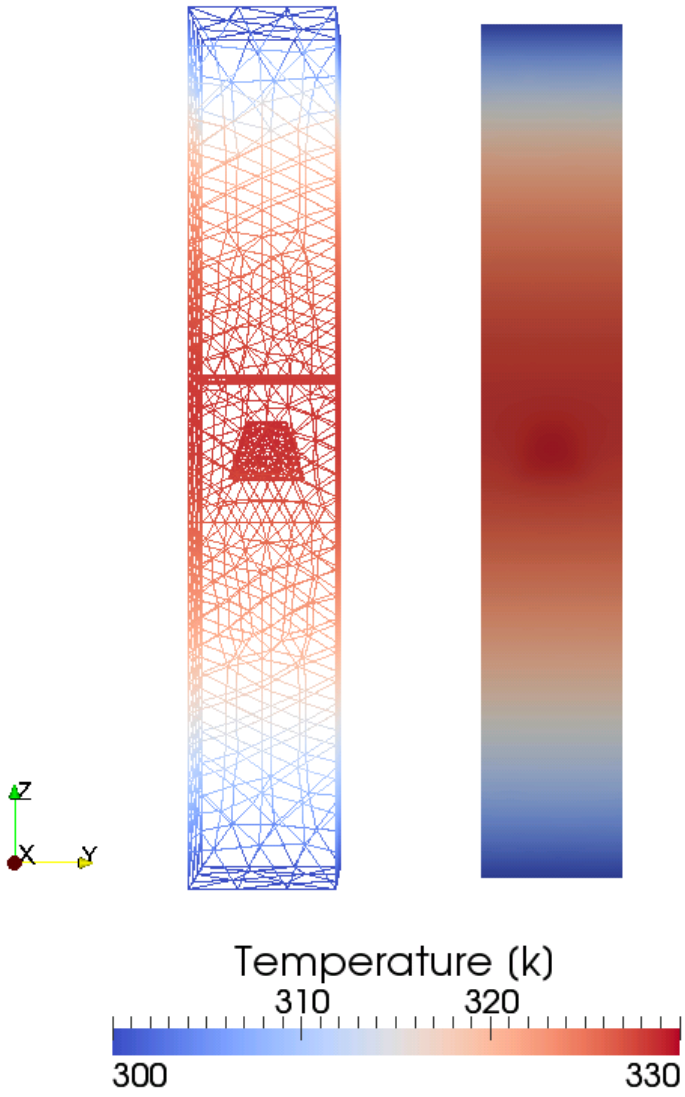

Figure 6.23: Temperature map computed by the Fourier model

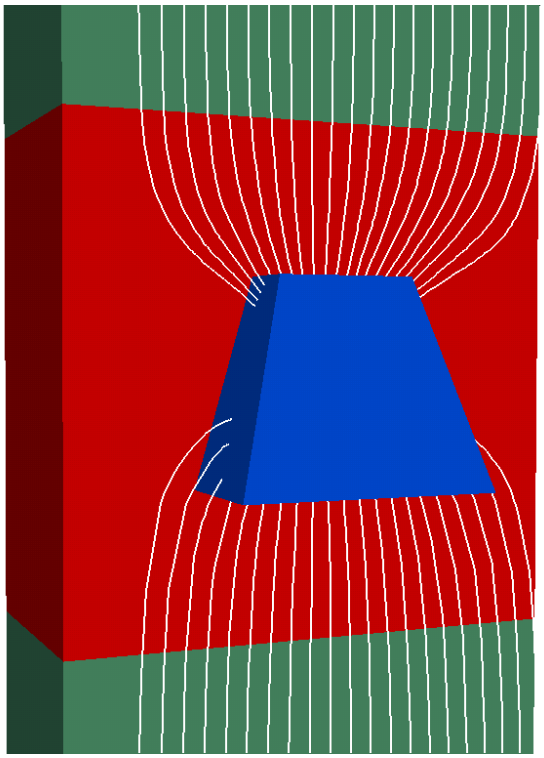

Figure 6.24: Thermal flux computed by the Fourier model

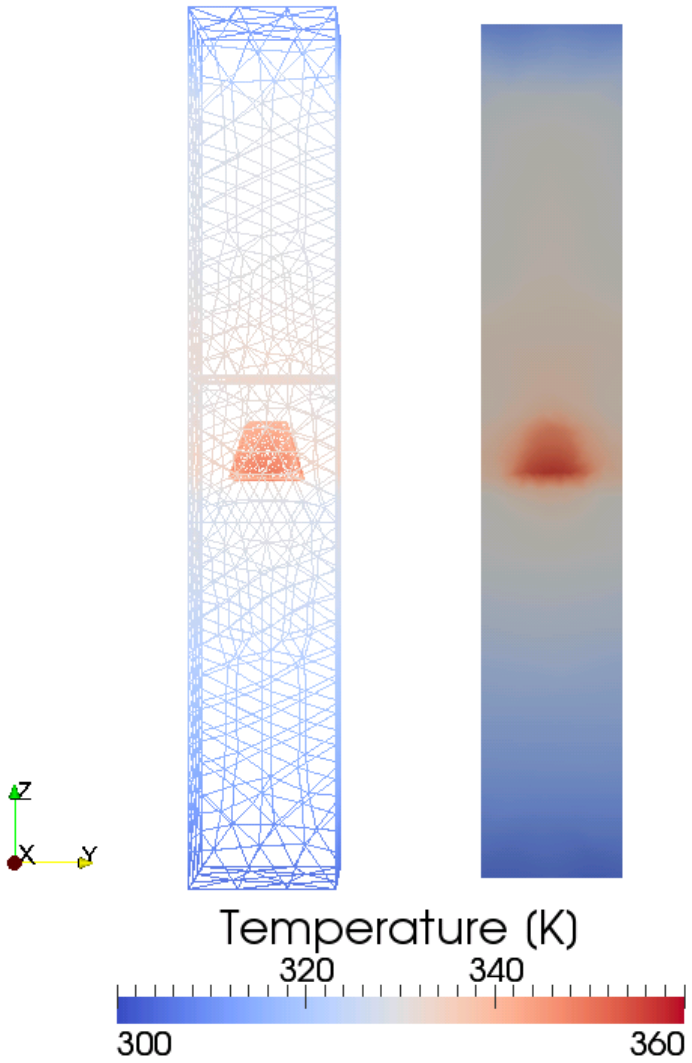

Figure 6.25: Temperature map computed by the gray model

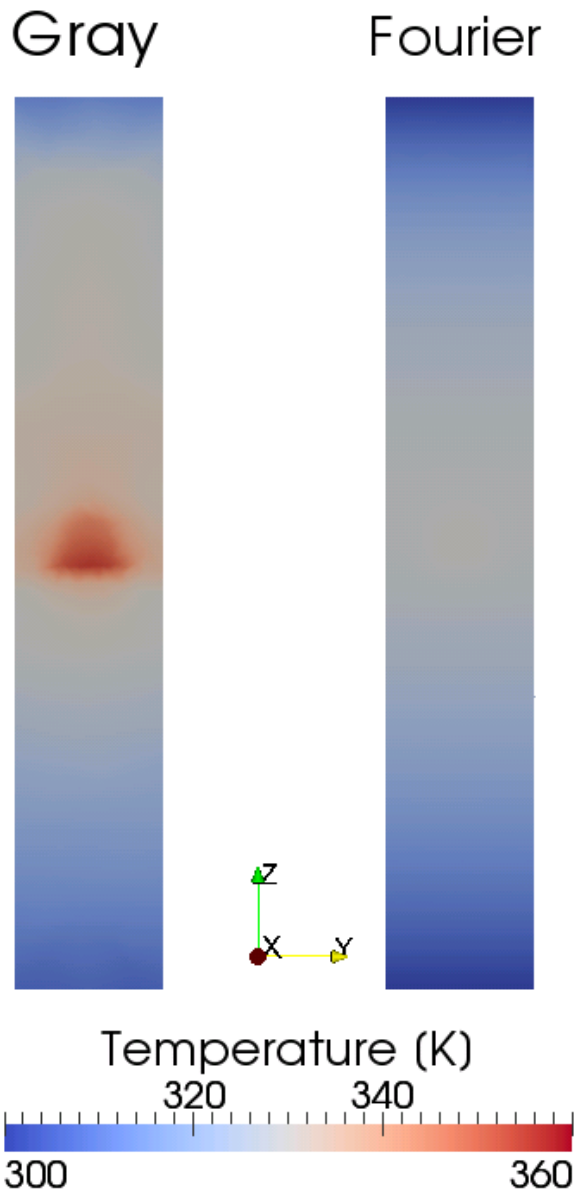

Figure 6.26: Comparison in the temperature map between the Fourier and the gray model

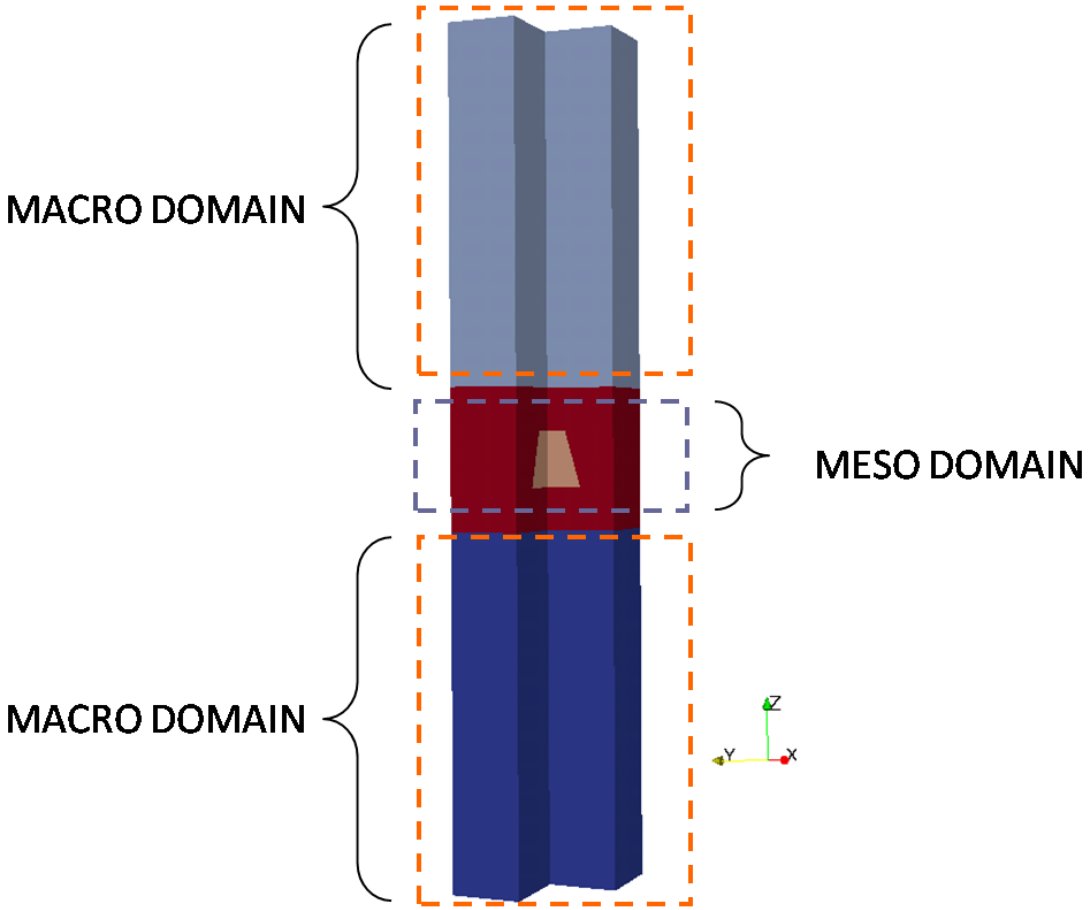

Figure 6.27: Domain partition

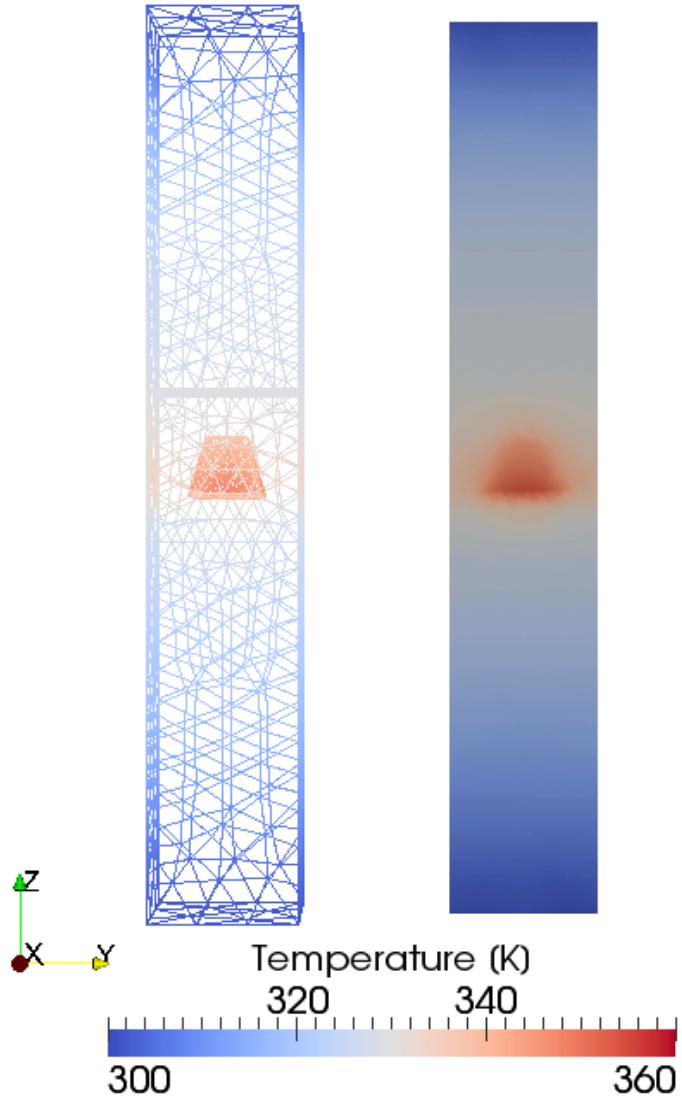

Figure 6.28: Temperature map computed my the multiscale model

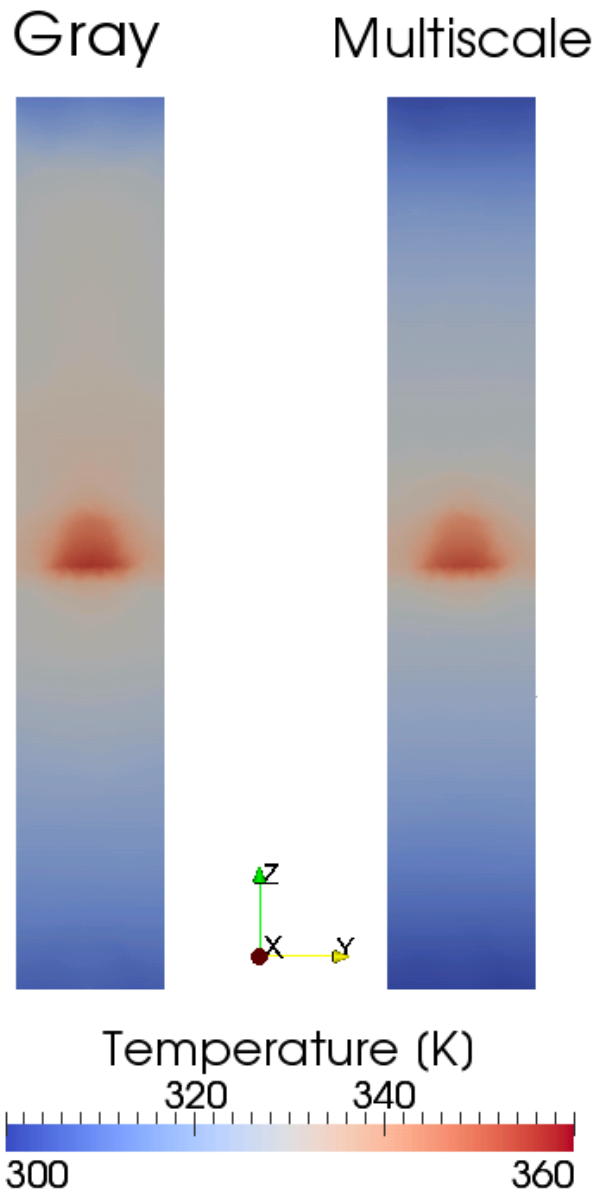

Figure 6.29: Comparison in the temperature map between the gray and the multiscale model

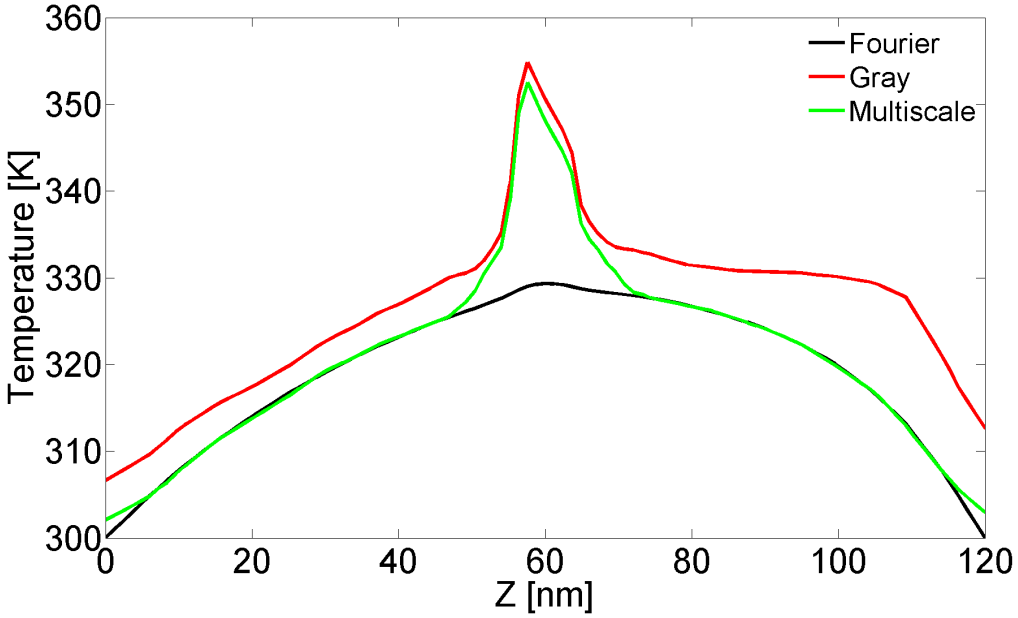

Figure 6.30: Cut along the growth direction of the temperature maps

Chapter 7

Conclusion

In this work we have investigated heating and heat dissipation in several aspects. We investigated heat transport models ranging from the first principles model of the electron-phonon interaction to the diffusive transport.

We reported on the effect of resonances on the thermal behavior of several molecular systems. Thermal effects in fullerene, $C_{10}H_{12}$ and $C_{10}H_{10}$ molecules have been studied.

We analyzed in detail the interplay between molecular resonances, phonon absorption and emission process. An effective molecular temperature was introduced mapping the internal energy stored in the vibrational degrees of freedom.

In the styrene case we underlined the sharp heating across the resonances. In the C_60 case we found that (but the results are general), given a resonance with energy E_L we have found a cooling regime in the bias range $E_L - \hbar\omega < V < E_L + \hbar\omega$ in which the non-equilibrium vibronic population and the effective molecular temperature decreases. Furthermore, we have computed the vibron decay rates due to electron-hole excitations in the substrate and in the tip and we have outlined the importance of these contributions in keeping the molecule stable. A tip-induced cooling effect was also discussed. Finally, we have investigated the possibility to cool the molecule below the environment temperature.

For the $C_{10}H_{12}$ and $C_{10}H_{10}$ molecules we have mainly investigated the thermal instability due to the the competition between the emission and the absorption of phonons.

Regarding the continuous models, we have developed a multiscale scheme with the capability to couple the Fourier and the Boltzmann Transport Equation in the same simulation. The algorithm has been applied to a GaN quantum dot embedded in a $AlGaN$ nanocolumn.

Temperature results of Fourier, gray and multiscale models have been compared. We found out that the Fourier model underestimates the temperature across the quantum dot and underlined the need of BTE based model. The maximum temperature, across the dot, is about 330 K for the Fourier model, against 360 K of the BTE model. We further identified a convenient choice of the initial guess of equilibrium energy density, which strongly speeds up the loop convergence of the gray model. All the three models have been implemented in TiberCAD, the multiscale simulator of optoelectronic devices developed by the OLAB research group at the University of Rome "Tor Vergata".

Appendix A

The self consistent born loop

The numerical simulator implements two nested self-consistent loops. The innermost loop solves the SCBA, which requires the iterative calculations of several equations. We start by assuming that the initial phonon self-energy is zero, $\Sigma_0^{<,>} = 0$, then we define the contact self energies, which are stored on disk and reused at each iterations, since they do not change,

$$\Sigma_n^{<(>)}(\omega) = \Sigma_L^{<(>)}(\omega) + \Sigma_R^{<(>)}(\omega) + \Sigma_{ph,n}^{<(>)}(\omega). \tag{A.1}$$

Then define the imaginary part of the electron-phonon self-energy,

$$\Sigma_{ph,n}^{r}(\omega) = \frac{1}{2}\left[\Sigma_{ph,n}^{>}(\omega) - \Sigma_{ph,n}^{<}(\omega)\right], \tag{A.2}$$

and the total self-energy,

$$\Sigma_n^{r}(\omega) = \Sigma_L^{r}(\omega) + \Sigma_R^{r}(\omega) + \Sigma_{ph,n}^{r}(\omega). \tag{A.3}$$

This enables the computation of the system Green's function,

$$G_n^{r}(\omega) = \left[\omega S - H - \Sigma_n^{r}(\omega)\right]^{-1}. \tag{A.4}$$

The correlation function is then solved from the kinetic equation,

$$G_n^{<(>)}(\omega) = G_n^{r}(\omega)\Sigma_n^{<(>)}(\omega)G_n^{a}(\omega). \tag{A.5}$$

Finally, the electron-phonon scattering can be computed from

$$\Sigma_{ph,n+1}^{<,>} = N_q\gamma_q G_n^{<,>}(E \mp \omega_q)\gamma_q + (N_q+1)\gamma_q G_n^{<,>}(E \pm \omega_q)\gamma_q. \tag{A.6}$$

Equations (A.2)-(A.6) are iterated for $n = 0, 1, ..., \infty$. The loop can be stopped at any step and $G_n^{<(>)}(\omega)$, $\Sigma_{ph,n+1}^{<(>)}(\omega)$ can be used to compute the phonon emission rate and current. It may be observed that this scheme ensure current conservation since $\Sigma_{ph}^{<,>}$ are computed from the same $G^{<,>}$ used in (2.21) to compute the virtual contact current and the emitted power

(2.19). This trick can be used in programming efficiently a SCBA loop which guarantees a correct calculation of the emitted power even when stopped after the first or a few steps. It is worth noting that when the loop is stopped at the second iteration ($n = 1$) the virtual contact current already contains terms of second order, whereas the current through the molecule is accurate to first order approximation. In general the power emitted is accurate to order $n + 1$, and the current flowing through the molecule is accurate to order n. In this way the virtual contact current is guaranteed to vanish for any n, giving a correct result for the emitter power and rate of phonon emission. The inconsistence disappears in the SCBA, but it is not of great concern, since the calculation of phonon emission rate and current can be considered independent.

Bibliography

[1] Z. M. Zhang, [*Nano/microscale heat transfer*], MacGrow-Hill (2005).

[2] G. Romano, A. Pecchia and A. D. Carlo. *Coupling of molecular vibrons with contact phonon reservoirs*. **Journal of Physics: Condensed Matter**, 19(21), 215207 (2007).

[3] A. Pecchia, A. Di Carlo, A. Gagliardi, S. Sanna, T. Frauenheim and R. Gutierrez. *Incoherent electron-phonon scattering in octanethiols*. **Nano Lett.**, 4, 2109 (2004).

[4] A. Pecchia, G. Romano and A. Di Carlo. *Theory of heat dissipation in molecular electronics*. **Phys. Rev. B**, 75, 035401 (Jan 2007).

[5] Y. Meir and N. S. Wingreen. *Landauer formula for the current through an interacting electron region*. **Phys. Rev. Lett.**, 68, 2512–2515 (Apr 1992).

[6] L. V. Keldysh. *Diagram Technique for Nonequilibrium Processes*. **Soviet Physics JETP**, 20, 1018 (1964).

[7] L. P. Kadanoff and G. Baym, [*Quantum Statistical Mechanics*], W. A. Benjamin (1962).

[8] T. Frauenheim, G. Seifert, M. Elstner, T. Niehaus, C. Köhler, M. Amkreutz, M. Sternberg, Z. Hajnal, A. D. Carlo and S. Suhai. *Atomistic simulations of complex materials: ground-state and excited-state properties*. **Journal of Physics: Condensed Matter**, 14(11), 3015 (2002).

[9] S. Datta, [*Electronic Transports in Mesoscopic Systems*], Cambridge (1995).

[10] A. Pecchia and A. D. Carlo. *Atomistic theory of transport in organic and inorganic nanostructures*. **Reports on Progress in Physics**, 67(8), 1497 (2004).

[11] M. Paulsson, T. Frederiksen and M. Brandbyge. *Modeling inelastic phonon scattering in atomic- and molecular-wire junctions*. **Phys. Rev. B**, 72, 201101 (Nov 2005).

[12] N. Mingo and K. Makoshi. *Calculation of the Inelastic Scanning Tunneling Image of Acetylene on Cu(100)*. **Phys. Rev. Lett.**, 84, 3694–3697 (Apr 2000).

[13] E. G. Emberly and G. Kirczenow. *Landauer theory, inelastic scattering, and electron transport in molecular wires*. **Phys. Rev. B**, 61, 5740–5750 (Feb 2000).

[14] B. Dong, H. L. Cui and X. L. Lei. *Photon-phonon-assisted tunneling through a single-molecule quantum dot*. **Phys. Rev. B**, 69, 205315 (May 2004).

[15] H. Ness and A. J. Fisher. *Coherent electron injection and transport in molecular wires: inelastic tunneling and electron-phonon interactions*. **Chemical Physics**, 281(2-3), 279 – 292 (2002).

[16] A. Nitzan, S. Mukamel and J. Jortner. *Some features of vibrational relaxation of a diatomic molecule in a dense medium*. **The Journal of Chemical Physics**, 60(10), 3929–3934 (1974).

[17] M. Budde, G. Lüpke, C. Parks Cheney, N. H. Tolk and L. C. Feldman. *Vibrational Lifetime of Bond-Center Hydrogen in Crystalline Silicon*. **Phys. Rev. Lett.**, 85, 1452–1455 (Aug 2000).

[18] A. Nitzan, [*Chemical Dynamics in Condesed Phases*], Oxford University Press (2006).

[19] Y.-C. Chen, M. Zwolak and M. Di Ventra. *Local heating in nanoscale conductors*. **Nano Letters**, 3(12), 1691 – 4 (2003/12/).

[20] T. N. Todorov, J. Hoekstra and A. P. Sutton. *Current-Induced Embrittlement of Atomic Wires*. **Phys. Rev. Lett.**, 86, 3606–3609 (Apr 2001).

[21] A. A. Joshi and A. Majumdar. *Transient ballistic and diffusive phonon heat transport in thin films*. **Journal of Applied Physics**, 74(1), 31–39 (1993).

[22] M. G. Holland. *Analysis of Lattice Thermal Conductivity*. **Phys. Rev.**, 132, 2461–2471 (Dec 1963).

[23] S. V. J. Narumanchi, J. Y. Murthy and C. H. Amon. *Submicron Heat Transport Model in Silicon Accounting for Phonon Dispersion and Polarization*. **Journal of Heat Transfer**, 126(6), 946–955 (2004).

[24] P. G. Sverdrup, Y. S. Ju and K. E. Goodson. *Sub-Continuum Simulations of Heat Conduction in Silicon-on-Insulator Transistors*. **Journal of Heat Transfer**, 123(1), 130–137 (2001).

[25] E. Pop, S. Sinha and K. Goodson. *Heat Generation and Transport in Nanometer-Scale Transistors*. **Proceedings of the IEEE**, 94, 1587 –1601 (aug. 2006).

[26] G. Chen. *Ballistic-Diffusive Heat-Conduction Equations*. **Phys. Rev. Lett.**, 86, 2297–2300 (Mar 2001).

[27] J. Y. M. Sreekant V. J. Narumanchi and C. H. Amon. *Boltzmann transport equation-based thermal modeling approaches for hotspots in microelectronic*. **Heat and Mass Transfer**, 42(6), 478–491 (2006).

[28] S. V. J. Narumanchi, J. Y. Murthy and C. H. Amon. *Comparison of Different Phonon Transport Models for Predicting Heat Conduction in Silicon-on-Insulator Transistors*. **Journal of Heat Transfer**, 127(7), 713–723 (2005).

[29] G. Chen. *Thermal conductivity and ballistic-phonon transport in the cross-plane direction of superlattices*. **Phys. Rev. B**, 57, 14958–14973 (Jun 1998).

[30] Z. Chen, [*Finite Element Methods and their Applcations*], Springer (2005).

[31] R. J. Stoner and H. J. Maris. *Kapitza conductance and heat flow between solids at temperatures from 50 to 300 K*. **Phys. Rev. B**, 48, 16373–16387 (Dec 1993).

[32] G. Romano, G. Penazzi and A. D. Carlo. *Multiscale thermal modeling of GaN/AlGaN quantum dot LEDs*. **Physics and Simulation of Optoelectronic Devices XVIII**, 7597(1), 75971S, SPIE (2010).

[33] M. Le Bellac, F. Mortessagne and G. G. Batroumi, [*Equilibrium and non equilibrium statistical thermodynamics*], Cambridge (2006).

[34] L. Onsager. *Reciprocal Relations in Irreversible Processes. I.* **Phys. Rev.**, 37, 405–426 (Feb 1931).

[35] M. A. D. Maur, *A Multiscale Simulation Environment for Electronic and Optoelectronic Devices*, PhD dissertation, Tor Vergata University (Rome, Italy) (2008).

[36] G. K. Wachutka. *Rigorous Thermodynamic Treatment of Heat Generation and Conduction in Semiconductor Device Modeling*. **IEEE Transactions on Computer-Aided Design**, 11, 1141–1149 (Nov. 1990).

[37] A. Ern and J.-L. Guermond, [*Theory and Practice of Finite Elements*], vol. 159 of *Applied Mathematical Sciences*, Springer (2004).

[38] O. C. Zienkiewicz and R. L. Taylor, [*The Finite Element Method*], vol. 1, McGraw-Hill, 4th ed. (1994).

[39] K. D. Mish, L. R. Herrmann and L. Haws, [*Finite Element Procedures in Applied Mechanics*], Lecture notes, University of California, 1st ed. (2000).

[40] *www.tibercad.org*.

[41] M. Auf Der Maur, M. Povolotskyi, F. Sacconi, A. Pecchia, G. Romano, G. Penazzi and A. Di Carlo. *TiberCAD: Towards multiscale simulation of optoelectronic devices*. **Optical and Quantum Electronics**, 40(14-15 SPEC. ISS.), 1077 – 1083 (2008).

[42] M. Auf der Maur, M. Povolotskyi, S. Fabio, A. Pecchia and A. Di Carlo. *Multiscale simulation of MOS systems based on high-k oxides.* **Journal of Computational Electronics**, 7(3), 398–402 (2006).

[43] G. Penazzi, A. Pecchia, F. Sacconi and A. D. Carlo. *Calculation of optical properties of a quantum dot embedded in a GaN/AlGaN nanocolumn*. **Superlattices and Microstructures**, 47(1), 123 – 128 (2010).

[44] G. Romano, A. Gagliardi, A. Pecchia and A. Di Carlo. *Heating and cooling mechanisms in single-molecule junctions*. **Phys. Rev. B**, 81, 115438 (Mar 2010).

[45] G. Schulze, K. J. Franke, A. Gagliardi, G. Romano, C. S. Lin, A. L. Rosa, T. A. Niehaus, T. Frauenheim, A. Di Carlo, A. Pecchia and J. I. Pascual. *Resonant Electron Heating and Molecular Phonon Cooling in Single C60 Junctions*. **Phys. Rev. Lett.**, 100, 136801 (Apr 2008).

[46] D. Porezag, T. Frauenheim, T. Köhler, G. Seifert and R. Kaschner. *Construction of tight-binding-like potentials on the basis of density-functional theory: Application to carbon*. **Phys. Rev. B**, 51, 12947–12957 (May 1995).

[47] R. Härtle, C. Benesch and M. Thoss. *Vibrational Nonequilibrium Effects in the Conductance of Single Molecules with Multiple Electronic States*. **Phys. Rev. Lett.**, 102, 146801 (Apr 2009).

[48] M. Povolotskyi and A. Di Carlo. *Elasticity theory of pseudomorphic heterostructures grown on substrates of arbitrary thickness*. **Journal of Applied Physics**, 100(6) (2006).

[49] W. Liu and A. Balandin. *Thermal conduction in Al[sub x]Ga[sub 1 - x]N alloys and thin films*. **Journal of Applied Physics**, 97(7), 073710 (2005).

List of Figures

Journal articles

1. A. Gagliardi, G. Romano, A. Pecchia and A. Di Carlo. *Simulation of Inelastic Scattering in Molecular Junctions: Application to Inelastic Electron Tunneling Spectroscopy and Dissipation Effects*. **Journal of Computational and Theoretical Nanoscience** (accepted).

2. M. Auf der Maur, F. Sacconi, G. Penazzi, M. Povolotskyi, G. Romano, A. Pecchia and A. Di Carlo. *Coupling atomistic and finite element approaches for the simulation of optoelectronic devices*. **Optical and Quantum Electronics** (in press).

3. G. Romano, A. Gagliardi, A. Pecchia and A. Di Carlo. *Heating and cooling mechanisms in single-molecule junctions*. **Physical Review B**, 81(11), 115438 (2010).

4. A. Gagliardi, G. Romano, A. Pecchia, A. Di Carlo, T. Frauenheim and T. A. Niehaus. *Electron-phonon scattering in molecular electronics: From inelastic electron tunnelling spectroscopy to heating effects*. **New Journal of Physics**, 10 (2008).

5. G. Schulze, K. Franke, A. Gagliardi, G. Romano, C. Lin, A. Rosa, T. A. Niehaus, T. Frauenheim, A. Di Carlo, A. Pecchia and J. Pascual. *Resonant electron heating and molecular phonon cooling in single C_{60} junctions*. **Physical Review Letters**, 100(13) (2008).

6. A. Pecchia, G. Romano, A. Di Carlo, A. Gagliardi and T. Frauenheim. *Joule heating in molecular tunnel junctions: Application to C_{60}*. **Journal of Computational Electronics**, 7(3), 384 – 389 (2008).

7. M. Auf Der Maur, M. Povolotskyi, F. Sacconi, A. Pecchia, G. Romano, G. Penazzi and A. Di Carlo. *TiberCAD: Towards multiscale simulation of optoelectronic devices*. **Optical and Quantum Electronics**, 40(14-15 SPEC. ISS.), 1077 – 1083 (2008).

8. G. Romano, A. Pecchia and A. Di Carlo. *Coupling of molecular vibrons with contact phonon reservoirs*. **Journal of Physics Condensed Matter**, 19(21) (2007).

9. A. Pecchia, G. Romano and A. Di Carlo. *Theory of heat dissipation in molecular electronics*. **Physical Review B**, 75(3), 35401 – 1 (2007).

10. A. Pecchia, G. Romano, A. Gagliardi, T. Frauenheim and A. Di Carlo. *Heat dissipation and non-equilibrium phonon distributions in molecular devices*. **Journal of Computational Electronics**, 6(1-3), 335 – 339 (2007).

Proceedings

1. G. Romano, G. Penazzi and A. D. Carlo. *Multiscale thermal modeling of GaN/AlGaN quantum dot LEDs*. **Physics and Simulation of Optoelectronic Devices XVIII**, 7597(1), 75971S, SPIE (2010).

2. G. Penazzi, A. Pecchia, F. Sacconi, M. Auf der Maur, M. Povolotskyi, G. Romano and A. Di Carlo. *Simulations of Optical Properties of a GaN Quantum Dot Embedded in a AlGaN Nanocolumn within a Mixed FEM/atomistic Method*. **13th International Workshop on Computational Electronics (IWCE '09)**, 1 –4 (2009).

3. M. Auf der Maur, F. Sacconi, G. Penazzi, M. Povolotskyi, G. Romano, A. Pecchia and A. Di Carlo. *Coupling atomistic and finite element approaches for the simulation of optoelectronic devices*. **9th International Conference on Numerical Simulation of Optoelectronic Devices (NUSOD)**, 75 – 80 (2009).

4. A. Di Carlo, M. Auf der Maur, F. Sacconi, A. Pecchia, M. Povolotskyi, G. Penazzi and G. Romano. *Multiscale atomistic simulations of high-k MOSFETs*. **Proceedings of the 8th IEEE International Conference on Nanotechnology**, 377 – 384 (2008).

5. A. Pecchia, G. Romano and A. Di Carlo. *Modeling of dissipative transport in molecular systems*. **Proceedings of the 7th IEEE International Conference on Nanotechnology**, 1185 – 1192 (2008).

6. F. Sacconi, G. Romano, G. Penazzi, M. Povolotskyi, M. Auf der Maur, A. Pecchia and A. Di Carlo. *Electronic and transport properties of GaN/AlGaN quantum dot-based p-i-n diodes*. **Interational Conference on Simulation of Semiconductor Processes and Devices (SISPAD 2008)**, 177 –180 (sept. 2008).

7. M. Auf der Maur, M. Povolotskyi, F. Sacconi, G. Romano, P. E. and A. Di Carlo. *Multiscale Simulation of Electronic and Optoelectronic Devices with TiberCAD*. **Interational Conference on Simulation of Semiconductor Processes and Devices (SISPAD 2007)**, 245 –248 (sept. 2007).

Presentations

1. G. Romano, G. Mantini, A. Di Carlo, A. D'Amico, C. Falconi and Z. L. Wang. *Simulation of piezoelectric nanogenerators with TiberCAD*. **AISEM 2010**, Messina (Italy), 8–10, Feb 2010 (Poster).

2. G. Romano, G. Penazzi and A. Di Carlo. *Multiscale thermal modeling of GaN/AlGaN quantum DOT LEDs*. **SPIE Photonics West**, San Francisco, CA (USA), 23–28, Jan 2010 (Oral).

3. F. Sacconi, G. Romano, G. Penazzi, M. Povolotskyi, M. Auf der Maur, A. Pecchia and A. Di Carlo. *Electronic and transport properties of GaN/ALGaN quantum dot based p-i-n diodes*. **SISPAD 2008**, Hakone (Japan), 9–11, Sep 2008 (Poster).

4. G. Romano, G. Penazzi, M. Auf der Maur, F. Sacconi, M. Povolotskyi, A. Pecchia and A. Di Carlo. *TiberCAD: the new multiscale simulator for electronic and optoelectronic devices*. **40th Electronic Group Meeting**, Otranto (Italy), 16–18, Jun 2008 (Poster).

5. G. Romano, G. Penazzi, M. Auf der Maur, F. Sacconi, M. Povolotskyi, A. Pecchia and A. Di Carlo. *A new Multiscale simulator for electronics and optoelectronics devices*. **New frontiers in micro and nanophotonics**, Florence (Italy), 23–26, April 2008 (Oral).

6. G. Romano, M. Auf der Maur, M. Povolotskyi, F. Sacconi, E. Petrolati, A. Pecchia and A. Di Carlo. *Multiscale approach in the heat balance problems*. **International summer school on advanced microelectronics**, Grenoble (France), 24–29, Jun 2007 (Poster).